Synthesis of Cesium Tungsten Bronze Nanoparticles by Spray Pyrolysis and Their Optical Properties

(噴霧法によるセシウムタングステンブロンズナノ粒子の合成と光学特性)

By

Shuhei Nakakura

Department of Chemical Engineering

Graduate School of Engineering

Hiroshima University

March 2020

Contents

Contents

Chapter 1

Introduction

1.1 Background

In September 2015, the United Nations adopted 17 Sustainable Development Goals with 169 targets. To achieve these goals, functional nanoparticle research requires further advances based on the material's chemical and physical properties [1].

In working to achieve minimal energy consumption, Sumitomo Metal Mining Co., Ltd. (SMM) commercialized cesium tungsten bronze nanoparticles as an effective infrared absorption material [2,3]. This dissertation notably focused on developing cesium tungsten bronze nanoparticles using a spray pyrolysis method [4,5].

1.2 Methods for particle preparation

In general, high purity, high crystallinity, uniform composition, and monodispersion are required for functional nanoparticles [5]; however, these properties are strongly related to the synthesis method. Thus, this section summarizes the gas-, liquid-, and solid-phase characteristics of the synthesis process based on the appropriate use for each application.

1.2.1 Gas-phase process

In the gas-phase process, particles are built from atoms or molecules to obtain the desired size, which is called the vapor-phase [6] or aerosol process [5,7]. The primary advantages of the vapor-phase process are to obtain a small particle size (from a few nanometers to microns), narrow size distribution, high purity, and high crystallinity. This

process could achieve a reaction field with high energy over several hundred degrees or more. However, the disadvantage of the vapor-phase process is the formation of hard agglomerates, low productivity, and the high apparatus cost.

The name of the vapor-phase process varies depending on the precursor phase and the heating energy source. In this doctoral dissertation, these names are classified (**Table 1.1**) and each method is summarized. **Figure 1.1** shows typical particle images.

Table 1.1 Classification of particle synthesis using the vapor-phase process.

		Heating Source		
		Electric Furnace	Flame Field	Plasma Field
Precursor Phase	Vapor Phase	Chemical Vapor Deposition (CVD)	Vapor-fed Aerosol Flame (VFAF)	Plasma-enhanced CVD (PECVD)
	Liquid Phase (Droplet)	Spray Pyrolysis (SP)	Flame-assisted Spray Pyrolysis (FASP)	-
	Solid Phase (Powder)	Physical Vapor Deposition (PVD)	Solid-fed Flame Synthesis (SFFS)	Thermal Plasma Synthesis (TPS)

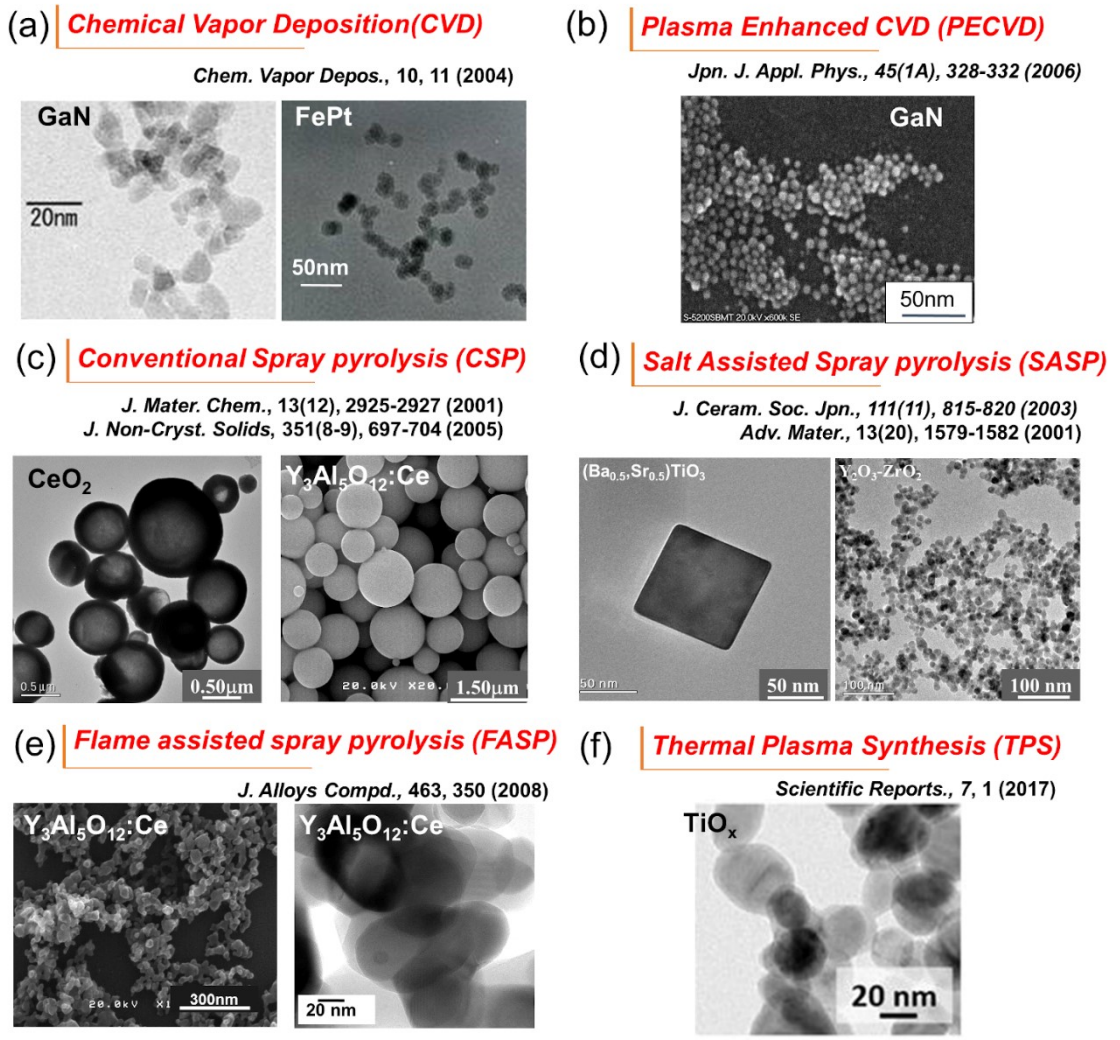

Figure 1.1 Typical particle images using the gas-phase process: (a) chemical vapor deposition (CVD), (b) plasma-enhanced CVD, (c) conventional spray pyrolysis (CSP), (d) salt-assisted spray pyrolysis (SASP), (e) flame-assisted spray pyrolysis (FASP), and (f) thermal plasma synthesis (TPS).

1.2.1.1 Chemical and physical vapor deposition

Chemical vapor deposition (CVD) has been widely applied to prepare thin films, such as graphene [8], Molybdenum sulfide (MoS_2) [9], and gallium nitride (GaN) [10]. In the CVD method, vapor-phase precursors are brought into a heated reactor. Products are then obtained by nucleation in the gas phase [11]. The principle of obtaining nanoparticles

using the CVD method is to change the film conditions to low temperature and high supersaturation [12,13]. Electric furnaces are widely used as the heat source, but techniques using a laser [14] or plasma [15] have been developed to accelerate the precipitation reaction. The CVD method was recently applied to particle coatings, fine particle composites, and nanoparticle synthesis [16].

Physical vapor deposition is a technique in which a precursor material is heated to a melting point or higher to form a vapor phase [17]. It can then be cooled to promote the nucleation and precipitation of nanoparticles. In this method, particle sizes can be controlled by the heating temperature and cooling rate of the precursor.

1.2.1.2 Spray pyrolysis

Conventional spray pyrolysis (CSP) is a continuous method for producing spherical particles with adjustable sizes (controllable from submicron to micrometers), narrow size distribution, high crystallinity, and good stoichiometry (**Figure 1.2(a)**) [5]. In CSP, multicomponent materials, including oxide, sulfide, and carbide, are easily obtained to mix well all components in the solvent (e.g., water or alcohol [5]).

To produce spherical particles using CSP, the droplets, which are atomized from a precursor solution, are introduced to an electric furnace. Evaporation of the solvent, precipitation, pyrolysis, or sintering in carrier gas may occur inside the furnace. The mechanism of particle formation is known that one droplet to one particle [4]. Submicrometer to micrometer-sized particles are typically formed in CSP.

Although the CSP process has been widely used to synthesize multicomponent materials in a simple process, modifications of the CSP process for obtaining nanoparticles, such as low-pressure spray pyrolysis (LPSP), pulse combustion-spray pyrolysis (PCSP), salt-assisted spray pyrolysis (SASP), flame-assisted spray pyrolysis

(FASP), and spray drying were developed [1,4,5].

In LPSP, a two-step spray atomizer, e.g., a filter-expansion aerosol generator (FEAG) was used and a pyrolysis reaction proceeds in low pressures around 2–10 kPa to obtain nanoparticles (**Figure 1.2(b)**). Because the solvent evaporation of droplet in low pressure fields is promoted, the dispersed nanoparticles were obtained before agglomeration occurred.

PCSP is a method integrating CSP and PCSP (**Figure 1.2(c)**). PCSP provides enhanced momentum and energy to the droplets by generation of high-intensity acoustic waves; therefore, solvent evaporation was promoted rapidly, and weakly agglomerated nanoparticles were obtained easily.

SASP is a modified method of CSP, where a salt is introduced into a precursor solution to obtain dispersed nanoparticles [18]. Nanoparticles derived from SASP prevented agglomeration and promoted crystallinity because of the effect of the salt as a flux (**Figure 1.2(d)**). During the SASP process, when the particle temperature exceeded the melting point of salts in the furnace, salts, such as chlorides or nitrates of Li, Na, and K, acted as high-temperature solvents (*i.e.*, a molten state). Various materials such as NiO, Ag-Pd, ZnS, and CeO_2 were synthesized using SASP [19–21]. The SASP method could be applicable in finding new materials.

Nanostructured particles, which have controlled shapes and morphology at the nanoscale, have great potential for saving resources and improving handling properties [4,22,23]. Nano risk could be avoided by using nanostructured particles because the particle size is in the submicrons. However, the nanosized pore can exhibit the same performance as the nanoparticle. These particles can be synthesized using the spray-drying method with template particles in a precursor solution, as shown in **Figure 1.2 (e)**.

In the spray-drying method, the precursor including the template particles is sprayed,

and then, solvent evaporation and self-assembly proceeds. Particles with several morphologies (*e.g.*, sphere, doughnut, encapsulated, porous, multiporous, hollow, and hairy) could be synthesized. To reduce the cost of template particles, methods using recyclable or inexpensive available materials (*e.g.*, polymethyl methacrylate resin) were developed recently [24].

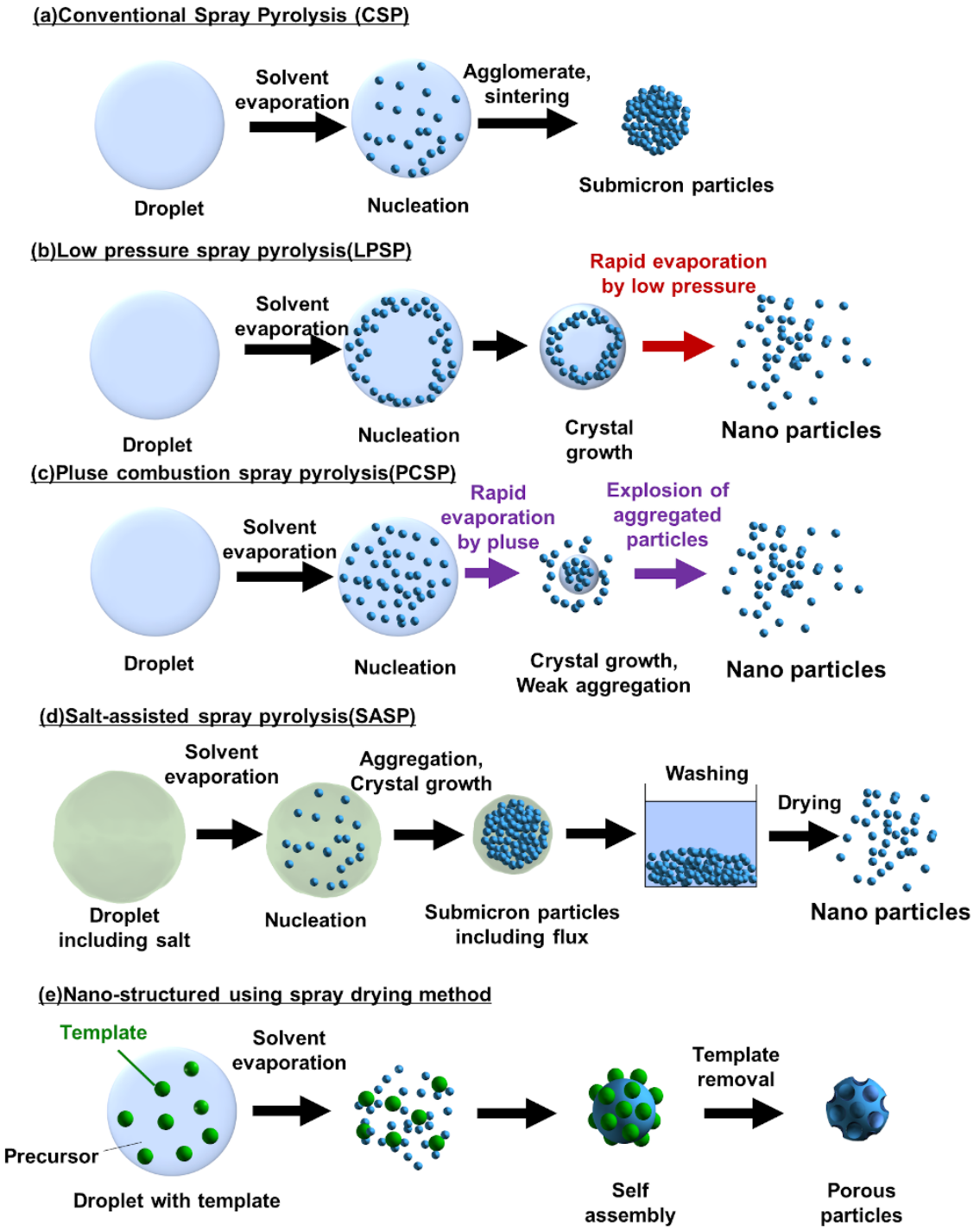

Figure 1.2 Precipitation mechanisms for (a) CSP, (b) LPSP, (c) PCSP, (d) SASP, and (e) nanostructured using a spray-drying method.

1.2.1.3 Vapor-fed aerosol flame and flame-assisted spray pyrolysis

Vapor-fed aerosol flame (VFAF) where a vapor precursor is introduced into the flame has been practically used as a method for synthesizing SiO_2 and Al_2O_3 particles [25]. However, vapor precursors in VFAF are mostly limited to low-cost precursors, such as chloride (*e.g.*, $SiCl_4$ and $AlCl_3$), and chlorine gas-generated toxic products.

Because of the availability of an inexpensive precursor solution, flame spray pyrolysis (FSP) has been developed, where the precursor is in liquid form with high combustion enthalpy (>50% of the total energy of combustion), such as organic solvents [26,27]. The use of exothermic liquid precursors produces self-sustaining flames. If a low-combustion enthalpy solution, such as an aqueous solution was used, this method was called FASP. Recently, single atoms or cluster-sized metal loaded onto support particles for catalysts was developed using FSP [28].

1.2.1.4 Thermal plasma synthesis

Thermal plasma synthesis (TPS) is a high productivity method on a large scale, which has some advantages of thermal plasma, such as high enthalpy, high chemical reactivity, and a rapid quenching process. In TPS, solid precursors were vaporized in high temperatures over 10,000 degrees. This vapor was converted into several nanoparticles when the temperature of the vaporized precursor cooled [29]. However, the particle growth mechanism remains unclear because these nanoparticles were precipitated in a few tens of milliseconds even when using the gas-phase synthesis method. Furthermore, the energy use of this apparatus is inefficient.

1.2.2 Liquid-phase process

The liquid-phase method was popular for the synthesis of various types of nanoparticles, such as particles with various structures (*e.g.*, rods, cubic, and plate structures) obtained from liquid precursors [30]. The advantages of the liquid-phase process are that it is possible to apply in laboratory to industrial scales and it uses ultrasonic waves and microwaves to promote precipitation [31]. Furthermore, the control of nanoscale morphologies could be developed using sol–gel, solvothermal, and hydrothermal methods, among others. The drawback of this process is the extensive synthesis time or too many experimental steps. The typical particle images are shown in **Figure 1.3**.

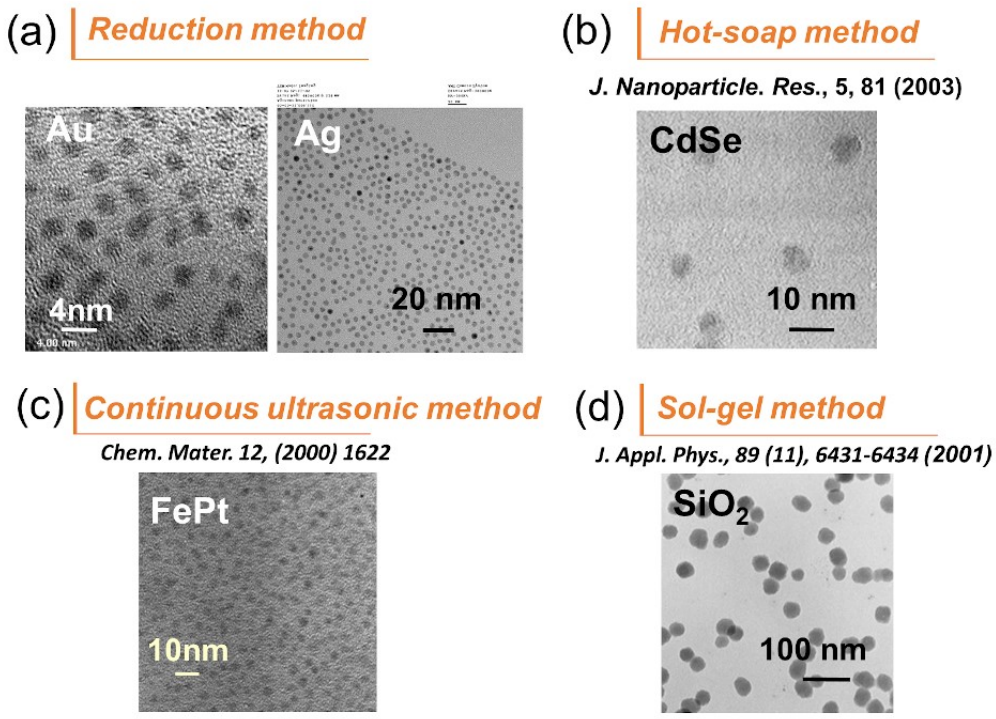

Figure 1.3 Typical particle images using the liquid-phase process: (a) reduction method, (b) hot-soap method, (c) continuous ultrasonic method, and (d) sol–gel method.

1.2.3 Solid-phase process

Conventional solid-phase processes using a bead-milling apparatus requires high energy consumption to promote chemical reactions among the material ingredients. This method results in the active surface of particles, which causes mechanical high-energy reactions locally and instantaneously. This is called the mechanochemical effect [32].

Solid-phase synthesis could be classified into dry and wet processing. In the dry process, the apparatus is simple and it is easy to identify the mechanochemical effects. Recently, all solid-state secondary batteries, such as Na_3PS_4 [33], have been reported to use a dry milling process. However, the cost of the process is inefficient because a long operation time was needed and the limitation of particle size refinement is about 0.1 micron. In the wet process, it is effective for dispersion and easily obtains nanoparticles.

The disadvantage of solid-phase synthesis including dry and wet processes is the contamination from balls, inhomogeneity in samples, insertion of defects, and irregularly shaped particles. Recently, many reports have used numerical simulation, such as the discrete element method (DEM) and computational fluid dynamics (CFD), to understand the dynamic and breakage behaviors in the milling process [34,35].

1.3 Application of Nanoparticles for near-infrared shielding

1.3.1 Near-infrared shielding materials

Near-infrared (NIR) light comprises more than half of the energy of the sunlight arriving at the Earth's surface. Thus, development of NIR-absorbing materials is required for efficient use and control of sunlight. NIR-shielding materials (*e.g.*, tin-doped indium oxide (ITO), antimony tin oxide (ATO)) are well known [36]. Recently, lanthanum hexaboride (LaB_6) [37] and cesium tungsten oxide (CWO®) [2,3] nanoparticles were commercialized by SMM because of the remarkable absorption property in the NIR

region with a high transmittance of the visible region.

Based on the properties of selective NIR absorption, CWO® could be widely applied to solar control films on windows of automobiles and buildings by being embedded in binder resins (**Figure 1.4(a)**). To improve safety, CWO® film was sandwiched between two glass plates (*i.e.*, interlayer glass) for hybrid (HV) and electric vehicles (EV) (**Figure 1.4(b)**). Furthermore, the CWO® film was developed for optical filters (**Figure 1.4(c)**), digital printing (**Figure 1.4(d)**), and photothermal conversion (**Figure 1.4(e)**).

To predict the trends in CWO® nanoparticles, **Figure 1.5** shows that the number of cited papers in the Web of Science using keyword of cesium tungsten bronze and infrared absorption. CWO® research, such as the clarification of NIR absorption, developing new applications, and composite materials, will expand in future because of the excellent absorption property.

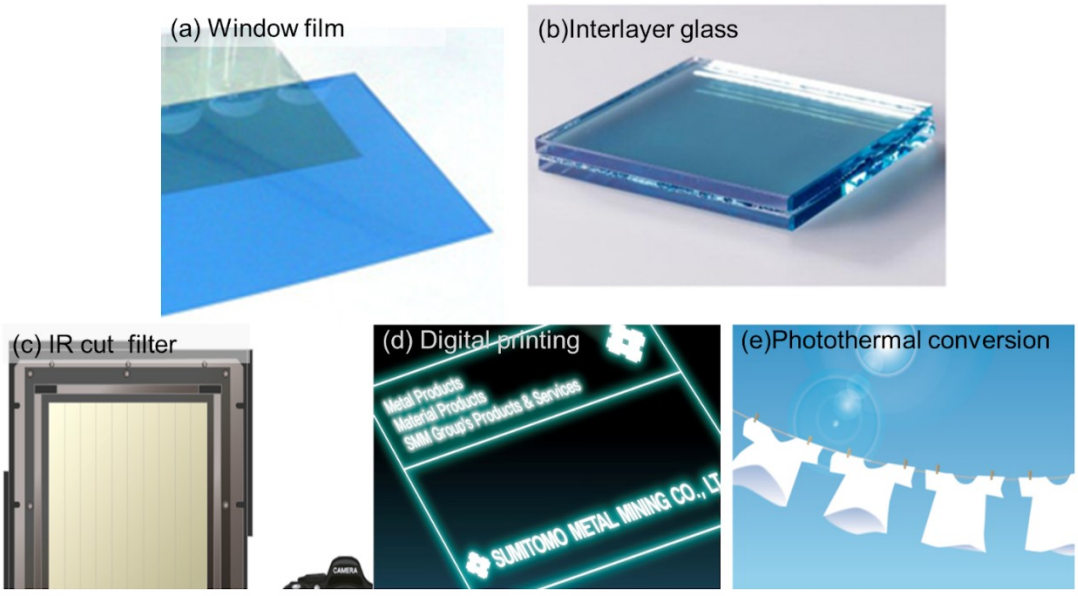

Figure 1.4 Examples of CWO® applications: (a) window film, (b) interlayer glass, (c) IR cut filter, (d) digital printing, and (e) photothermal conversion.

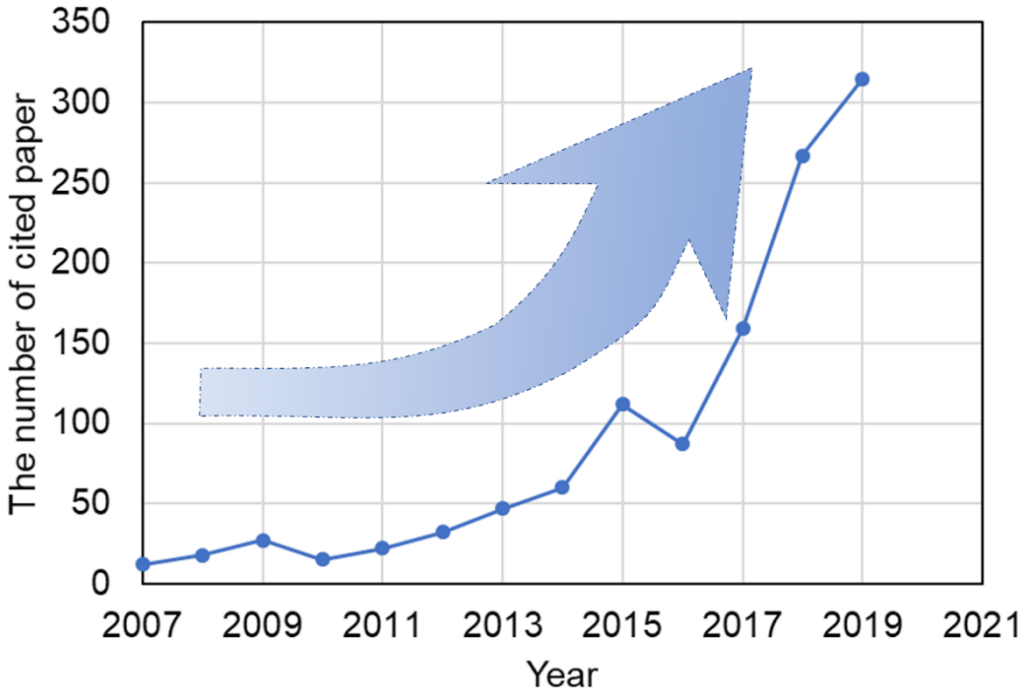

Figure 1.5 The number of cited papers related to cesium tungsten bronze for near infrared absorption materials.

1.3.2 Characteristics of $Cs_{0.32}WO_3$

The space group of $Cs_{0.32}WO_3$ crystal is *P6₃/mcm*, and the International Centre for Diffraction Data (ICDD) number is 04-009-6455. Cs atoms are positioned in the center of the hexagonal cavities (**Figure 1.6(a)**). The $Cs_{0.32}WO_3$ crystal structure is constituted from the c planes including Cs atoms and W atoms alternatingly (**Figure 1.6(b)**). The oxygen atoms contained in the c planes including Cs atoms and W atoms are labeled O(1) and O(2), respectively.

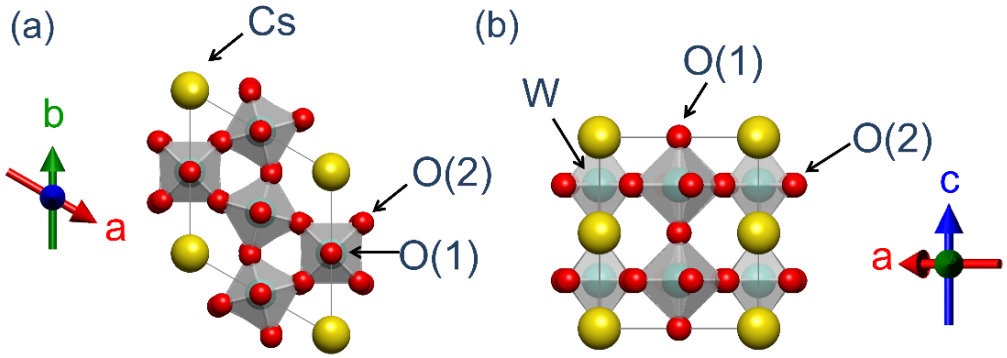

Figure 1.6 Crystal structure of $Cs_{0.32}WO_3$ (a) projection from c axis, (b) projection from b axis.

$Cs_{0.32}WO_3$ nanoparticles for NIR-absorbing materials can be synthesized by various methods (**Table 1.2**), *i.e.*, solid-phase synthesis [2] and thermal decomposition [38]. These methods are then followed by liquid-phase synthesis [39,40], such as the hydro- [41,42] and solvothermal methods [43,44], and by vapor-phase synthesis, such as the electrospinning [45], FASP [46] and TPS methods [47].

Table 1.2 Synthesis method and $Cs_{0.32}WO_3$ particle characteristics.

Method	Target materials	Tungsten and cesium sources	Experimental conditions	Size and morphology	References
Solid-phase synthesis	$Cs_{0.33}WO_3$	Tungstic acid (H_2WO_4), Cesium carbonate (Cs_2CO_3)	Heated at 650 °C in H_2/N_2, and 800 °C in N_2	50–100 nm, Irregular	[2]
Thermal decomposition	$Na_xCs_yWO_3$	Ammonium metatungstate hydrate (AMT), Cesium hydroxide ($CsOH·H_2O$)	In N_2 heated at 250 °C with oleylamine	Average 32 nm, irregular	[38]
Simple liquid-phase synthesis	$Cs_{0.33}WO_3$	Tungsten chloride (WCl_4), Cesium chloride (CsCl)	Heated at 300 °C with oleic acid	10–30 nm, hexagonal prisms	[39]
Solution mixing method	$Na_xCs_yWO_3$	Cesium sulfate (Cs_2SO_4), CsCl, $CsOH·H_2O$, cesium acetate	Heated at 260 °C with oleic acid	5–20 nm, nanorods, truncated tetrahedron	[40]
Hydrothermal method	Cs_xWO_3	Sodium Tungstate ($Na_2WO_4·2H_2O$), Cs_2CO_3	Heated at 190 °C, and 500 °C in N_2	>1 μm	[41]
Hydrothermal method	$Cs_xWO_{3-x}F_x$	$Na_2WO_4·2H_2O$, hydrofluoric acid (HF), Cs_2CO_3	Heated at 190 °C, and 60 °C for drying	20–300 nm, nanorods	[42]
Solvothermal process	Cs_xWO_3	WCl_4, $CsOH·H_2O$	Heated at 200 °C with ethanol	15–50 nm, nanorods	[43]
Solvothermal process	Pt-doped Cs_xWO_3	$Na_2WO_4·2H_2O$, Cs_2SO_4, and H_2PtCl_6	Heated at 190 °C with citric acid	10–80 nm, nanorods	[44]
Electrospinning method	Cs_xWO_3	H_2WO_4, Cs_2CO_3	The voltage was applied at 20 kV	Several μm, nanofiber	[45]
Flame assisted Spray pyrolysis	$Cs_{0.33}WO_3$	ATP, Cs_2CO_3	Flame field around 1000 °C and heated at 650 °C in H_2/Ar	80 nm, hexagonal prisms	[46]
Thermal plasma method	$Cs_{0.33}WO_3$	ATP, Cesium formate (CsCOOH)	Plasma field operating at 65 kW	50–500 nm	[47]
Spray pyrolysis	$Cs_{0.33}WO_3$	ATP, Cs_2CO_3	Heated at 1200 °C, and 650 °C in H_2/Ar	20–100 nm, hexagonal prisms	This study

The NIR-absorption properties of $Cs_{0.32}WO_3$ nanoparticles are based on electrons supplied from Cs and oxygen deficiency (V_O) to W-5*d* orbitals. Machida *et al.* [48,49] reported the peak separation of infrared absorption bands by Mie's scattering analysis considering the anisotropic effect and ensemble inhomogeneity of the nanoparticles, which indicates that the free electrons supplied from Cs are mainly responsible for localized surface plasmon resonance (LSPR) absorption and localized electrons because of generation of V_O are responsible for polaron absorption. Yoshio *et al.* [50,51] also clarified that polaronic absorption based on V_O was derived from localized electrons in W-5*d* orbitals using first-principles calculations.

1.3.3 Drawbacks of $Cs_{0.32}WO_3$

Photochromic (PC) materials are defined by their ability to change optical properties by interaction with external light. Similarly, an electrochromic (EC) material [52] and a thermochromic (TC) material are known as chromatic materials that change color by electricity and heating, respectively. PC materials such as WO_3, MoO_3 [53], and V_2O_5 [54] have been applied in the development of smart windows [55], colorimetric sensors [56], and PC eyewear [57] because of their reversible changes in color using only light. The color change in WO_3 was attributed to the formation of a bronze structure (e.g., A_xWO_3, where A = H, Na). In particular, the PC mechanism of WO_3 was revealed to be due to the injection of electrons through the intercalation of hydrogen atoms [58].

In the case of $Cs_{0.32}WO_3$ nanoparticles, which already formed a bronze structure with a slight bluish color, they changed to a further bluish coloration under UV irradiation (**Figure 1.7**). This change was caused by the diffusion of H^+ ions from the resin matrix to amorphous or crystalline Cs-deficient sites [59] present in the particle surface at a depth of a few nm [60]. Because the H_xWO_3 phase on the surface of $Cs_{0.32}WO_3$ nanoparticles

strongly absorbs red light, the color of the particles turns to deep blue.

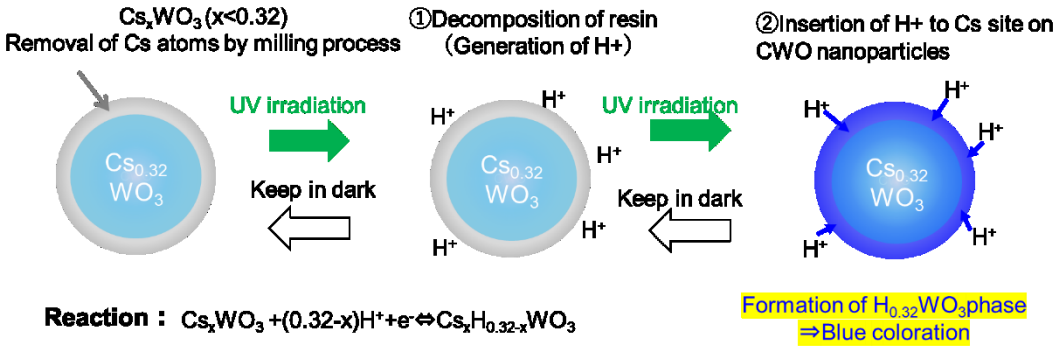

Figure 1.7 The mechanism of deep blue coloration under UV irradiation.

1.4 Objective and outline of the dissertation

This dissertation aims to synthesize tungsten oxide nanoparticles and $Cs_{0.32}WO_3$ nanoparticles using the spray pyrolysis method and evaluate their optical properties, such as NIR absorption and PC response. The presence of tungsten deficiency in $Cs_{0.32}WO_3$ nanoparticles using the rapid quenching process of the spray pyrolysis method is demonstrated for the first time as a novel finding. Notably, the relation between tungsten deficiency in tungsten bronze crystals and NIR-absorption properties were clarified in detail. Finally, the PC properties of $Cs_{0.32}WO_3$ nanoparticles derived using the spray pyrolysis method were compared with that of the solid-phase method.

The schematic diagram of the organization and structure of this dissertation in five chapters is shown below (**Figure 1.8**).

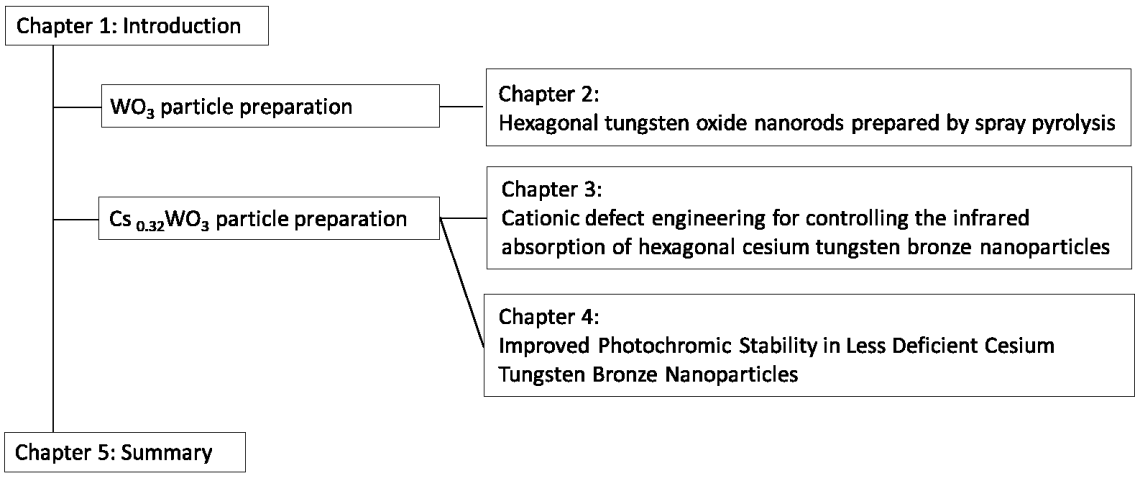

Figure 1.8 Chapter organization

In Chapter 2, hexagonal tungsten oxide nanorods were synthesized using the spray pyrolysis method. The effects of the reaction time of spray pyrolysis on the size, morphology, and crystal phase of tungsten oxide nanoparticles were investigated. The extended residence time in the spray pyrolysis method enables the direct synthesis of single-phase hexagonal tungsten oxide nanorods. Furthermore, the N_2 and CO_2 absorption properties were evaluated to confirm the hexagonal channels in hexagonal tungsten oxide.

In Chapter 3, $Cs_{0.32}WO_3$ nanoparticles including tungsten deficiency were produced using the spray pyrolysis method. We investigated the effect of tungsten deficiency on lattice constants and NIR-absorption properties in detail.

In Chapter 4, the PC stability of $Cs_{0.32}WO_3$ nanoparticles was investigated because the critical issue for industrial applications is a blue coloration when UV light was irradiated. We demonstrated that the less Cs-deficient $Cs_{0.32}WO_3$ particles synthesized using the spray pyrolysis method exhibit improved PC stability compared with that of the solid-phase method.

A summary of this work and insights for future research are presented in Chapter 5.

1.5 References

[1] T. Ogi, K.Okuyama, *Structurization and Control of Nanoparticle Material towards their Application*. FUNTAI GIJUTSU, 4 (2012) 1075-1085.

[2] H. Takeda, K. Adachi, *Near Infrared Absorption of Tungsten Oxide Nanoparticle Dispersions*, Journal of the American Ceramic Society, 90 (2007) 4059-4061.

[3] H. Takeda, K. Adachi, US patent, 2010, No. 7655301

[4] T. Ogi, A.B.D. Nandiyanto, K. Okuyama, *Nanostructuring strategies in functional fine-particle synthesis towards resource and energy saving applications*, Advanced Powder Technology, 25 (2014) 3-17.

[5] K. Okuyama, I. W. Lenggoro, *Preparation of nanoparticles via spray route*, Chemical Engineering Science, 58 (2003) 537-547.

[6] M.T. Swihart, *Vapor-phase synthesis of nanoparticles*, Current Opinion in Colloid & Interface Science, 8 (2003) 127-133.

[7] K. Okuyama, K. Nakaso, The micromeritics, 45 (2001) 31-40.

[8] A. Reina, et al., *Large area, few-layer graphene films on arbitrary substrates by chemical vapor deposition*, Nano letters 9 (2008) 30-35.

[9] X. Ling, et al., *Role of the seeding promoter in MoS_2 growth by chemical vapor deposition.* Nano letters 14 (2014) 464-472.

[10] T. Hashizume et al., *Chemistry and electrical properties of surfaces of GaN and GaN/AlGaN heterostructures*. Journal of Vacuum Science & Technology B: Microelectronics and Nanometer Structures Processing, Measurement, and Phenomena 19 (2001) 1675-1681.

[11] K. Okuyama, et al., *Particle generation in a chemical vapor deposition process with seed particles*. AIChE journal 36 (1990) 409-419.

[12] C. Vahlas, B. Caussat, P. Serp, G. N. Angelopoulos, *Principles and applications of*

CVD powder technology Materials Science and Engineering. R, 53 (2006) 1-72.

[13] J. Zhang, R. Tu, and T. Goto, *Preparation of carbon nanotube by rotary CVD on Ni nano-particle precipitated cBN using nickelocene as a precursor*. Materials letters 65 (2011) 367-370.

[14] T. Goto, B. Ryan, and T. Kimura, *Morphology and preferred orientation of Y_2O_3 film prepared by high-speed laser CVD.* Surface and Coatings Technology 201 (2007) 5776-5781.

[15] Y. Li, et al., *Preferential growth of semiconducting single-walled carbon nanotubes by a plasma enhanced CVD method*. Nano Letters 4 (2004) 317-321.

[16] H. Katsui, and T. Goto, *Coatings on ceramic powders by rotary chemical vapor deposition and sintering of the coated powders*. Journal of the Ceramic Society of Japan 126 (2018) 413-420.

[17] Y. C. Kong, et al. *Ultraviolet-emitting ZnO nanowires synthesized by a physical vapor deposition approach*. Applied Physics Letters 78 (2001) 407-409.

[18] B. Xia, I. W. Lenggoro and K. Okuyama, *Novel Route to Nanoparticle Synthesis by Salt-Assisted Aerosol Decomposition*, Advanced Materials, 13 (2001) 1579-1582.

[19] B. Xia, I.W. Lenggoro and K. Okuyama, *Synthesis of CeO_2 Nanoparticles by Salt-Assisted Ultrasonic Aerosol Decomposition*, Journal of Material Chemistry, 13(2001) 2925-2927.

[20] Y. Itoh, I. W. Lenggoro, K. Okuyama, L. Madler and S. E. Pratsinis, *Size Tunable Synthesis of Highly Crystalline $BaTiO_3$ nanoparticles using Salt-Assisted Spray Pyrolysis*, Journal of Nanoparticle Research, 5(2003) 191-198.

[21] C. Panatarani, I. W. Lenggoro and K. Okuyama, *Synthesis of single crystalline ZnO nanoparticles by salt-assisted spray pyrolysis*, Journal of Nanoparticle Research, 5(2003), 47-53.

[22] T. Ogi, *Approaches and Issues o Nanostructuralization of Fine Particles*, Journal of the Society of Powder Technology, Japan, 56 (2019) 109-116.

[23] A.B.D. Nandiyanto, et al., *Template-assisted spray-drying method for the fabrication of porous particles with tunable structures*. Advanced Powder Technology, 30 (2019) 2908-2924.

[24] A. M. Rahmatika, et al., *Energy-efficient templating method for the industrial production of porous carbon particles by a spray pyrolysis process using poly (methyl methacrylate)*. Industrial & Engineering Chemistry Research 57 (2018) 11335-11341.

[25] S. E. Pratsinis, *History of manufacture of fine particles in high-temperature aerosol reactors.* Aerosol science and technology: History and reviews, RTI international, USA (2011) 475-507.

[26] L. Mädler, et al., *Controlled synthesis of nanostructured particles by flame spray pyrolysis.* Journal of Aerosol Science 33 (2002) 369-389.

[27] W.Y. Teoh, R. Amal, L. Mädler, *Flame spray pyrolysis, An enabling technology for nanoparticles design and fabrication*, Nanoscale, 2 (2010) 1324-1347.

[28] K. Fujiwara. *Atomically Dispersed Pd or Highly Loaded Ag Clusters on TiO_2 by Flame Spray Pyrolysis*, Journal of the Society of Powder Technology, Japan, 56 (2019) 403-408.

[29] M. Tanaka, T. Watanabe, *Achievement of Mass Production System of Attractive Nanoparticles by Thermal Plasmas*, Journal of the Society of Powder Technology, Japan, 56 (2019) 109-116.

[30] S. Diodati, et al., *Pursuing the crystallization of mono-and polymetallic nanosized crystalline inorganic compounds by low-temperature wet-chemistry and colloidal routes*. Chemical reviews 115 (2015) 11449-11502.

[31] Y. Hayashi, *Metal Nanoparticle Related Material Processing by Synergistic Effects of Solid-Liquid System and Ultrasound, Microwave Reactor—Innovative Nanomaterial Fabrication Joining Environment*, Low Cost and High Throughput—, Journal of the Society of Powder Technology, Japan, 56 (2019) 409-416.

[32] A. Sakuda, A. Hayashi, M. Tatsumisago, *Development of Next Generation Battery Materials by Mechanochemical Process*, Journal of the Society of Powder Technology, Japan, 56 (2019) 452-458.

[33] A. Hayashi, *Superionic glass-ceramic electrolytes for room-temperature rechargeable sodium batteries*. Nature communications 3 (2012) 856.

[34] T, Tsuji, K. Yabumoto, and T. Tanaka, *Spontaneous tructures in three-dimensional bubbling gas-fluidized bed by parallel DEM–CFD coupling simulation*. Powder Technology, 184 (2008) 132-140.

[35] K. Kushimoto, S. Ishihara, and J. Kano., *Development of ADEM–CFD model for analyzing dynamic and breakage behavior of aggregates in wet ball milling*. Advanced Powder Technology 30 (2019) 1131-1140.

[36] K. P. Sibin, et al., *Design and development of ITO/Ag/ITO spectral beam splitter coating for photovoltaic-thermoelectric hybrid systems*. Solar Energy 141 (2017) 118-126.

[37] H. Takeda, H. Kuno, and K. Adachi., *Solar Control Dispersions and Coatings With Rare-Earth Hexaboride Nanoparticles.* Journal of the American Ceramic Society, 91 (2008) 2897-2902.

[38] J. Choi, K. Moon, I. Kang, S. Kim, P.J. Yoo, K.W. Oh, J. Park, *Preparation of quaternary tungsten bronze nanoparticles by a thermal decomposition of ammonium metatungstate with oleylamine*, Chemical Engineering Journal, 281 (2015) 236-242.

[39] T. M. Mattox, et al., *Influence of shape on the surface plasmon resonance of tungsten bronze nanocrystals*. Chemistry of Materials 26 (2014) 1779-1784.

[40] X.-J. Huang, J. Bao, Y. Han, C.-W. Cui, J.-X. Wang, X.-F. Zeng, J.-F. Chen, *Controllable synthesis and evolution mechanism of tungsten bronze nanocrystals with excellent optical performance for energy-saving glass*, Journal of Materials Chemistry C, 6 (2018) 7783-7789.

[41] F. Shi, J. Liu, X. Dong, Q. Xu, J. Luo, H. Ma, *Hydrothermal Synthesis of Cs_xWO_3 and the Effects of N_2 Annealing on its Microstructure and Heat Shielding Properties*, Journal of Materials Science & Technology, 30 (2014) 342-346.

[42] J. Liu, J. Luo, F. Shi, S. Liu, C. Fan, Q. Xu, G. Shao, *Synthesis and characterization of F-doped $Cs_{0.33}WO_{3-x}F_x$ particles with improved near infrared shielding ability,* Journal of Solid State Chemistry, 221 (2015) 255-262.

[43] C. Guo, S. Yin, P. Zhang, M. Yan, K. Adachi, T. Chonan, T. Sato, *Novel synthesis of homogenous Cs_xWO_3 nanorods with excellent NIR shielding properties by a water controlled-release solvothermal process,* Journal of Materials Chemistry, 20 (2010) 8227-8229.

[44] J. Liu, S. Ran, C. Fan, Y. Qiao, F. Shi, J. Yang, B. Chen, S. Liu, *One pot synthesis of Pt-doped Cs_xWO_3 with improved near infrared shielding for energy-saving film applications*, Solar Energy, 178 (2019) 17-24.

[45] N. Tahmasebi, S. Madmoli, P. Farahnak, *Synthesis of cesium tungsten bronze nanofibers with different crystalline phases*, Materials Letters, 211 (2018) 161-164.

[46] T. Hirano, S. Nakakura, F.G. Rinaldi, E. Tanabe, W.-N. Wang, T. Ogi, *Synthesis of highly crystalline hexagonal cesium tungsten bronze nanoparticles by flame-assisted spray pyrolysis*, Advanced Powder Technology, 29 (2018) 2512-2520.

[47] M. Mamak, S.Y. Choi, U. Stadler, R. Dolbec, M. Boulos, S. Petrov, *Thermal plasma*

synthesis of tungsten bronze nanoparticles for near infra-red absorption applications, Journal of Materials Chemistry, 20 (2010) 9855-9857.

[48] K. Machida, and K. Adachi, *Ensemble inhomogeneity of dielectric functions in Cs-doped tungsten oxide nanoparticles*. Journal of Physical Chemistry C, 120 (2016) 16919-16930.

[49] K. Machida, M. Okada, and K. Adachi, *Excitations of free and localized electrons at nearby energies in reduced cesium tungsten bronze nanocrystals*. Journal of Applied Physics, 125(2019) 103103.

[50] S. Yoshio, M. Okada, and K. Adachi, *Destabilization of pseudo-Jahn–Teller distortion in cesium-doped hexagonal tungsten bronzes*. Journal of Applied Physics 124 (2018) 0063109.

[51] S. Yoshio, and K. Adachi, *Polarons in reduced cesium tungsten bronzes studied using the DFT method*. Materials Research Express 6 (2019) 0126548.

[52] C. G. Granqvist, *Electrochromic tungsten oxide films: review of progress 1993–1998*. Solar Energy Materials and Solar Cells, 60 (2000) 201-262.

[53] S. Li, et al., *Synthesis and characterization of photochromic molybdenum and tungsten oxide nanoparticles*. Nanostructured Materials, 12 (1999) 215-219.

[54] S. Nishio, et. Al., *Evidence for visible light photochromism of V_2O_5*. Chemistry of materials, 14(2002) 3730-3733.

[55] C. G. Granqvist, *Chromogenic materials for transmittance control of large-area windows*. Critical Reviews in Solid State and Material Sciences, 16 (1990) 291-308.

[56] S. Tanaka, et.al., *Surface-enhanced photochromic phenomena of phenylalanine adsorbed on tungsten oxide nanoparticles: a novel approach for "label-free" colorimetric sensing*. Analyst, 138(2013) 2536-2539.

[57] A. M. Österholm, et. al., *Four shades of brown: tuning of electrochromic polymer blends toward high-contrast eyewear.* ACS applied materials & interfaces, 7(2015) 1413-1421.

[58] R. J. Colton, et. al., *Photochromism and electrochromism in amorphous transition metal oxide films.* Accounts of Chemical Research, 11(1978), 170-176.

[59] K. Adachi, et. al., *Chromatic instabilities in cesium-doped tungsten bronze nanoparticles*. Journal of Applied Physics, 114(2013), 194304.

[60] Y. Sato, M. Terauchi, and K. Adachi. *High energy-resolution electron energy-loss spectroscopy study on the near-infrared scattering mechanism of* $Cs_{0.33}WO_3$ *crystals and nanoparticles.* Journal of Applied Physics 112 (2012) 074308.

Chapter 2

Direct Synthesis of Highly Crystalline Single-phase Hexagonal Tungsten Oxide Nanorods by Spray Pyrolysis*

2.1 Introduction

Tungsten oxide (WO_3) is known as both a visible light-responsive photocatalytic and electrochromic material [1-10]. Various crystal phases of WO_3 have been reported, including monoclinic, hexagonal, orthorhombic, tetragonal, and cubic. Among these crystal phases, monoclinic WO_3 (m-WO_3), as shown in **Figure 2.1(a)**, is stable at room temperature. Currently, the development of WO_3 particles has focused on increasing their reactivity. Formation of nanoparticles and nanostructures with well-ordered morphologies is one way to address this issue [11]. Introduction of hexagonal channels into the crystal structure of WO_3 particles is another promising approach to increase their reactivity [12]. Hexagonal channels can be obtained in WO_3 by controlling the atom coordination geometries (polyhedra) in the crystal structure, as illustrated in **Figure 2.1(b)**. The hexagonal channels promote intercalation reactions, leading to high reactivity. Hexagonal tungsten oxide (h-WO_3) particles usually exhibit higher specific surface areas compared with those of m-WO_3 particles of similar size because of the presence of hexagonal channels. Specific surface areas of h-WO_3 particles of up to 47 m^2/g have been reported [13]. The hexagonal channels in h-WO_3 can react selectively with either

ammonia or lithium ions, meaning that h-WO_3 has potential applications in selective gas sensing [14,15] and lithium-ion batteries [16,17], respectively.

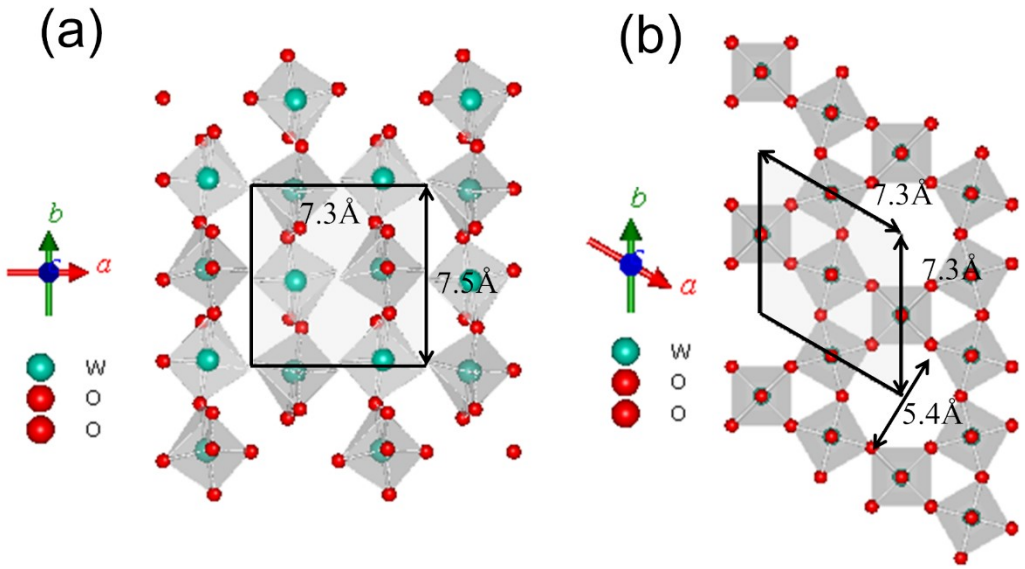

Figure 2.1 Crystal structures of (a) m-WO_3 and (b) h-WO_3.

Figlarz's group first synthesized h-WO_3 in 1978 using a hydrothermal reaction method [18]. Thereafter, other methods to prepare h-WO_3 were developed, such as thermal oxidation of ammonium tungsten bronze [19,20] or tungsten metal as the WO_3 source [21], spray pyrolysis [22,23], and another hydrothermal method [24]. In particular, spray pyrolysis is an efficient method for industrialization because particles can be synthesized continuously and rapidly [25,26]. For example, Ortega et al. [22] synthesized a WO_3 membrane containing a mixture of h-WO_3 and m-WO_3 phases by pulsed spray pyrolysis. However, their research focused on the formation of WO_3 membranes that contained the unreactive m-WO_3 phase.

Our group developed a spray pyrolysis process to synthesize WO_3 particles using ammonium para-tungstate pentahydrate (ATP) as a precursor [23]. Fine m-WO_3 particles

were obtained in the temperature range of 600–1000 °C. h-WO_3 began to form when the maximum furnace temperature was increased to 1000–1300 °C. In this temperature range, the particle surface segregated and formed h-WO_3 nanoparticles, as illustrated in the upper part of **Figure. 2.2**. However, the final particles still contained the m-WO_3 phase because of the incomplete particle segregation even at a maximum furnace temperature of 1300 °C. These results led to a hypothesis that the synthesis conditions could not supply sufficient energy to completely segregate intermediate WO_3 particles and promote the formation of h-WO_3.

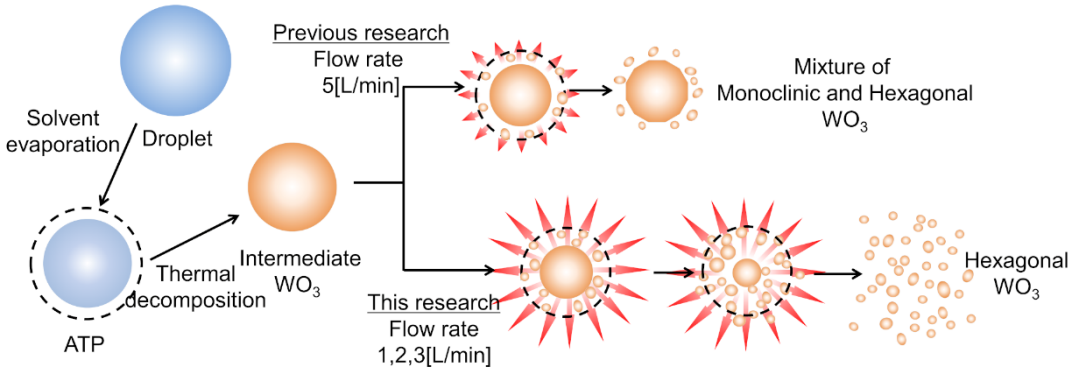

Figure 2.2 Schematic diagram of the surface and complete segregation of WO_3 nanoparticles during spray pyrolysis.

The present study improves on our previously developed spray pyrolysis process with the aim of producing single-phase h-WO_3 nanoparticles. Simply raising the furnace temperature is not feasible from the viewpoints of energy consumption and furnace durability. Based on this consideration, we addressed the issue of the insufficient energy supply to produce pure h-WO_3 by extending the segregation time. For this purpose, the effect of the carrier gas flow rate on the crystal phase produced is investigated. The gas adsorption ability of the synthesized nanoparticles is then examined to confirm the

advantageous adsorption behavior of h-WO_3 over that of m-WO_3. This study represents a promising step towards the scaled-up production of single-phase h-WO_3 nanoparticles.

2.2 Experimental

2.2.1 Preparation of h-WO_3

A solution of ATP [$(NH_4)_{10}(W_{12}O_{41})$•$5H_2O$; purity 88%–90%; Kanto Chemical Co., Inc., Tokyo, Japan] in ultrapure water with a concentration of 10 mmol/L was used as the main precursor. The spray pyrolysis reactor system consisted of an ultrasonic nebulizer (NE-U17; Omron Healthcare Co., Ltd., Tokyo, Japan) operated at 1.7 MHz as the droplet generator, a ceramic tube with a length of 1.3 m and inner diameter of 28.5 mm as the reactor, and a glass microfiber filter as the particle collector.

The precursor solution was pumped into the ultrasonic nebulizer at a flow rate of 1.5 mL/min. The temperature of the nebulizer was kept at 40 °C using a circulating water cooling system. The generated droplets were fed into the tubular furnace using air as the carrier gas. The air was supplied from a gas bottle at room temperature and a flow rate of 1–3 L/min. The air flow rate was controlled using a flow meter with a needle valve. At a carrier gas flow rate of 3 L/min, the atomization of 100 mL of precursor solution was completed after 1.1 h. For the same amount of precursor solution at a carrier gas flow rate of 1 L/min, it took 6 h to complete the atomization process. Based on the time required to complete the atomization, we estimated that the droplet generation rates were 1.5 and 0.27 mL/min at carrier gas flow rates of 3 and 1 L/min, respectively.

The tubular furnace was arranged horizontally and divided into five temperature zones; i.e., 200, 500, 700, 1200, and 1200 °C. The segregation time t_s is given by:

$$t_s = \frac{V_f}{Q_C} \qquad (1)$$

where V_f is volume of the tube at synthesis temperatures over 1000 °C and Q_C is carrier gas flow rate. The t_s values of particles in the furnace were 18.4, 9.2, and 6.1 s at Q_C of 1, 2, and 3 L/min, respectively. The change in Q_C slightly shifted the temperature profile towards the furnace end. This shift was considered in the calculation of t_s.

2.2.2 Characterization

The size, morphology, and structure of the prepared particles were characterized using scanning electron microscopy (SEM; 5–20 kV, S-5200, Hitachi High-Tech. Corp., Tokyo, Japan) and transmission electron microscopy (TEM; 297 kV, JEM-3000F, JEOL, Tokyo, Japan). The lattice spacing was calculated as the average of ten lattice spacing values measured from high-resolution transmission electron microscopy (HR-TEM) images using Gatan Digital Micrograph software (Gatan, München, Germany). The crystal phase of WO_3 particles was examined by X-ray diffraction (XRD; 40 kV and 30 mA, D2 PHASER, Bruker AXS GmbH, Karlsruhe, USA). The weight percentages of h-WO_3 and m-WO_3 phases were determined by Rietveld analysis using Total Pattern Analysis Solutions software (TOPAS; Bruker AXS GmbH, Karlsruhe, Germany) considering these crystal phases. To investigate the specific surface area and presence of hexagonal channels in h-WO_3, nitrogen (N_2) and carbon dioxide (CO_2) adsorption analyses were conducted on a Belsorp 28SA analyzer (Bel Japan, Tokyo, Japan) at 77 K and 300 K, respectively. The surface areas of the particles were calculated using the Brunauer–Emmett–Teller (BET) method.

2.3 Results and Discussion

2.3.1 Synthesis of h-WO_3 nanoparticles

Q_c controls the droplet generation rate ($Q_{droplet}$) and t_s of particles in the furnace. $Q_{droplet}$

is an important factor in spray pyrolysis because it affects the frequency of collisions between the droplets [27]. The number of droplets per unit volume (n_{unit}) was calculated using the following formula,

$$n_{\mathrm{unit}} = \frac{Q_{\mathrm{droplet}}}{Q_{\mathrm{c}}} \frac{6}{\pi D^3} \qquad (2)$$

where D is the droplet diameter (4.5 μm [23]). When Q_{c} was 3 L/min, n_{unit} was $1.0 \times 10^{13}/\mathrm{m}^3$. The value of n_{unit} decreased to $5.8 \times 10^{12}/\mathrm{m}^3$ when Q_{c} was 1 L/min. As n_{unit} decreased, the frequency of collisions between the droplets lowered and the energy per unit volume of droplets from the furnace increased.

The XRD patterns of h-WO_3 and m-WO_3 nanoparticles synthesized using Q_{c} of 1–3 L/min are presented in **Figure. 2.3**. A mixture of h-WO_3 and m-WO_3 phases was observed for Q_{c} of 2 and 3 L/min. In contrast, only the h-WO_3 phase formed at the lowest Q_{c} of 1 L/min. The Rietveld analysis (**Figure 2.4**) indicated that the weight percentage of the h-WO_3 phase reached nearly single-phase h-WO_3 when Q_{c} was 1 L/min and decreased to 60.9 wt% and 32.5 wt% at higher Q_{c} of 2 and 3 L/min, respectively. The decreasing weight percentage of h-WO_3 was accompanied by an increasing fraction of m-WO_3. The presence of m-WO_3 indicates there was insufficient energy supply to completely segregate intermediate WO_3 particles into h-WO_3 nanoparticles at high Q_{c}. This may be attributed to the high n_{unit} ($1.0 \times 10^{13}/\mathrm{m}^3$) and short t_{s} of 9.2 and 6.1 s at Q_{c} of 2 and 3 L/min, respectively. Decreasing Q_{c} to 1 L/min increased t_{s} to 18.4 s and decreased n_{unit} to $5.8 \times 10^{12}/\mathrm{m}^3$. This long t_{s} in the maximum temperature zone was found to provide sufficient energy to the intermediate WO_3 particles to produce single-phase h-WO_3.

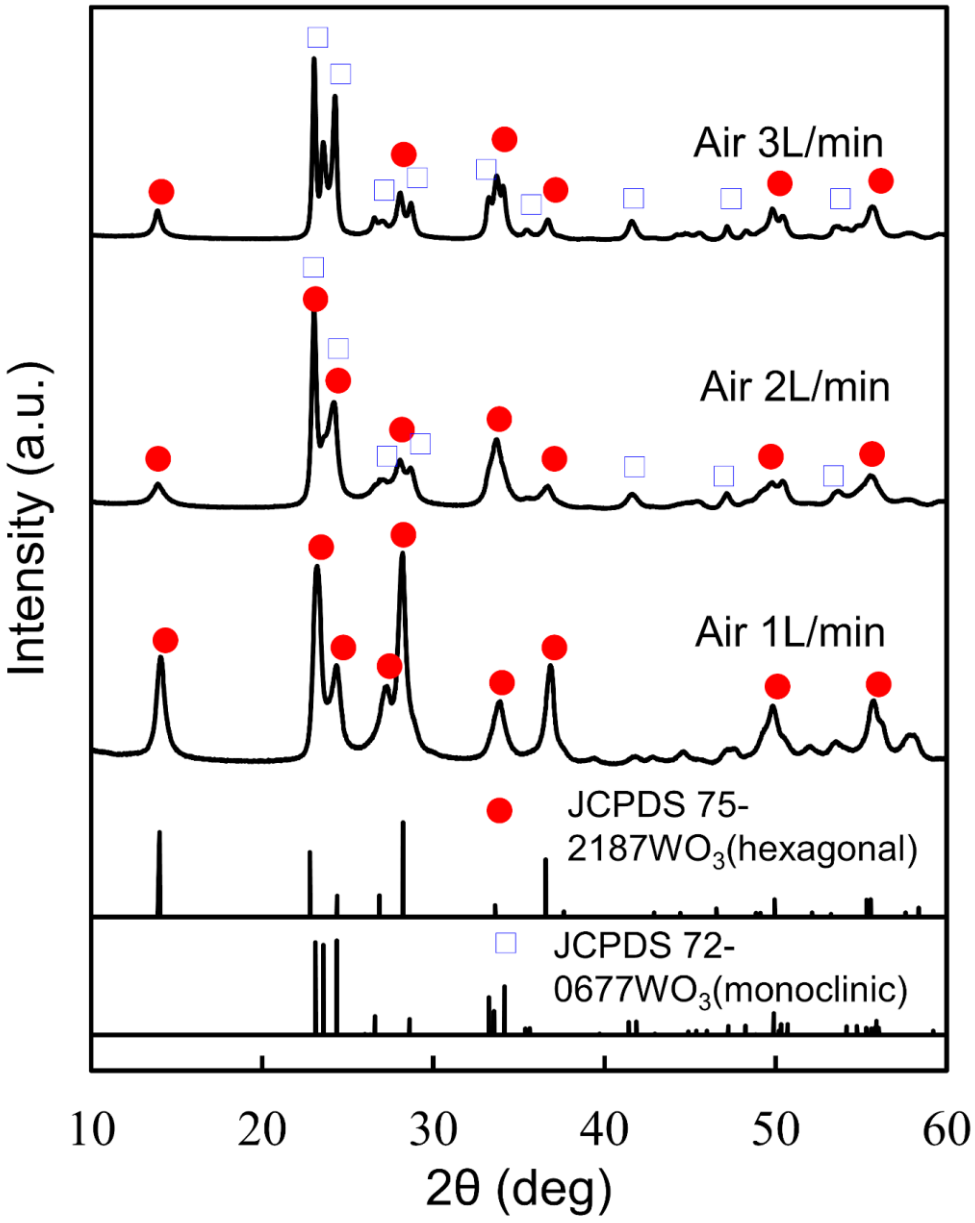

Figure 2.3 XRD patterns of WO_3 nanoparticles synthesized at various gas flow rates.

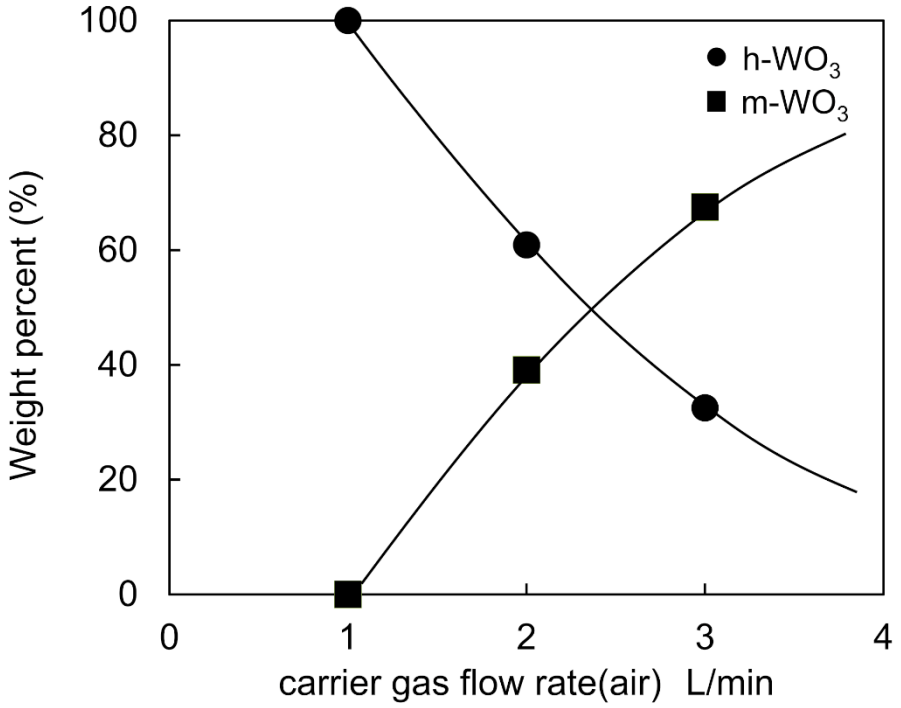

Figure 2.4 Weight percentages of h-WO_3 and m-WO_3 phases of WO_3 nanoparticles synthesized at various gas flow rates.

To investigate the atom coordination in the crystal structure and the morphology of the samples, SEM and TEM observations were conducted. **Figure 2.5** shows SEM images and particle size distributions of the WO_3 nanoparticles synthesized with Q_c of 1–3 L/min. When Q_c was 1 L/min, rod-like nanoparticles with lengths of about 100–200 nm and cuboid-shaped nanoparticles with a diameter of about 50 nm and various lengths were obtained (Fig. 3(a)). Square-shaped nanoparticles with lengths of 10–80 nm and rod-like nanoparticles with a length of about 80 nm were observed when Q_c was 2 L/min (Fig. 3(b)). Increasing Q_c to 3 L/min resulted in polygonal nanoparticles with sizes of 50–400 nm, as displayed in **Figure 2.5(c)**.

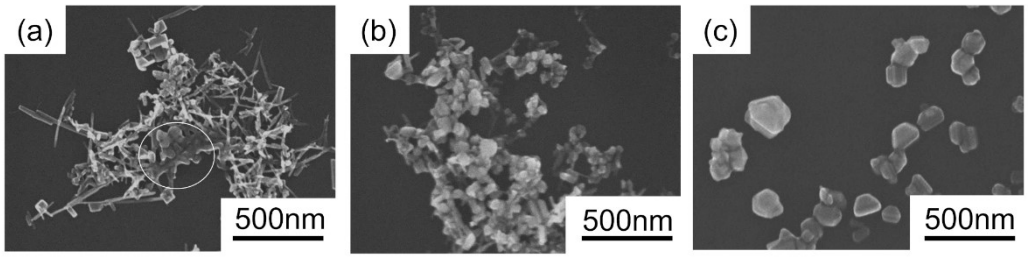

Figure 2.5 SEM images of WO_3 nanoparticles synthesized at carrier gas flow rates of (a) 1 L/min, (b) 2 L/min, and (c) 3 L/min.

A Q_c of 1 L/min gave rod-like nanoparticles with lengths of 100–200 nm and an aspect ratio of about ten (**Figure 2.6**). The corresponding HR-TEM image (**Figure 2.6(b)**) confirmed that the prepared nanoparticles had a uniform orientation with a lattice spacing of 0.67 nm. This is consistent with the *d* spacing of the (100) plane of h-WO_3. However, some vertical lines were observed in the fast Fourier transform (FFT) image (inset of **Figure 2.6(b)**), which indicates that the h-WO_3 nanoparticles contain stacking faults [5].

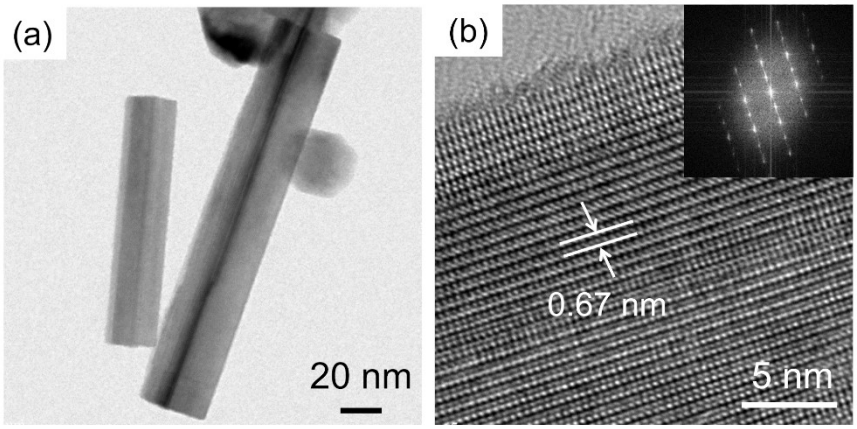

Figure 2.6 (a) TEM and (b) HR-TEM images of WO_3 nanoparticles prepared at carrier gas flow rates of 1 L/min. Insets of (b) display corresponding FFT images.

TEM images of the WO_3 nanoparticles synthesized at a Q_c of 3 L/min revealed the formation of polygonal nanoparticles with sizes of 50–200 nm, as presented in **Figure 2.7**. The HR-TEM image in **Figure 2.7(b)** shows that the polygonal nanoparticles contain changing contrast with sharp gradation. This gradation indicates the generation of grain boundaries inside the m-WO_3 nanoparticles. Both regions have the same lattice spacing of about 0.34 nm, but they have different directions. This shows that the synthesized m-WO_3 nanoparticles are not single crystals, which is caused by the insufficient energy present for single-crystal particle formation [23].

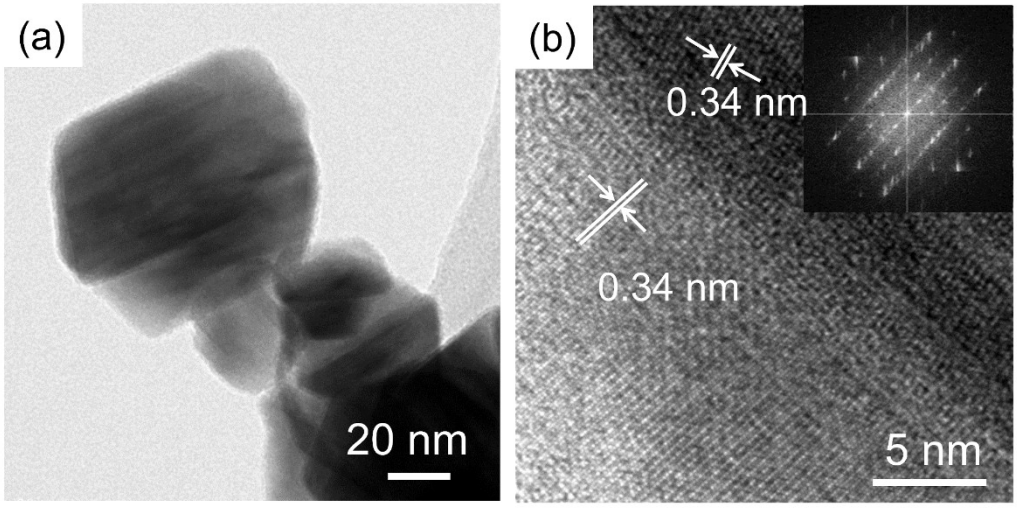

Figure 2.7 (a) TEM and (b) HR-TEM images of WO_3 nanoparticles prepared at carrier gas flow rates of 3 L/min. Insets of (b) display corresponding FFT images.

Based on the results presented above, a mechanism of nanoparticle formation through spray pyrolysis was proposed, as illustrated in **Figure 2.8**. Droplets containing ATP are sprayed into the furnace and react to form intermediate WO_3 particles after the solvent evaporates in the entrance of the furnace, which was set at a temperature of 200 °C. The crystallization process then occurs in the high temperature zone of the furnace, where the

temperature was set at 1200 °C. The reaction temperature in the high temperature zone affects the segregation behavior of intermediate WO_3 particles. When the maximum furnace temperature is less than 1000 °C, spherical m-WO_3 nanoparticles are obtained [23]. This particle formation mechanism was assumed to follow the one-droplet-to-one-particle principle [11,25]. When the maximum furnace temperature was 1000 °C or higher, more than one particle was generated from each intermediate WO_3 particle through segregation [23,28]. The t_s and n_{unit} values of intermediate WO_3 particles strongly affected the morphology and crystal phase of the final nanoparticles. At a high Q_c of 3 L/min, the precursor reacts immediately after being sprayed into the furnace. Because of the short t_s, segregation only occurs on the surface of the intermediate WO_3 particles; the inner part crystallizes as polygonal WO_3 nanoparticles. These nanoparticles tend to crystallize as phase regions with anisotropy in multiple directions rather than as a single crystal. The segregation phenomenon nearly reaches the center of the intermediate WO_3 particles when Q_c is decreased to 2 L/min. Therefore, the sizes of the obtained nanoparticles decreased to several tens of nanometers (Fig. 3(e)). In this case, polygonal WO_3 nanoparticles were still observed in the SEM image, which are probably m-WO_3 nanoparticles, along with rod-like h-WO_3 nanoparticles. At a low Q_c of 1 L/min, complete segregation occurs to mainly produce rod-like nanoparticles with lengths of several hundred nanometers and an aspect ratio of about ten because of the low n_{unit} and long t_s (Fig. 3(d)). The rod-like h-WO_3 nanoparticles contain stacking faults, suggesting that the crystal structure is greatly distorted from that of perfect h-WO_3 [18].

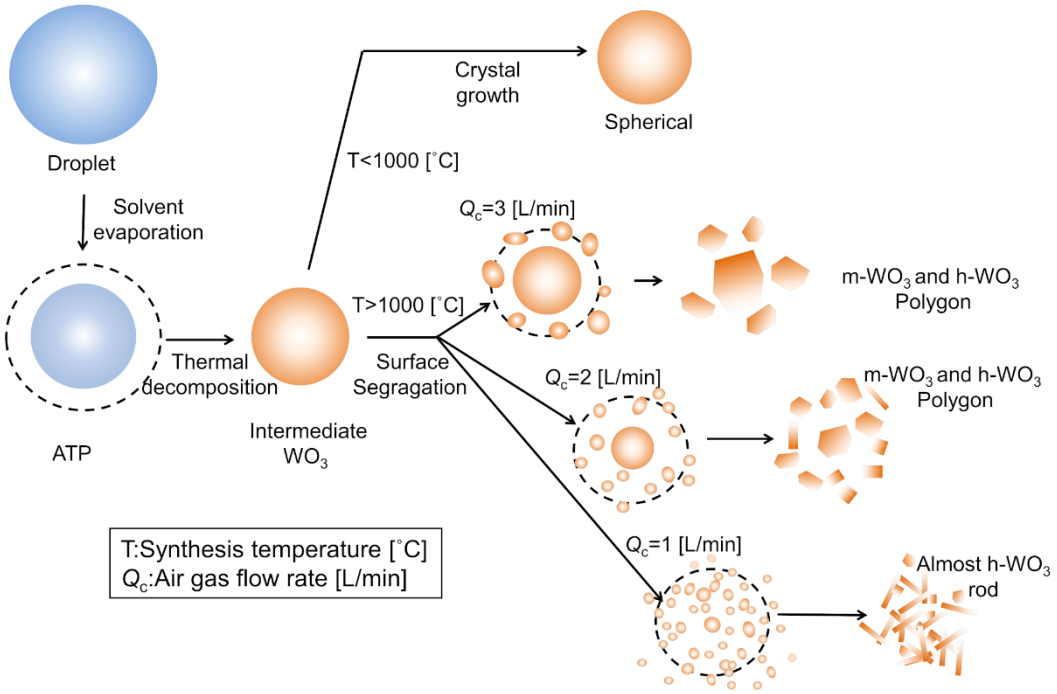

Figure 2.8 Formation mechanisms of WO_3 nanoparticles during spray pyrolysis.

2.3.2 Gas adsorption of h-WO₃ nanoparticles

Figure 2.9 shows the N_2 adsorption–desorption curves of WO_3 nanoparticles prepared with Q_c of 1 and 3 L/min. The obtained adsorption curves indicate that the WO_3 nanoparticles synthesized with a Q_c of 1 L/min adsorbed less gas molecules than those synthesized at 3 L/min. The specific surface areas (S_A) calculated using the BET method were about 12.8 and 17.2 m^2/g for nanoparticles prepared with Q_c of 1 and 3 L/min, respectively. S_A of the WO_3 nanoparticles synthesized at a Q_c of 1 L/min was smaller than that of the nanoparticles synthesized at a Q_c of 3 L/min. A possible reason for this result is sintering of the nanoparticles, as indicated by the white circle in **Figure 2.5 (a)**. As shown in Fig. 3(a) and (c), the sintering degree of nanoparticles prepared at a Q_c of 1 L/min was greater than that of the sample produced at a Q_c of 3 L/min because of the longer t_s.

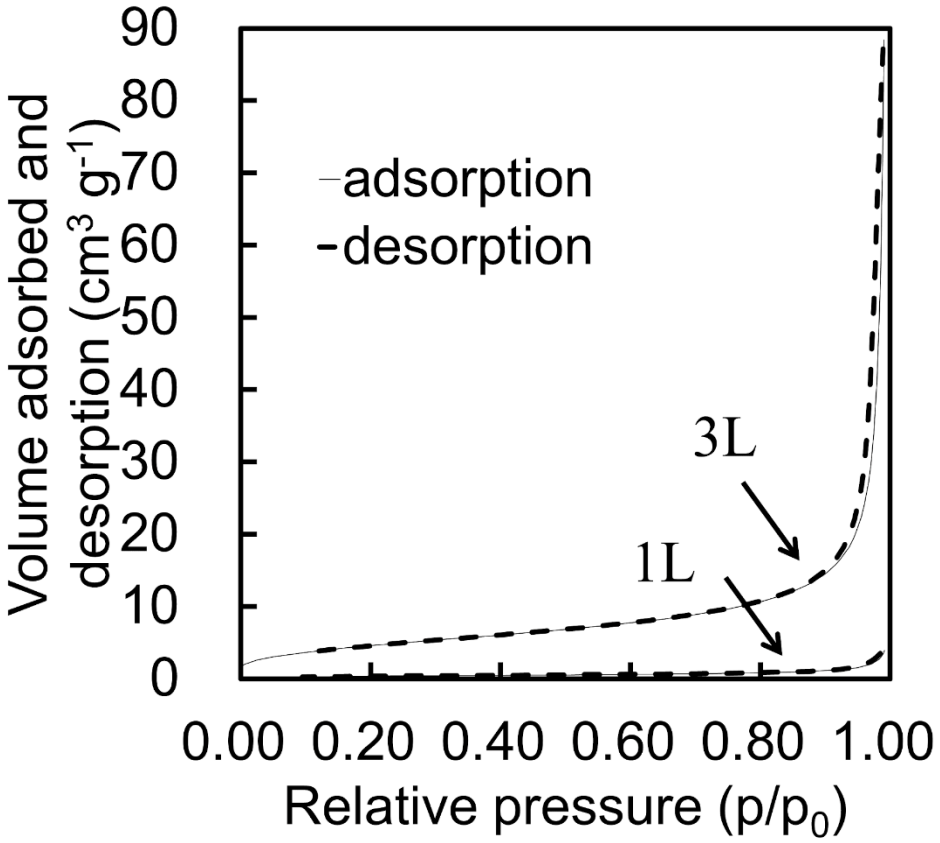

Figure 2.9 N_2 adsorption–desorption curves of WO_3 nanoparticles prepared at carrier gas flow rates of 1 and 3 L/min.

To confirm the presence of hexagonal channels in the h-WO_3 nanoparticles synthesized at a Q_c of 1 L/min, their CO_2 adsorption performance was also evaluated. **Figure 2.10** depicts the CO_2 adsorption of the sample, which displayed a CO_2 capture capacity of up to 0.32 cm^3/g at 25 °C and relative pressure of 0.01. This value is lower than the CO_2 capture capacity of h-WO_3 of 3.2 cm^3/g reported recently [13], even though these nanoparticles are highly crystalline h-WO_3 according to the XRD analysis. There are two possible reasons for this result. The first is the crystal defects in h-WO_3. The FFT image in the inset of **Figure 2.6(b)** contains vertical lines, which indicates that the prepared nanoparticles have stacking faults in their crystal structure. Thus, the hexagonal channels

have not formed completely, which is because the crystal growth period (cooling process) during spray pyrolysis was quite short [11]. The second reason is the effect of the ammonium ions (NH_4^+) of ATP. Previously, Kudo's group [29] reported that h-WO_3 nanoparticles prepared from ATP have WO_6 octahedra with inclined plane geometries because of the effect of the remaining NH_4^+. If NH_4^+ are present in the crystal structure, the *c*-axis of the crystal structure could be shortened from 3.899 to 3.823 Å, and the size of hexagonal channels will shrink accordingly. This might lead to the formation of smaller hexagonal channels than in the absence of NH_4^+. Although the pore size analysis and optimization of experimental conditions to maximize CO_2 adsorption are required in the future, we succeeded in producing single-phase h-WO_3 nanoparticles with a short t_s.

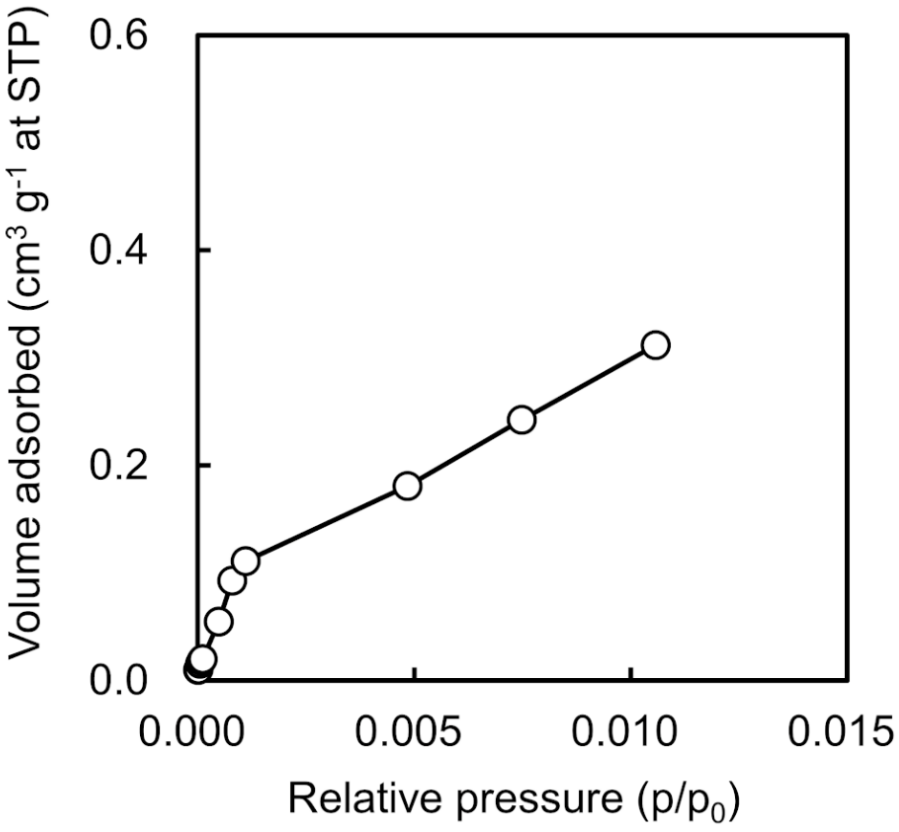

Figure 2.10 CO_2 adsorption curves of WO_3 nanoparticles prepared at a carrier gas flow rate of 1 L/min at 25 °C.

2.4. Summary

A spray pyrolysis method was developed to synthesize single-phase h-WO_3 nanoparticles/nanorods. Q_c was optimized to provide sufficient t_s for the formation of h-WO_3. Rod-like nanoparticles composed of only the h-WO_3 phase were obtained when a low Q_c of 1 L/min was used, which is equivalent to a t_s of 18.4 s. Gas adsorption analysis indicated that S_A of the nanoparticles was about 12.8 m^2/g, and less presence of hexagonal channels in the h-WO_3 nanoparticles was estimated.

2.5 References

[61] Y. T. Kwon, K. Y. Song, W. I. Lee, G. J. Choi, Y. R. Do, *Photocatalytic behavior of WO_3-loaded TiO_2 in an oxidation reaction,* Journal of Catalysis, 191(2000) 192-199.

[62] K. Bange, *Colouration of tungsten oxide films: A model for optically active coatings*, Solar Energy Materials and Solar Cells 58 (1999) 1-131.

[63] S. H. Lee, R. Deshpande, P. A. Parilla, K. M. Jones, B. To, A. H. Mahan, A. C. Dillon, *Crystalline WO_3 Nanoparticles for Highly Improved Electrochromic Applications*, Advanced Materials 18 (2006) 763-766.

[64] A. Purwanto, H. Widiyandari, T. Ogi, K. Okuyama, *Role of particle size for platinum-loaded tungsten oxide nanoparticles during dye photodegradation under solar-simulated irradiation*, Catalysis Communications 12 (2011) 525-529.

[65] H. Widiyandari, A. Purwanto, R. Balgis, T. Ogi, K. Okuyama, *CuO/WO_3 and Pt/WO_3 nanocatalysts for efficient pollutant degradation using visible light irradiation*, Chemical Engineering Journal 180 (2012) 323-329.

[66] A. B. D. Nandiyanto, O. Arutanti, T. Ogi, F. Iskandar, T. O. Kim, K. Okuyama, *Synthesis of spherical macroporous WO_3 particles and their high photocatalytic performance*, Chemical Engineering Science 101 (2013) 523-532.

[67] O. Arutanti, A. B. D. Nandiyanto, T. Ogi, F. Iskandar, T. O. Kim, K. Okuyama, *Synthesis of composite WO_3/TiO_2 nanoparticles by flame-assisted spray pyrolysis and their photocatalytic activity*, Journal of Alloys and Compounds 591 (2014) 121-126.

[68] O. Arutanti, A. B. Nandiyanto, T. Ogi, T. O. Kim, K. Okuyama, *Influences of porous structurization and Pt addition on the improvement of photocatalytic performance of WO_3 particles,* ACS Appl Mater Interfaces 7 (2015) 3009-17.

[69] O. Arutanti, A. F. Arif, R. Balgis, T. Ogi, K. Okuyama, F. Iskandar, *Tailored synthesis of macroporous Pt/WO_3 photocatalyst with nanoaggregates via flame assisted spray pyrolysis*, AIChE Journal 62 (2016) 3864-3873.

[70] T. Ogi, T. Makino, S. Nagai, W. J. Stark, F. Iskandar, K. Okuyama, *Facile and Efficient Removal of Tungsten Anions Using Lysine-Promoted Precipitation for Recycling High-Purity Tungsten*, ACS Sustainable Chemistry & Engineering 5 (2017) 3141-3147.

[71] T. Ogi, A. B. D. Nandiyanto, K. Okuyama, *Nanostructuring strategies in functional fine-particle synthesis towards resource and energy saving applications*, Advanced Powder Technology 25 (2014) 3-17.

[72] H. K. Chae, D. Y. Siberio-Pérez, J. Kim, Y. Go, M. Eddaoudi, A. J. Matzger, M. O'Keeffe, O. M. Yaghi, *A route to high surface area, porosity and inclusion of large molecules in crystals*. Nature 427 (2004) 523-527.

[73] W. Sun, M. T. Yeung, A. T. Lech, C. W. Lin, C. Lee, T. Li, X. Duan, J. Zhou, R. B. Kaner, *High Surface Area Tunnels in Hexagonal WO_3*, Nano Letters 15 (2015) 4834-8.

[74] L. Wang, J. Pfeifer, C. Balázsi, P. I. Gouma, *Synthesis and Sensing Properties to NH_3 of Hexagonal WO_3 Metastable Nanopowders*, Materials and manufacturing processes 22 (2007) 773-776.

[75] C. Balázsi, L. Wang, E. O. Zayim, I. M. Szilágyi, K. Sedlacková, J. Pfeifer, A. L. Tóth, P.-I. Gouma, *Nanosize hexagonal tungsten oxide for gas sensing applications*, Journal of the European Ceramic Society 28 (2008) 913-917.

[76] K. Huang, Q. Pan, F. Yang, S. Ni, X. Wei, D. He, *Controllable synthesis of hexagonal WO_3 nanostructures and their application in lithium batteries*, Journal of Physics D: Applied Physics 41 (2008) 155417.

[77] C. Lian, X. Xiao, Z. Chen, Y. Liu, E. Zhao, D. Wang, C. Chen, *Preparation of hexagonal ultrathin WO_3 nano-ribbons and their electrochemical performance as an anode material in lithium ion batteries*, Nano Research 9 (2015) 435-441.

[78] B. Gerand, G. Nowogrocki, J. Guenot, M. Figlarz, *Structural Study of a New Hexagonal Form of Tungsten Trioxide*, Journal of Solid State Chemistry 29 (1979) 429-434.

[79] K. H. Cheng, A. J. Jacobson and M. S. Whittingham, *Hexagonal tungsten trioxide and its intercalation chemistry*, Solid State Ionics 5 (1981) 355-358.

[80] I.M. Szilágyi, J.n. Madara´sz, G.r. Pokol, P.t. Kira´ly, G.b. Ta´rka´nyi, S. Saukko, J.n. Mizsei, A.L. To´th, A.s. Szabo´, K. Varga-Josepovits, *Stability and Controlled Composition of Hexagonal WO_3*, Chemistry of Materials 20 (2008) 4116-4125.

[81] Y. Wu, Z. Xi, G. Zhang, J. Yu, D. Guo, *Growth of hexagonal tungsten trioxide tubes*, Journal of Crystal Growth 292 (2006) 143-148.

[82] J. M. Ortega, A. I. Martínez, D. R. Acosta, C. R. Magaña, *Structural and electrochemical studies of WO_3 films deposited by pulsed spray pyrolysis,* Solar Energy Materials and Solar Cells 90 (2006) 2471-2479.

[83] O. Arutanti, T. Ogi, A. B. D. Nandiyanto, F. Iskandar, K. Okuyama, *Controllable crystallite and particle sizes of WO_3 particles prepared by a spray-pyrolysis method and their photocatalytic activity*, AIChE Journal 60 (2014) 41-49.

[84] A. Phuruangrat, D. J. Ham, S. J. Hong, S. Thongtem, J. S. Lee, *Synthesis of hexagonal WO_3 nanowires by microwave-assisted hydrothermal method and their electrocatalytic activities for hydrogen evolution reaction.* Journal of Materials Chemistry, 20 (2010) 1683-1690.

[85] K. Okuyama, I. W. Lenggoro, *Preparation of nanoparticles via spray route*, Chemical Engineering Science, 58 (2003) 537-547.

[86] T. Ogi, D. Hidayat, F. Iskandar, A. Purwanto, K. Okuyama, *Direct synthesis of highly crystalline transparent conducting oxide nanoparticles by low pressure spray pyrolysis,* Advanced Powder Technology, 20 (2009) 203-2609.

[87] W. N.Wang, A. Purwanto, I. W. Lenggoro, K. Okuyama, H. Chang, & H.D. Jang, *Investigation on the correlations between droplet and particle size distribution in ultrasonic spray pyrolysis,* Industrial & Engineering Chemistry Research, 47 (2008) 1650-1659.

[88] D. Hidayat, A. Purwanto, W. N. Wang, & K. Okuyama, *Preparation of size-controlled tungsten oxide nanoparticles and evaluation of their adsorption performance.* Materials Research Bulletin, 45 (2010) 165-173.

[89] J. Oi, A. Kichimoto, T. Kudo, *Hexagonal Tungsten Trioxide Obtained from Peroxo-polytungstate and Reversible Lithium Electro-intercalation into Its Framework*, Journal of Solid State Chemistry 96 (1992) 13-19.

*This chapter was written based on the paper published on *Advanced Powder Technology*:
S. Nakakura, A.F. Arif, F.G. Rinaldi, T. Hirano, E. Tanabe, R. Balgis, T. Ogi, Direct synthesis of highly crystalline single-phase hexagonal tungsten oxide nanorods by spray pyrolysis, Advanced Powder Technology, 30 (2019) 6-12.

Chapter 3

Cationic Defect engineering for controlling the infrared absorption of hexagonal tungsten bronze nanoparticles*

3.1 Introduction

Structural defects play an important role in regulating the properties of metal oxides. Controllably introduced defects alter the density of localized charges, which affect the charge mobility and the response to an incident electromagnetic field and other chemicals [1]. Based on this principle, structural defects have been engineered to control the electronic [2,3], optical [4], ionic transport [5], adsorption [6], and catalytic properties [7] of metal oxides.

Controlling the stoichiometry of metal oxides by creating an oxygen vacancy (V_O) has been popular in defect engineering [8]. For example, V_O can be introduced to the structure of tungsten trioxide (WO_3), which creates a suboxide WO_{3-x}. A recent study reported that this structure has a high chemical adsorption ability owing to the formation of active sites by V_Os [9]. Another study found that the electrons provided from V_Os and interstitial dopants, such as Rb^+ and Cs^+, facilitated the absorption of near-infrared (NIR) light in hexagonal tungsten bronzes [10,11,12,13].

Besides anionic defects (*i.e.,* V_O), Li *et al*. suggested that a cationic defect can also greatly influence the electrical conductivity and catalytic activity of metal oxides [14].

Similarly, Zhao *et al*. synthesized the chalcogenide copper-deficient $Cu_{2-x}S$ for optical materials [15]. In titania, the incorporation of fluorine as an interstitial dopant determines the number of titanium vacancies, which suggests a correlation between cationic defects and an interstitial dopant [14].

Among the tungsten bronzes, nanometer-sized cesium tungsten bronzes ($Cs_{0.32}WO_3$), in particular, have attracted much attention as a NIR shielding material owing to its excellent NIR absorption capability and high transmittance of visible light [10,16]. These properties are strongly correlated with the electrons in the hybridized orbitals of W 5*d* and O 2*p* in the conduction band, which are derived from V_Os and alkali dopants [17,12,13. In a recent study, Okada *et al*. [18,12] observed a coordinated linear structural change in lattice dimensions, which were interpreted as arising from the relaxation of the pseudo–Jahn–Teller (PJT) distortion by decreasing Cs defects and/or increasing V_Os in $Cs_{0.32}WO_3$. However, the effect of cationic defects, which includes W deficiency in $Cs_{0.32}WO_3$, remains a concern that should be investigated.

Based on the above background, the current study focuses on the nanoscale engineering of cationic defects in the $Cs_{0.32}WO_3$ crystal. Specifically, we focus on W deficiency and doping states of Cs ions with their effects on the NIR absorption properties. $Cs_{0.32}WO_3$ nanoparticles including cationic defects were synthesized using spray pyrolysis. This process has been proven to be effective for the synthesis of various nanostructured and heteroatom-doped particles[19-22]. It features a rapid quenching, which increases the possibility of defect formation. A control of the cationic defects is achieved by heat treatment in a mildly reducing atmosphere. Close attention is given to the spatial aspect of the crystal structure through observations of lattice constants, atomic arrangements, and interatomic distances, to construct a hypothesis for the relation between the cationic defects and the NIR absorption properties.

3.2 Experimental

3.2.1 Preparation of $Cs_{0.32}WO_3$

A solution containing ammonium para-tungstate pentahydrate (ATP; $(NH_4)_{10}(W_{12}O_{41})\cdot 5H_2O$; purity 88%–90%; Kanto Chemical Co., Inc., Tokyo, Japan), was dissolved in ultra-pure water with a concentration of 10 mmol/L, which was used as the main precursor. A solution containing cesium carbonate (Cs_2CO_3; purity 99.9% Sigma-Aldrich Co., St Louis, Mo, USA), dissolved in ultra-pure water with a concentration of 40 mmol/L, was used as the Cs precursor. The atomic ratio of Cs : W = 0.32 : 1, which is close to the typical hexagonal tungsten bronze structure. The spray pyrolysis reactor system consisted of an ultrasonic nebulizer (NE-U17; Omron Healthcare Co., Ltd., Tokyo, Japan; operated at 1.7 MHz) as a droplet generator, a tubular ceramic tube (length of 1.3 m and inner diameter of 28.5 mm) as a reactor, and a glass microfiber filter as a particle collector. The tubular furnace was arranged horizontally and divided into five temperature zones, that is, 200, 500, 700, 1200, and 1200 °C. The generated droplets were fed into the tubular furnace using air as the carrier gas with a flow rate of 5 L/min. Temperatures at the end of the furnace, that is, in the last two zones, were varied from 1000 °C to 1400 °C. Control of the W defect was achieved by a heat treatment in 5% H_2 with Ar balance at varied temperatures between 300 and 650 °C for 1 h.

3.2.2 Characterization

Size, morphology, and structure of prepared particles were characterized using scanning electron microscopy (SEM; S-5200, 5-20 kV, Hitachi High-Tech. Corp., Tokyo, Japan) and transmission electron microscopy (TEM; JEM-2010 and JEM-3000F, 200 and 297 kV, JEOL Ltd., Tokyo, Japan). Elemental mapping of prepared particles was carried out

with a post-column 90 energy filter system (GIF-2000 Gatan Inc., Pleasanton, CA, USA). The W deficiency in $Cs_{0.32}WO_3$ was investigated by spherical aberration-corrected scanning TEM (STEM; JEM-ARM-200F, 200 kV, JEOL Ltd., Tokyo, Japan). Number-averaged particle diameters were determined by direct measurements on more than 200 randomly-selected particles. The crystalline phase of $Cs_{0.32}WO_3$ particles was examined by X-ray diffraction (XRD; Bruker D2 Phaser, Bruker AXS GmbH, Karlsruhe, Germany) using Cu Kα radiation (λ = 1.54 Å), operated at30 kV and 10 mA with a scan step of 0.02 deg. Rietveld analysis was performed using Total Pattern Analysis Solutions (TOPAS version 6; Bruker AXS GmbH, Karlsruhe, Germany) software [23,24]. Weight percentages, lattice constants and site occupancy of Cs, W, and O (S_{Cs}, S_W, $S_{O(1)}$, and $S_{O(2)}$) in $Cs_{0.32}WO_3$ crystal assuming the *P6₃/mcm* were determined. In this study, the fraction of Cs, W, and O deficiency (V_{Cs}, V_W, $V_{O(1)}$, and $V_{O(2)}$) were calculated based on the value of S_{Cs}, S_W, $S_{O(1)}$, and $S_{O(2)}$. The oxidation states of W and Cs were examined using X-ray photoelectron spectroscopy (XPS; ESCA-3400, Shimadzu, Kyoto, Japan) operated at 10 kV and 20 mA. Uncleaned powders were used considering that the surface of samples is reduced by the irradiation of Ar^+ beam. Energy dependence was calibrated using C1*s* spectrum. Shirley type baseline was applied. The mean distance between W and O atoms was determined by using X-ray Adsorption Fine Structure (XAFS; BL5S1, Aichi Synchrotron Radiation Center, Seto, Japan). To investigate the optical performance, $Cs_{0.32}WO_3$ nanoparticles were dispersed in methyl isobutyl ketone at a concentration of 0.02 wt%. Optical measurements were conducted using a UV-Vis-NIR spectrophotometer (Model V-670, JASCO Corporation, Tokyo, Japan).

3.3 Results and Discussion

3.3.1 Synthesis and Characterization of $Cs_{0.32}WO_3$ Nanoparticles

$Cs_{0.32}WO_3$ particles were synthesized using spray pyrolysis at various temperatures that were determined in course of the preliminary experiments. The temperatures in the earlier zones of the furnace are designed to promote self-assembly of the precursor in the droplets and solvent evaporation. The critical zone where the precursor is converted into a particle is usually at the end of the furnace. Specifically, in the production of metals and metal oxides, the temperature of the end zone of the furnace determines the crystal structure of the final particle. On the basis of this background, the temperature of the last two zones of the furnace in this research was varied to evaluate its effect on the crystal structure. The temperature of these zones was then referred to as the synthesis temperature. Samples synthesized at 1200 °C were selected for further investigation because of the small particle size (~50 nm) and the relatively narrow size distribution, as shown in **Figure 3.1(c)**. The other samples exhibited an inhomogeneous size distribution with the observance of some large particles (**Figures 3.1**).

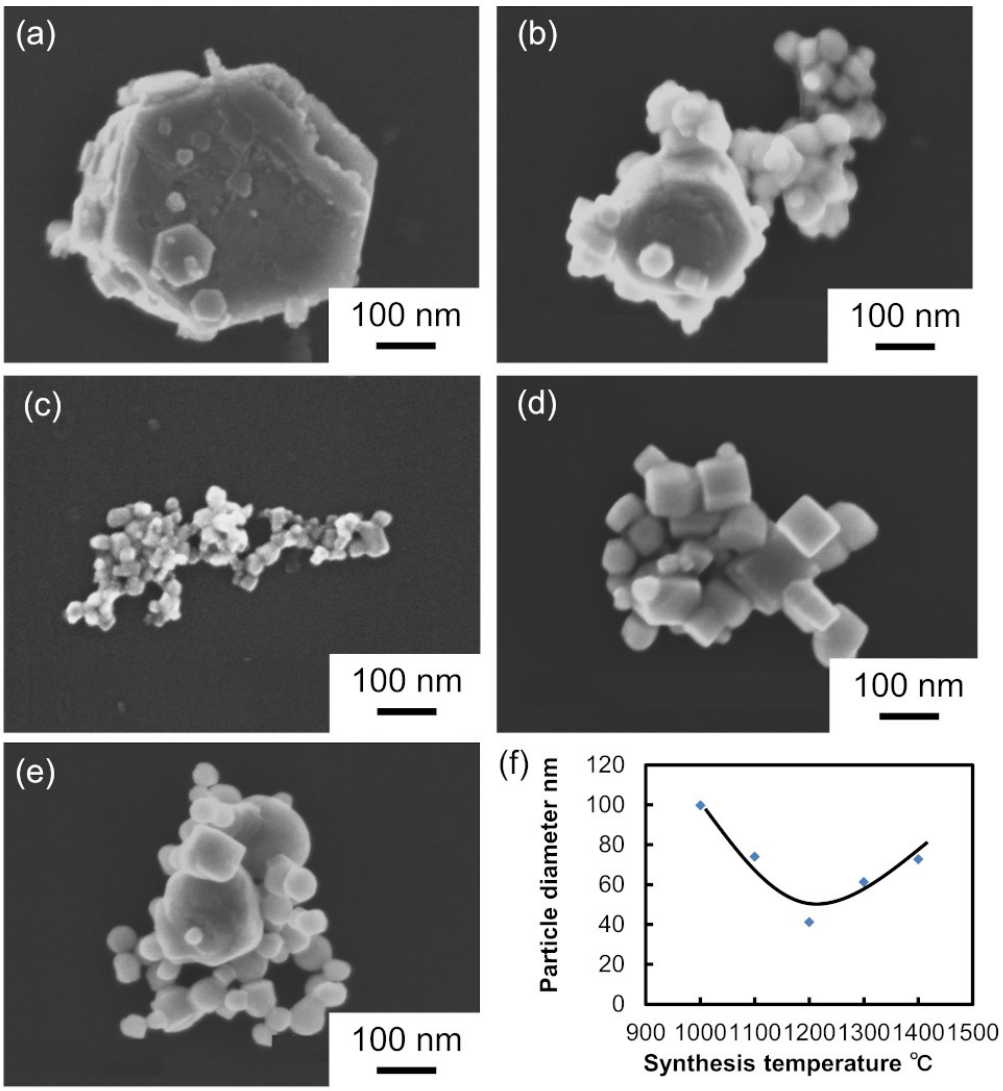

Figure 3.1 SEM images of particles prepared at (a) 1000 °C, (b) 1100 °C, (c) 1200 °C, (d) 1300 °C, and (e) 1400 °C, and (f) the temperature dependence of particle diameter.

The XRD spectrum of particles prepared at 1200 °C in **Figure 3.2** exhibits a mixed pattern of $Cs_{0.32}WO_3$ (ICDD No.04-009-6455), $(Cs_2O)_{0.44}W_2O_6$ (ICDD No.00-47-0566), $W_{11}O_{22}$(ICDD No.04-007-0719), $(H_2O)_{0.33}WO_3$ (ICDD No.01-072-0199), ATP (ICDD No.00-040-1470), and WO_2 (ICDD No.00-032-1393). The formation of $(Cs_2O)_{0.44}W_2O_6$ and $(H_2O)_{0.33}WO_3$ phases was realized by the presence of oxygen in the carrier gas (air) and water in the precursor solution. The formation of $(Cs_2O)_{0.44}W_2O_6$ phase implied

insufficient Cs doping in the $Cs_{0.32}WO_3$ particles.

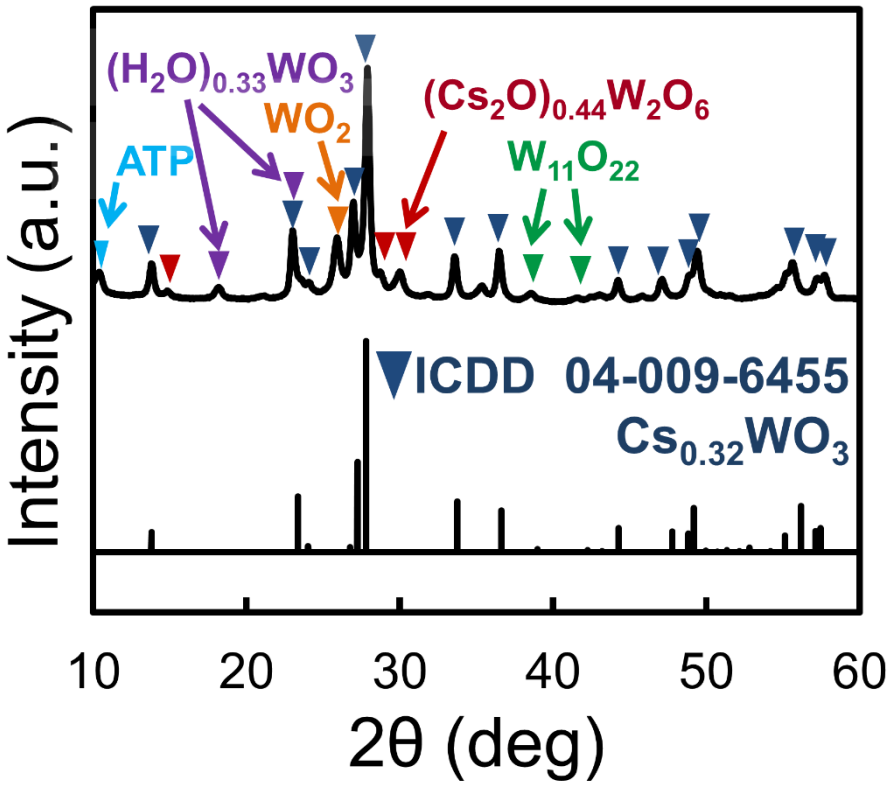

Figure 3.2 XRD spectrum of particles prepared at 1200 °C.

Figures 3.3(a) show the STEM image of the obtained particle and the corresponding elemental mappings of Cs, W, and O atoms are indicated in **Figures 3.3(b)**, **(c)**, and **(d)**, respectively. Cs atoms are uniformly distributed even in the small particles with a diameter of 10 nm.

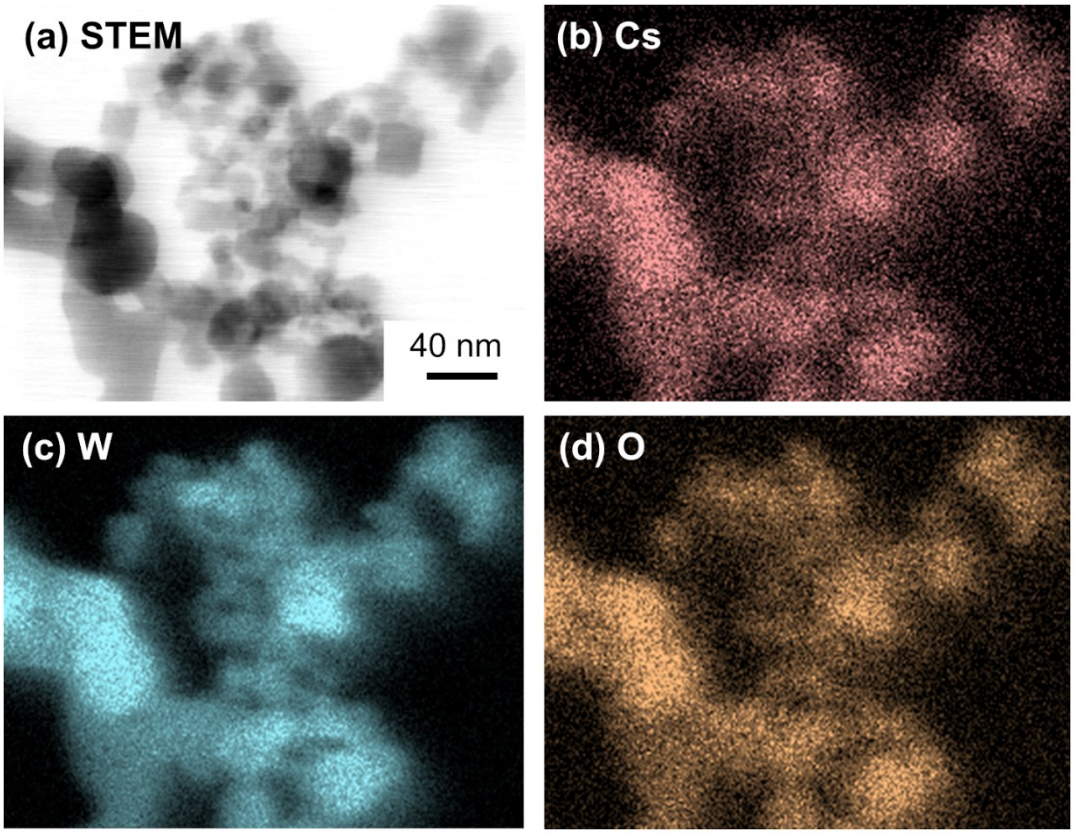

Figure 3.3 STEM image and elemental mapping of Cs, W, and O atoms.

Figure 3.4 shows the optical properties of the dispersed $Cs_{0.32}WO_3$ nanoparticles. According to previous reports [10,16], NIR absorption property is expected if the prepared nanoparticles have a hexagonal $Cs_{0.32}WO_3$ crystalline phase. However, NIR absorption properties were not observed in the present as-prepared samples even though a hexagonal structure was confirmed. Immaturity of the crystals and high oxidation states (+6) of tungsten were suggested as possibly causing the absence of NIR absorption. Therefore, the as-prepared sample was heat treated under a mildly reducing environment to rearrange the crystal structure. In attempt to control the oxidation states in the crystal structure, three different temperatures, namely, 300, 450, and 650 °C, were used for the heat treatment.

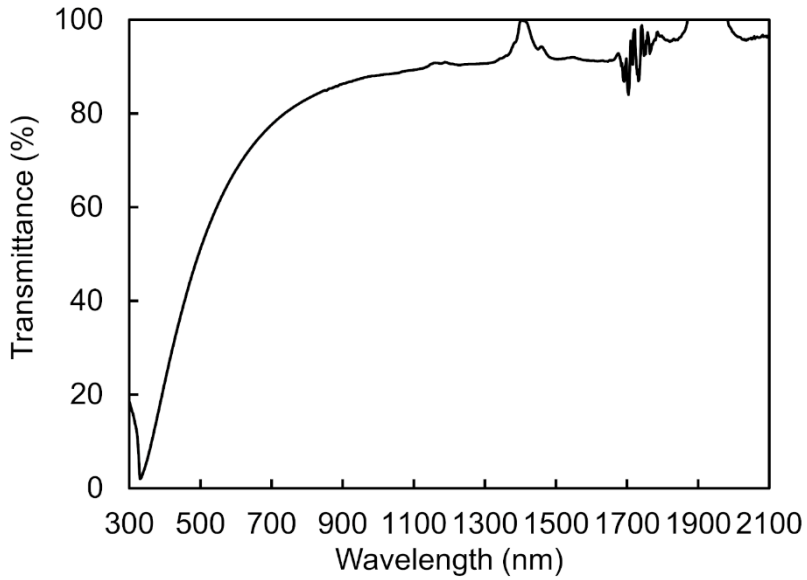

Figure 3.4 Transmittance profile of $Cs_{0.32}WO_3$ nanoparticles prepared by spray pyrolysis at 1200 °C.

Figure 3.5 shows the decreasing of the $(Cs_2O)_{0.44}W_2O_6$, WO_2, $(H_2O)_{0.33}WO_3$, and ATP peaks with increasing temperature of the heat treatment. These peaks disappeared when a temperature of 650 °C was applied except for $W_{11}O_{22}$. A quantitative Rietveld analysis was conducted until the index of *R*-weighted pattern (R_{wp}) fell below 10 for a reliable refinement. Interestingly, the fraction of $Cs_{0.32}WO_3$ increased in parallel with the diminution of $(Cs_2O)_{0.44}W_2O_6$, WO_2, $(H_2O)_{0.33}WO_3$, and ATP phases, as shown in **Figure 3.6(a)**. This suggests that the heat treatment in a mildly reducing environment decomposed $(Cs_2O)_{0.44}W_2O_6$ and $(H_2O)_{0.33}WO_3$, and then, urged crystallization of $Cs_{0.32}WO_3$ through the following reaction.

$$0.75\ (H_2O)_{0.33}WO_3+(Cs_2O)_{0.44}W_2O_6+0.19\ H_2 \rightarrow 2.75\ Cs_{0.32}WO_3+0.69\ H_2O \quad (1)$$

Along with the growth of $Cs_{0.32}WO_3$, the particle color changed from light green to blue, as shown in **Figure 3.6(b)**. The heat treatment kept the particle size below 100 nm, as shown in the TEM image (**Figure 3.7**). The high resolution TEM image in **Figure**

3.7(b) showed lattices with a spacing of 3.2 Å, which corresponded to the (200) plane in $Cs_{0.32}WO_3$ (ICDD 04-009-6455).

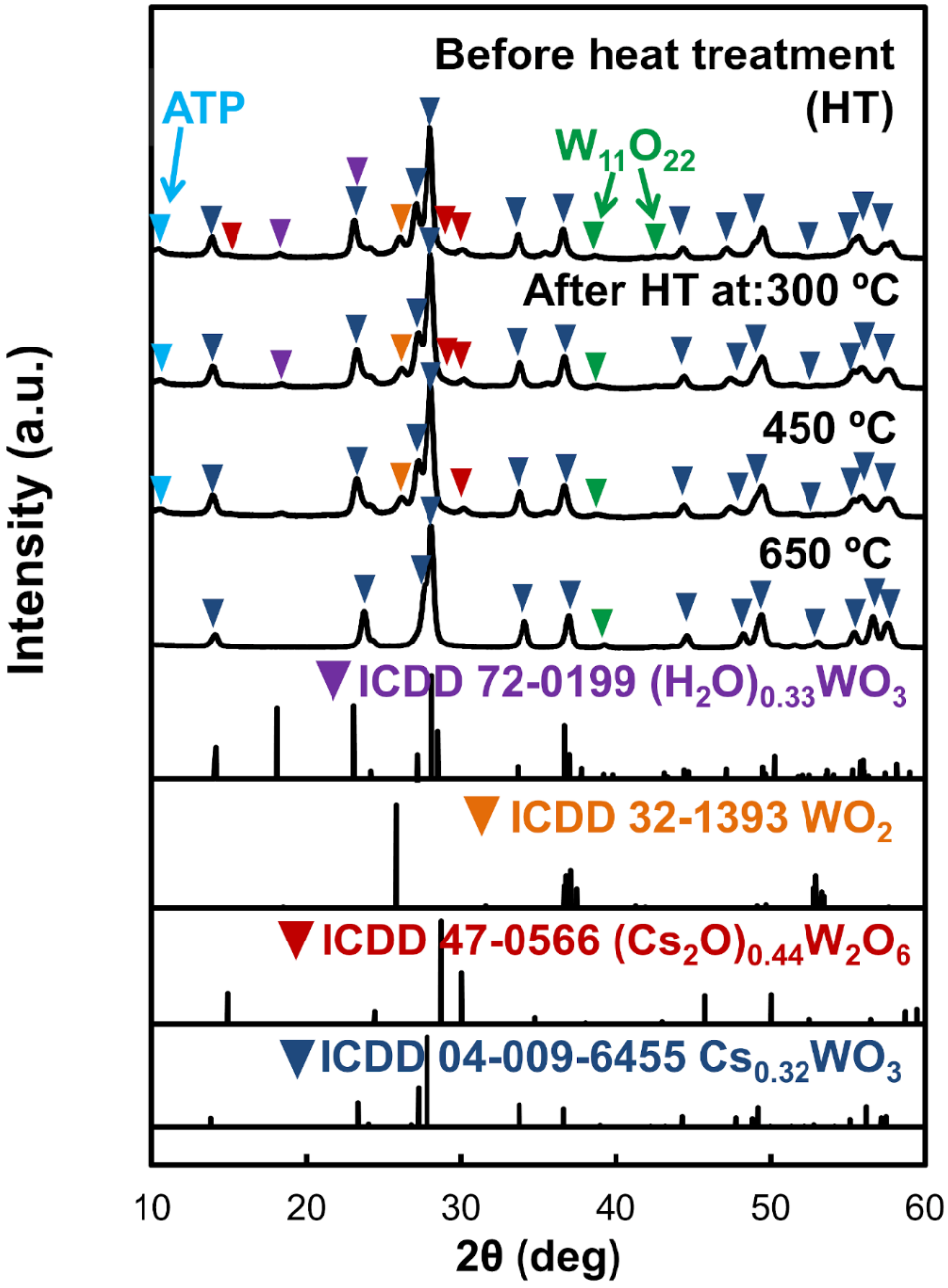

Figure 3.5 XRD patterns of samples before and after heat treatment at 300, 450, and 650 °C in 5% H_2/Ar atmosphere.

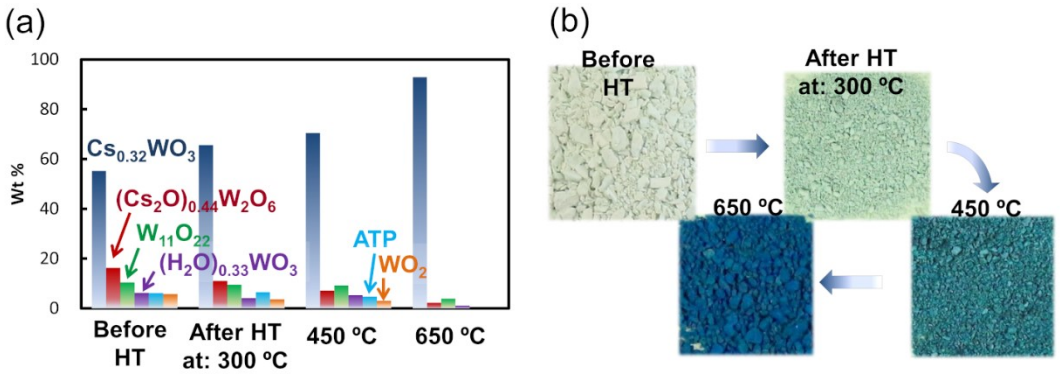

Figure 3.6 (a) Mass fractions of $Cs_{0.32}WO_3$, $(Cs_2O)_{0.44}W_2O_6$, $W_{11}O_{22}$, $(H_2O)_{0.33}WO_3$, WO_2, and ATP from Rietveld analysis, (b) optical micrographs of the sample powders before and after heat treatment.

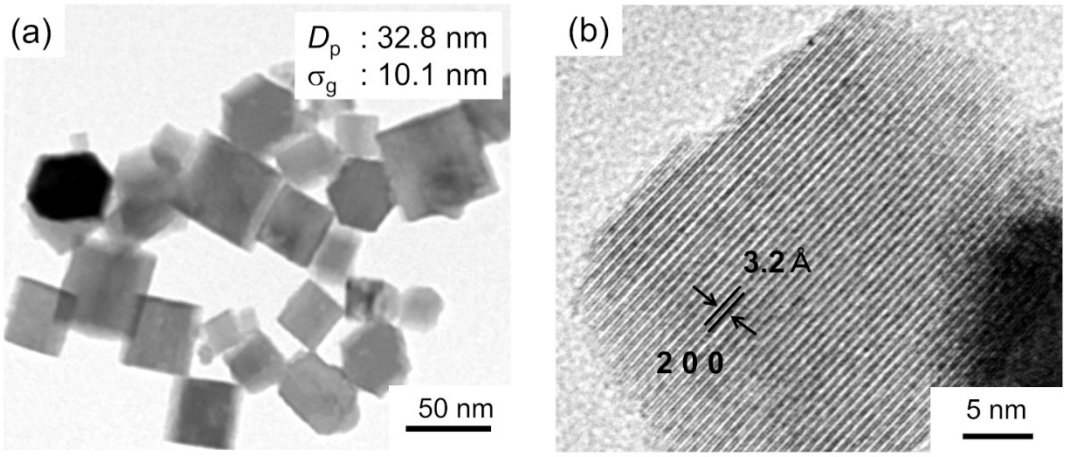

Figure 3.7 (a) TEM and (b) HRTEM images of particles after heat treatment at 650 °C.

The arrangements of W and Cs atoms before and after the heat treatment were analyzed using a high-resolution STEM in the high-angle annular dark field (HAADF) mode. **Figure 3.8(a)** notably shows a presence of linear defects aligned in the [100], [010], and [110] directions in the as-synthesized sample. The white squared area in **Figure 3.8(a)**

is magnified in **Figure 3.8(b)**. Because the brightness of the spot contrast of atoms is proportional to the atomic number in the HAADF mode, the brightest spots represent W atoms, while the less bright spots represent Cs atoms. Viewing along [001], a plane consisting of Cs and W atoms (Cs/W planes) and a plane consisting of only W atoms (W/W planes) are alternately arranged, as illustrated in **Figure 3.8(c)**. Linear defects were observed exclusively in the Cs/W plane, aligned in directions indicated by the white arrows, whereas no defects were observed in the W/W plane. The intensities of the atom spots scanned along the defect line between a and b are shown in **Figure 3.8(d)**. In the defect region, W atom rows clearly exhibited low intensities that were comparable to those of Cs atoms. This indicates that W is partly deficient in the Cs/W plane in the as-synthesized $Cs_{0.32}WO_3$. The linear W deficiency along the Cs/W plane was also observed along the [010] viewing direction (**Figure 3.9(a)**). Therefore, it was implied that the deficiency extended onto the prism planes, forming a planar deficiency. The intensity of Cs atoms shown in **Figure 3.8(d)** was predominantly stable, suggesting a uniform distribution of Cs atoms.

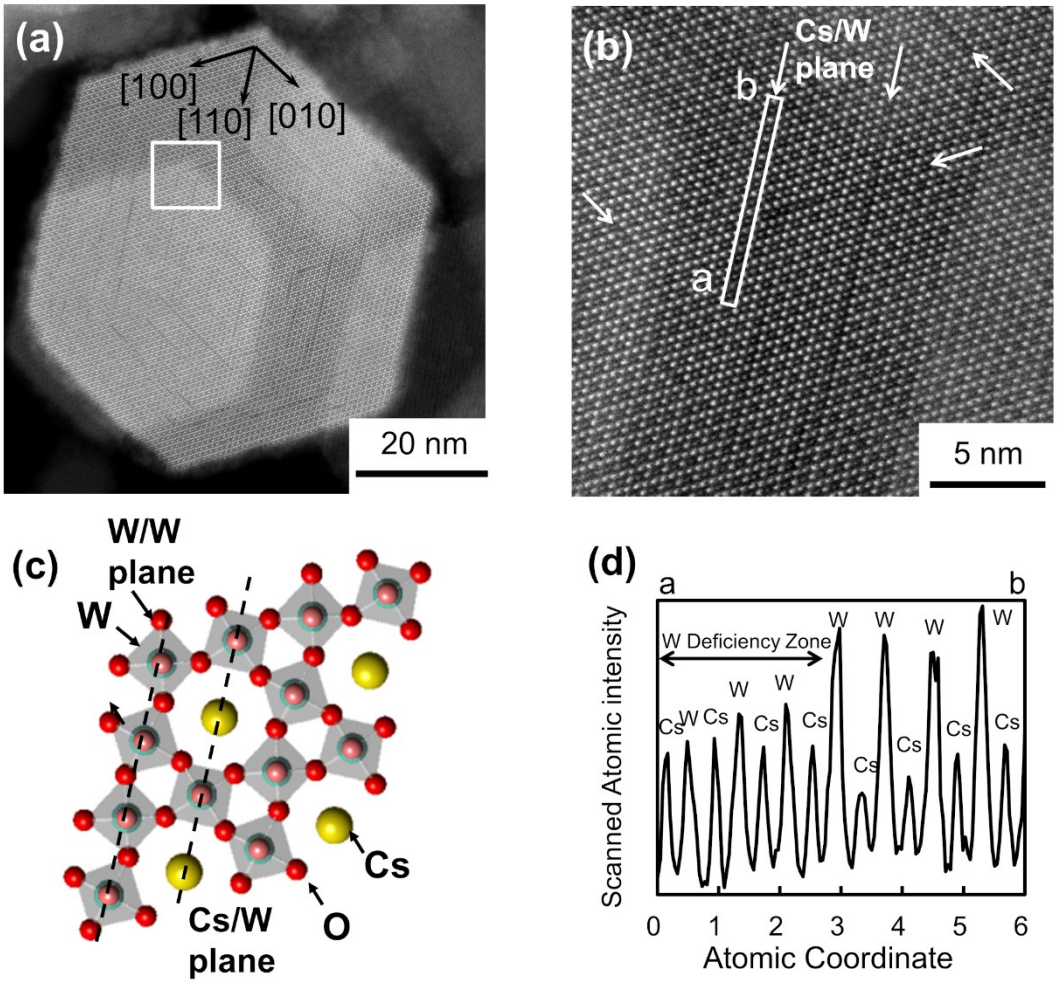

Figure 3.8 (a,b) STEM images in the HAADF mode, (c) illustrates the schematic atomic arrangements and (d) scanned spot intensity profiles along a–b in **Figure 3.8(b)**.

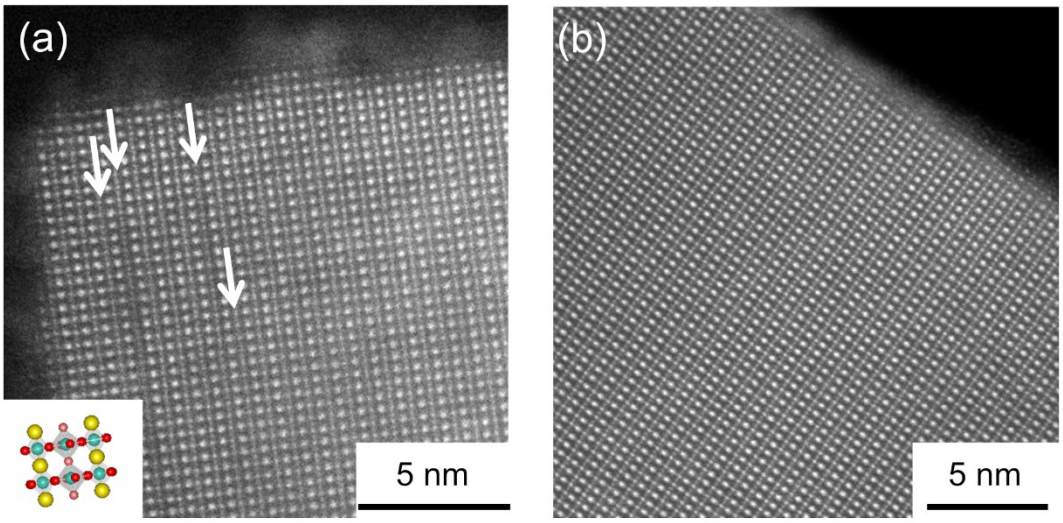

Figure 3.9 (a,b) HAADF-STEM images of the samples (a) before and (b) after heat treatment at 650 °C in 5% H_2/Ar atmosphere along the [010] viewing. Inset of (a) illustrates the atomic arrangement of the structure from the [010] direction.

The STEM–HAADF images of the heat-treated particles in **Figure 3.9(b)** and **Figures 3.10** show well-structured arrays of atoms with no appreciable W deficiencies. The faultless atomic arrays were also confirmed by the stable scanned intensity of W and Cs spots, as shown in **Figure 3.10(c)**.

Site occupancies of Cs, W, and O as analyzed by the Rietveld analysis are shown in **Table 3.1** with deduced chemical formula for sampes before and after the heat treatment. From the values of S_W (= 78.6 %) and S_{Cs} (= 60.7 %), the fraction of W planar deficiency and insufficient Cs doping for the as-synthesized sample were assessed to be 21.4 % and 39.3 %, respectively. The S_W increased gradually from 78.6 % to 100 % with increasing temperature of heat treatment, indicating that a rearrangement of W atoms took place vigorously during the heat treatment. In contrast, S_{Cs} changed moderately from 60.7 % to 77.9 %, so that the insufficient Cs doping still remained after the heat treatment. The distribution of Cs vacancies is fairly random according to **Figure 3.8(d)**. The presence of

$V_{O(1)}$ is supposed to be related to the V_W, whereas the $V_{O(2)}$ in the annealed sample are obviously introduced to O(2) site due to the reducing heat treatment.

Table 3.1 Site occupancy and chemical formula in samples before and after heat treatment. Numbers in parentheses are uncertainties in the last digit.

	Site occupancy				**Chemical**
	S_{Cs}	S_W	$S_{O(1)}$	$S_{O(2)}$	**formula**
Before heat treatment (As-synthesized)	0.607(6)	0.786(3)	0.358(17)	1.00(2)	$Cs_{0.200}W_{0.786}O_{2.716}$
After heat treatment at 300 °C	0.619(3)	0.8444(17)	0.348(11)	1.000(14)	$Cs_{0.204}W_{0.844}O_{2.696}$
After heat treatment at 450 °C	0.635(3)	0.8737(18)	0.370(12)	1.000(14)	$Cs_{0.210}W_{0.874}O_{2.740}$
After heat treatment at 650 °C	0.779(4)	1.0000(12)	0.380(11)	0.935(14)	$Cs_{0.257}W_{1.000}O_{2.630}$

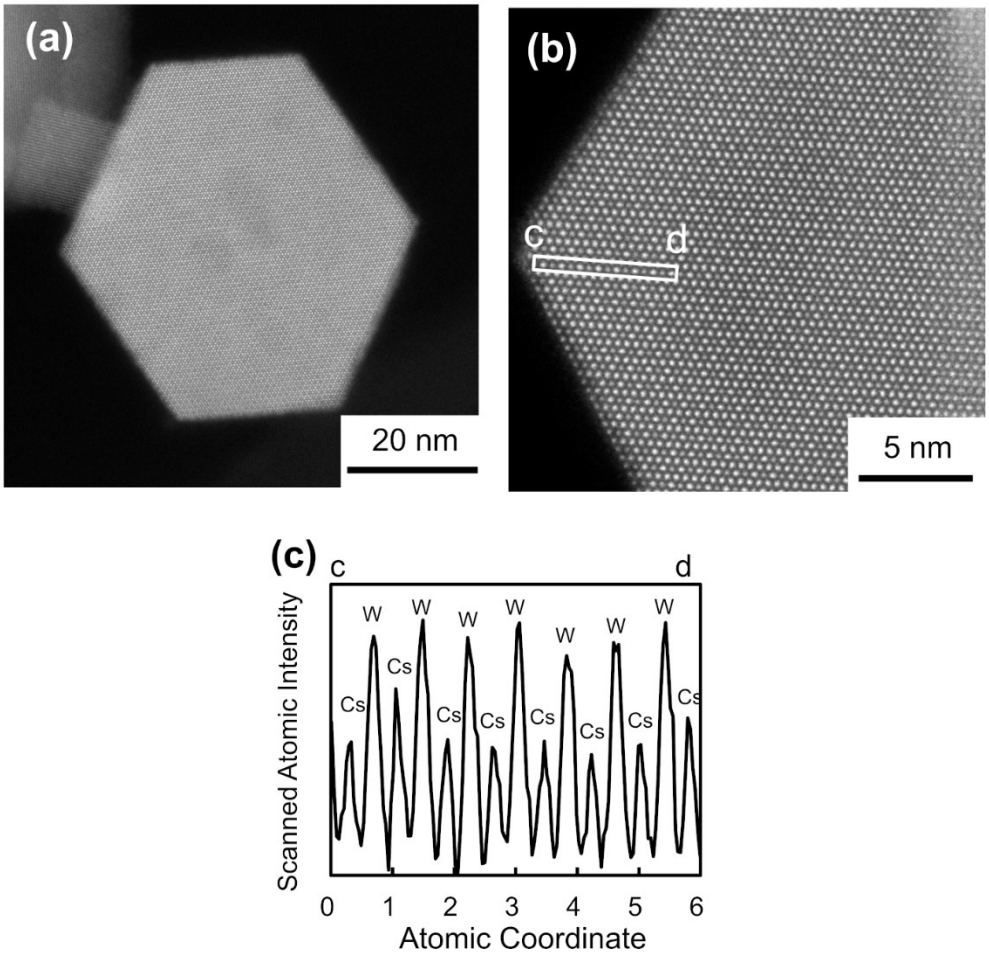

Figure 3.10 (a–b) STEM images in the HAADF mode and (c) scanned spot intensity profiles along a–b and c–d, respectively, in samples after the heat treatment at 650 °C in 5% H_2/Ar atmosphere.

In the as-synthesized sample, charge must be balanced to compensate for the observed W deficiency. Thus, to see the valence state of cations, XPS spectra of W 4*f* and Cs 3*d* were measured**.** As shown in **Figure 3.11(a)**, the W 4*f* spectrum of samples before the heat treatment showed only W^{6+} peaks at 35.5 eV ($4f_{7/2}$) and 37.6 eV ($4f_{5/2}$). All the W atoms bond O atoms with a valency of +6 in the WO_6 octahedra. The Cs 3*d* spectrum of samples before the heat treatment (**Figure 3.11(b)**) showed a peak at 723.9 eV, which

corresponds to the monovalent oxidation state. Thus, the lack of charge in the W-defected sample is considered to be compensated by the formation of $(Cs_2O)_{0.44}W_2O_6$, as evidenced by XRD in **Figure 3.2**, and the possible incorporation of H at the time of spray pyrolysis.

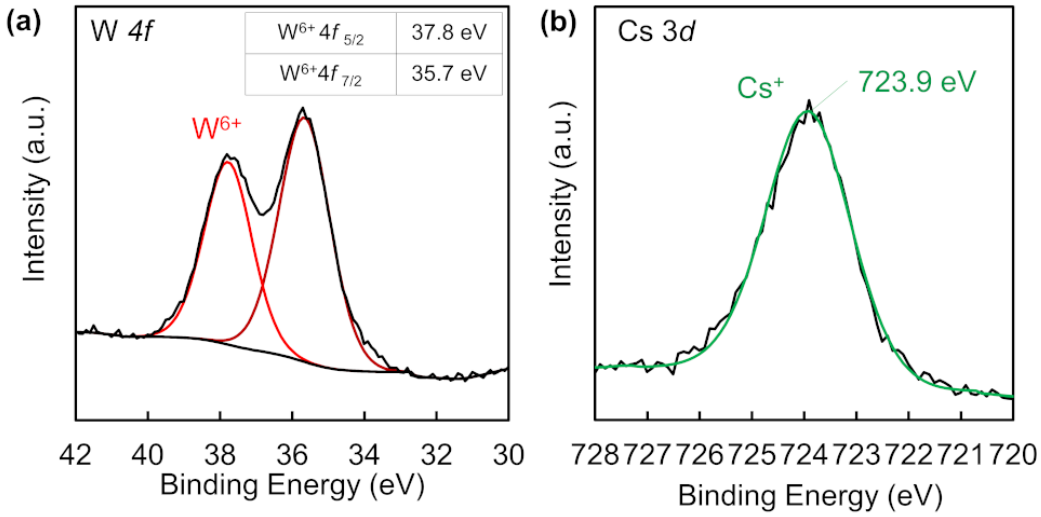

Figure 3.11 XPS spectrum of (a) W 4*f* and (b) Cs 3*d* before heat treatment in 5% H_2/Ar at 650 °C.

The reduction heat treatment brought a new peak at 33.8 eV which corresponds to W^{5+} for a 7/2 spin orbital as shown in **Figure 3.12(a)**. The low-intensity $W^{5+}4f_{5/2}$ interfered with the $W^{6+}4f_{7/2}$ at 35.5 eV. Peak deconvolution determined the area ratio of $W^{5+}/(W^{6+}+W^{5+})$ to be 26.9%. Cs 3*d* showed the same monovalent peak at 724.0 eV as shown in **Figure 3.12(b)**. These observations are in agreement with the recent series of reports on Cs_xWO_{3-y} fabricated by solid state reaction method[18,26]. On increasing reduction time during crystallization, the amount of V_O and the XPS W^{5+}/W^{6+} ratio increased according to Okada *et al.*[18] Machida *et al.* [25] analyzed the optical absorption of Cs_xWO_{3-y} nanoparticles using the Drude–Lorentz theory and the Mie scattering integration method to observe that the V_Os initiated and increased the polaron

absorption in the NIR absorption band. Yoshio *et al.*[12,13] calculated using the DFT+U method to show that the V_O-derived electrons are localized in W–5d_{xy} and W–5$d_{x^2-y^2}$ orbitals to be excited to generate a polaron absorption.

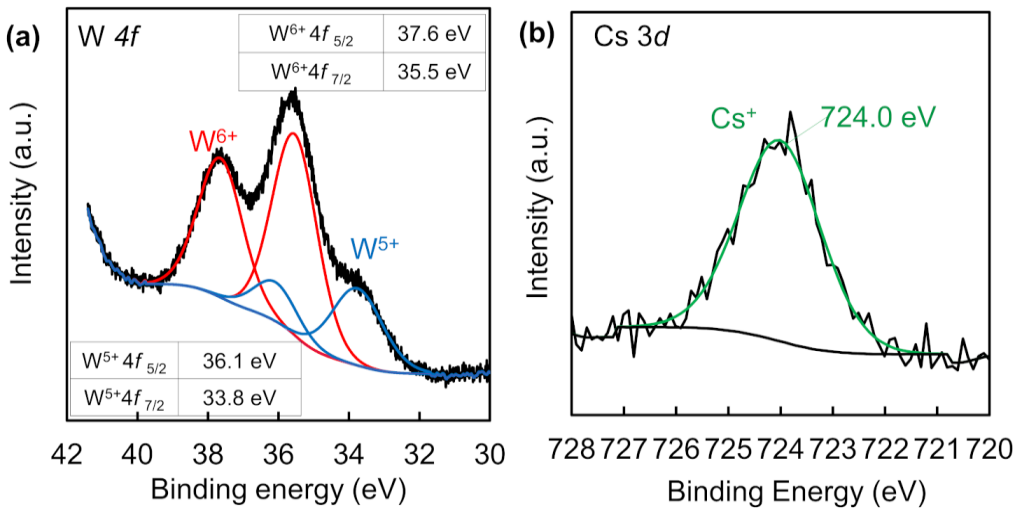

Figure 3.12 XPS spectrum of (a) W 4*f* and (b) Cs 3*d* after heat treatment in 5% H_2/Ar at 650 °C.

As summarized in **Table 3.1**, the as-synthesized sample of $Cs_{0.200}W_{0.786}O_{2.716}$ including the W planer deficiencies and insufficient Cs doping recovered the W stoichiometry through atomic rearrangements upon reduction heating, but left many Cs deficiencies toward the composition of $Cs_{0.257}W_{1.000}O_{2.630}$ after 1 hour at 650 °C. Decompositions of $(Cs_2O)_{0.44}W_2O_6$ and $(H_2O)_{0.33}WO_3$ occurred in parallel as seen above with the evaporations of H_2O.

Lattice constants of the $Cs_{032}WO_3$ phase before and after the heat treatment are plotted in **Figure 3.13**. Those of the as-synthesized sample were measured as 7.3756(5) and 7.7147(8) Å for the *a*-axis and *c*-axis, respectively. They are deviated from 7.4049(1) and 7.6098(1) Å, respectively[26], for $Cs_{030}WO_3$ synthesized by solid state reaction methods

(ICDD 81-1244). After the heat treatment, the lattice expanded along the *a*-axis and shrank along the *c*-axis, in the direction towards the reference values[26].

In alkali-doped tungsten bronzes[27,28], lattice constants are reported to increase with increasing amount of alkali dopant. According to Hussain *et al*.[29], the values of *a* and *c*–axes in the hexagonal tungsten bronzes, M_xWO_3 (M= Rb and Cs), decrease and increase, respectively, with increasing amount of the alkali ions. For reduced hexagonal Cs_xWO_{3-y}, the recent study by Okada *et al*[18]. shows that the *a*–axis shrinks and *c*–axis elongates with increasing Cs and/or V_O content in the composition range $0.20 \leq x \leq 0.32$ and $0 < y \leq 0.46$. The dimensional change occurs due to Cs- and V_O-derived electrons injected to W−5*d* orbitals causing a destabilization of the pseudo–Jahn–Teller distortion, and its effect on the dimensional change is greater than the ionic size effect[18]. In our study, the *a*–axis elongated with increasing Cs content and decreasing W deficiencies. Thus the direction of the *a*–axis modification is opposite to Hussain *et al*[30]. and Okada *et al*[18]. The magnitude of the present *a*–axis elongation is significantly larger than that in Okada *et al.* since the greater elongation increment (0.042 Å) occurred in a much narrower composition range, $0.200 \leq x \leq 0.257$ and $0.260 < y \leq 0.370$ in the present study, as compared with the smaller increment (0.012 Å) occurred in a much broader range $0.20 \leq x \leq 0.32$ and $0 < y \leq 0.46$ in Okada *et al*[18]. Thus, the present elongation in the *a*-axis is considered to be dominantly caused by the rearrangement of W atoms. The filling of W atoms to the vacant sites in the linear and/or planar W defects is supposed to be highly effective to dominate the dimensional change of lattice. Each of these W atoms shared one O atom with another W atom, causing the O–W–O bond to stretch along the *a*-axis. At the same time, the O–W–O bond in the *c*-axis direction contracted to maintain the equilibrium.

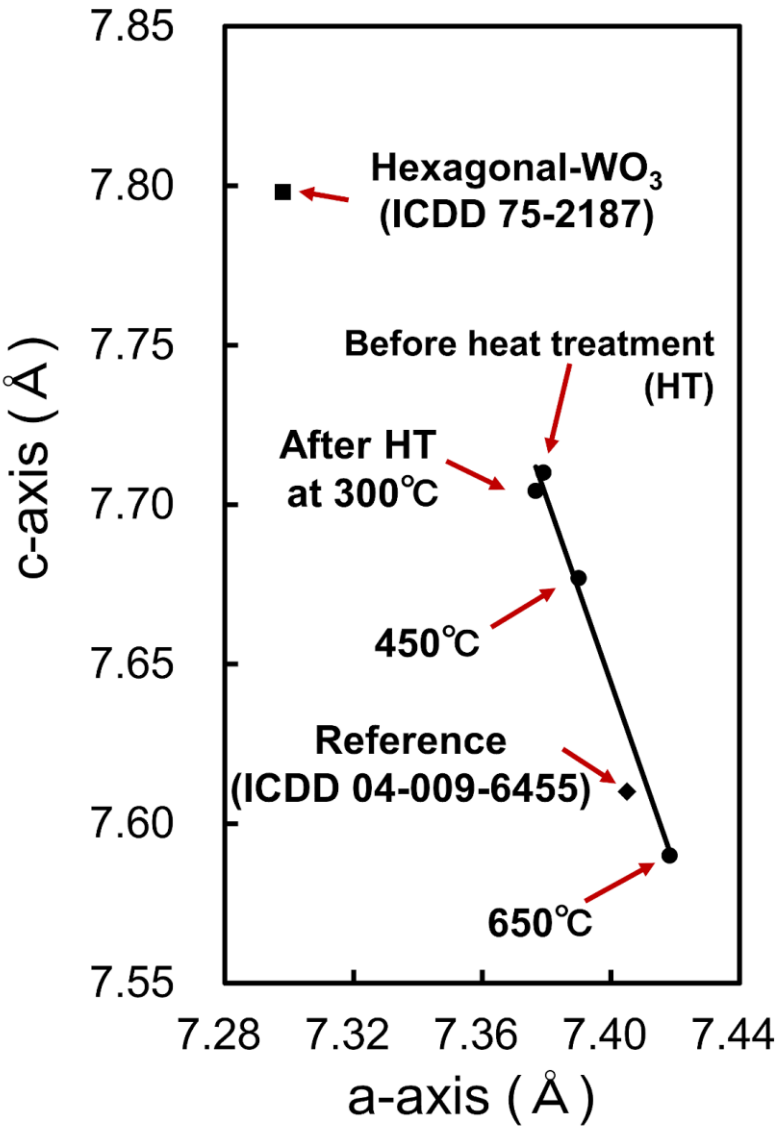

Figure 3.13 Lattice constants of $Cs_{0.32}WO_3$ particles before and after the heat treatment at various temperatures referenced with hexagonal WO_3 (ICDD No. 75-2187) and $Cs_{0.32}WO_3$ (ICDD No. 04-009-6455).

This dimensional change was consistent with the change in the W-L_3 edge XAFS spectra shown in **Figure 3.14**. The heat treatment shifted the peak in the spectrum from 1.35 Å to 1.41 Å, which indicated an increase in the average nearest-neighbor W–O distance. This was contributed by more W–O bonds in the *a*- and *b*-axis directions than

in the *c*-axis direction. Hypothetical atomic arrangements before and after the heat treatment are illustrated in **Figures 3.15(a) and (b)**, respectively. These results infer that the W planar deficiencies in $Cs_{0.32}WO_3$ should be playing a critical role in controlling the lattice constants over the wide range, 7.3756(5) Å ≤ *a* ≤ 7.4180(4) Å.

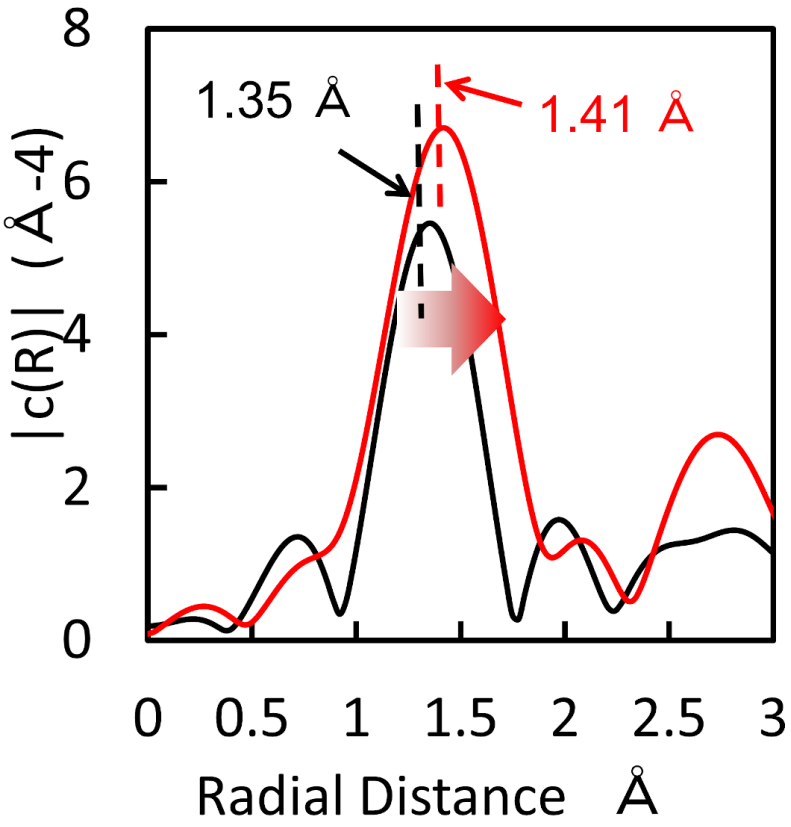

Figure 3.14 XAFS spectra showing the frequency of radial distance between W atom and the nearest neighbor atom.

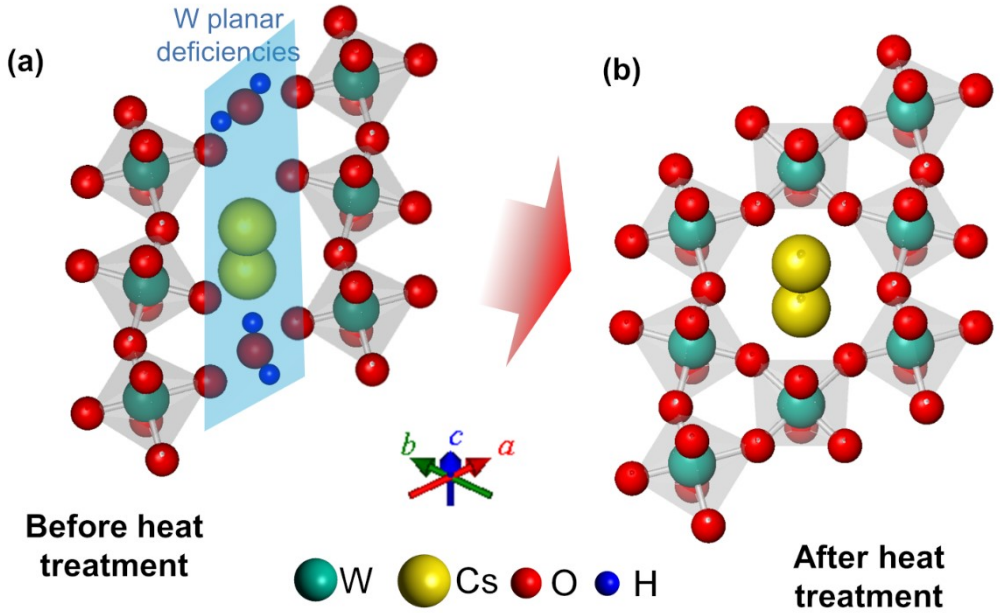

Figure 3.15 Illustrations of atomic arrangements

(a) before and (b) after the heat treatment.

3.3.2 NIR absorption Capability

By modifying the W deficiencies, the NIR absorption capability of the $Cs_{0.32}WO_3$ particles could be altered. The as-prepared $Cs_{0.32}WO_3$ particles exhibited no symptom of NIR absorption, as shown by the gray spectrum in **Figure 3.16.** The absence of NIR absorption was common with samples prepared by different synthesis temperatures. The reductive heat treatment applied on the as-prepared samples progressively developed the absorption in the infrared region.

According to the previous work [10,13], the NIR absorption property is caused by free and localized electrons in the W 5*d* orbital, which are donated from Cs and V_Os. The V_Os provide localized electrons through W^{5+}. Based on this principle, the possible reasons for the absence of NIR absorption in the present as-prepared samples could be attributed to either or all of the following 3 factors: i) insufficient Cs doping, ii) high oxidation state

of W^{6+}, and iii) presence of the linear/planar W defects.

As for the factor i), the chemical formula, $Cs_{0.200}W_{0.786}O_{2.716}$, as deduced from the site occupancies of Cs, W, and O for the synthesis temperature 1200 °C indicates the amount of 5.40 at% Cs in crystal. As well, the specimens of chemical formulae, $Cs_{0.159}W_{0.703}O_{2.566}$ and $Cs_{0.160}W_{0.680}O_{2.534}$, respectively, for the synthesis temperatures of 1000 and 1100 °C hold the amounts of 4.65 and 4.74 at% Cs in crystal. These quantities of Cs in crystal should provide a sufficient number of electrons, because the previous report[30] by Hussain *et al*. observed typical Drude-type free electron reflections in Cs_xWO_3 hexagonal tungsten bronzes with nominal Cs/W as low as 0.2, that corresponding to 4.76 at% Cs. Another recent report by Machida *et al*[25]. indicates that a strong NIR absorption occurred for a series of samples with Cs content as low as 5.06 at%. However, NIR absorption was not exhibited (**Figure 3.4** and **Figure 3.16**). Therefore, the present samples have an adequate quantity of Cs and hence the factor i) was excluded.

The factor ii) contributes to the absence of NIR absorption because the maximum valency of W was confirmed by XPS as shown in **Figure 3.11(a)**. We do not expect any W^{5+} or polaronic absorptions taking place in the as-synthesized samples, nor expect the W^{6+} in crystal invalidating electrons from Cs.

Thus, we consider that the factor iii) should be responsible for the absence of NIR absorption. It was considered that the generation of the linear/planar W defect suspended a sufficient number of electrons to be donated to the W 5*d* orbitals to activate the NIR absorption. Therefore, the state of the W deficiency was found as one of the key conditions to obtain the high NIR absorption properties.

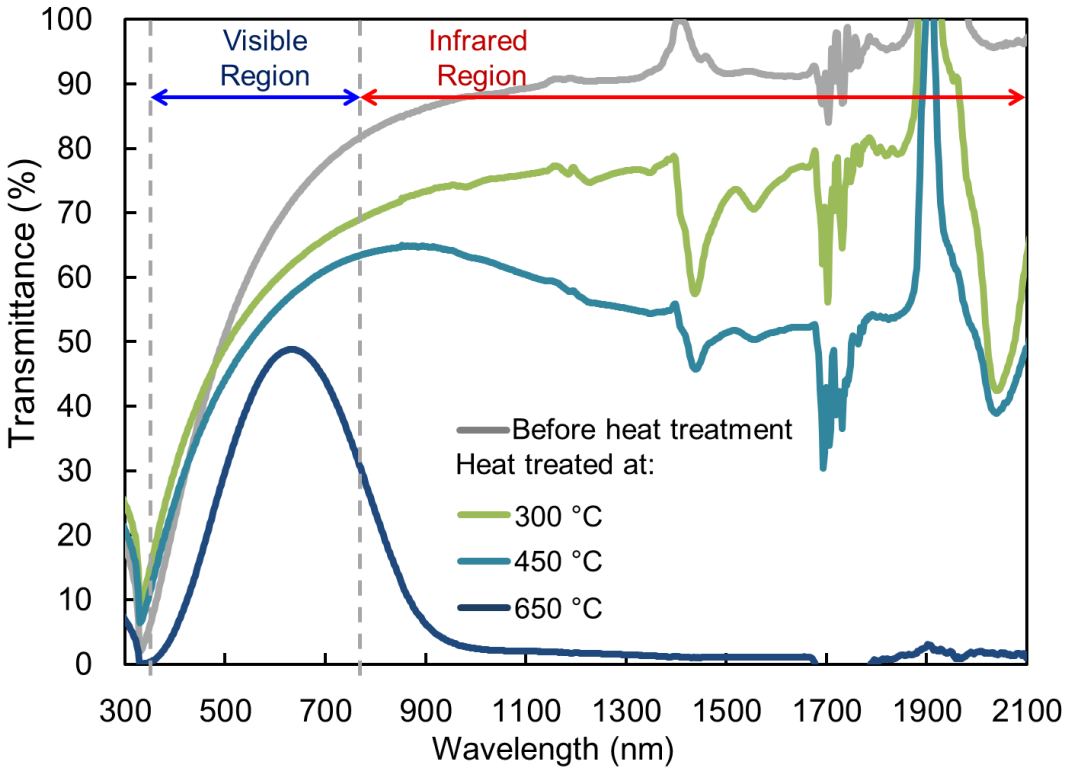

Figure 3.16 Transmittance spectra of $Cs_{0.32}$ WO_3 nanoparticles. Disturbances at 1450, 1730, and 1900 nm are caused by methyl isobutyl ketone.

These results demonstrate the possibility to control the NIR absorption of $Cs_{0.32}WO_3$ through cationic defect engineering. Our facile method proposed in this paper can control the W linear/planar deficiencies and lattice constants of $Cs_{0.32}WO_3$ nanoparticles. The consistent interrelationships between the NIR absorption, W linear/planar deficiencies and the dimensional changes of lattice emphasize the importance of considering the

cationic defects in the control of the optical properties of $Cs_{0.32}WO_3$ through crystallographic design.

3.4 Summary

In this paper, the influence of cationic defects, specifically, W deficiency and insufficient Cs doping in $Cs_{0.32}WO_3$ nanoparticles, on lattice constants and the NIR absorption properties were reported. The results showed that the W linear/planar deficiency in $Cs_{0.32}WO_3$ could be controlled by spray pyrolysis combined with heat treatments. We demonstrated that spray pyrolysis-prepared $Cs_{0.32}WO_3$ particles offered no NIR absorption that could be restored by the successive heat treatment. The main reason for the absence of NIR absorption is considered to arise from the linear/planar W defect causing the shortage of W 5*d* electrons. Thus, W deficiencies are shown as one of the key factors among the cationic defects for obtaining high NIR absorption properties. Results of this study are expected to provide an understanding on defect engineering of $Cs_{0.32}WO_3$ from the viewpoint of cationic defects. This will be beneficial for the further advancement of this material.

3.5 References

[1] H. Nan, Z. Wang, W. Wang, Z. Liang, Y. Lu, Q. Chen, D. He, P. Tan, F. Miao, X. Wang, *Strong photoluminescence enhancement of MoS_2 through defect engineering and oxygen bonding*, 8 (2014) 5738-5745.

[2] A.F. Arif, R. Balgis, T. Ogi, F. Iskandar, A. Kinoshita, K. Nakamura, K. Okuyama, *Highly conductive nano-sized Magnéli phases titanium oxide (TiO_x)*, 7 (2017) 3646.

[3] J. Li, J. Wang, H. Kuang, H. Zhang, Y. Zhao, K. Qiao, F. Wang, W. Liu, W. Wang, L. C. Peng, Y. Zhang, and R.C. Yu, F. X. Hu, J. R. Sun, and B. G. Shen, *Oxygen defect engineering by the current effect assisted with temperature cycling in a perovskite-type $La_{0.7}Sr_{0.3}CoO_3$ film*, 9 (2017) 13214-13221.

[4] E.L. Runnerstrom, A. Bergerud, A. Agrawal, R.W. Johns, C. J. Dahlman, A. Singh, S. M. Selbach, D. J. Milliron, *Defect engineering in plasmonic metal oxide nanocrystals*, 16 (2016) 3390-3398.

[5] T. Koketsu, J. Ma, B.J. Morgan, M. Body, C. Legein, W. Dachraoui, M. Giannini, A. Demortière, M. Salanne, F. Dardoize, H. Groult, O. J. Borkiewicz, K. W. Chapman, P. Strasser, and D. Dambournet, *Reversible magnesium and aluminium ions insertion in cation-deficient anatase TiO_2*, 16 (2017) 1142.

[6] M.K. Nowotny, L.R. Sheppard, T. Bak, J. Nowotny, *Defect chemistry of titanium dioxide. Application of defect engineering in processing of TiO_2-based photocatalysts*, 112 (2008) 5275-5300.

[7] N.J. Lawrence, J.R. Brewer, L. Wang, T.-S. Wu, J. Wells-Kingsbury, M.M. Ihrig, G. Wang, Y.-L. Soo, W.-N. Mei, C.L. Cheung, *Defect Engineering in Cubic Cerium Oxide Nanostructures for Catalytic Oxidation*, Nano Letters, 11 (2011) 2666-2671.

[8] C. Jiang, L. Chen, S. Ji, J. Liu, Z. Zhang, P. Jin, Y. Wang, Z. Zhang, *Atomic scale observation of a defect-mediated first-order phase transition in $VO_2(A)$*, Nanoscale,

9 (2017) 9834-9840.

[9] F.G. Rinaldi, O. Arutanti, A.F. Arif, T. Hirano, T. Ogi, K. Okuyama, *Correlations between Reduction Degree and Catalytic Properties of WO_x Nanoparticles*, ACS Omega, 3 (2018) 8963-8970.

[10] K. Adachi and T. Asahi, *Activation of plasmons and polarons in solar control cesium tungsten bronze and reduced tungsten oxide nanoparticles*, Journal of Material Research, 27 (2012) 965-970.

[11] K. Machida, K. Adachi, *Ensemble Inhomogeneity of Dielectric Functions in Cs-Doped Tungsten Oxide Nanoparticles*, The Journal of Physical Chemistry C, 120 (2016) 16919-16930.

[12] S. Yoshio, M. Okada, K. Adachi, *Destabilization of pseudo-Jahn–Teller distortion in cesium-doped hexagonal tungsten bronzes*, Journal of Applied Physics, 124 (2018) 063109.

[13] S. Yoshio, K. Adachi, P*olarons in reduced cesium tungsten bronzes studied using the DFT + U method*, Materials Research Express, 6 (2018) 026548.

[14] W. Li, D. Corradini, M. Body, C. Legein, M. Salanne, J. Ma, K.W. Chapman, P.J. Chupas, A.-L. Rollet, C. Julien, K. Zhagib, M. Duttine, A. Demourgues, H. Groult, D. Dambournet, *High Substitution Rate in TiO_2 Anatase Nanoparticles with Cationic Vacancies for Fast Lithium Storage, Chemistry of Materials*, 27 (2015) 5014-5019.

[15] Y. Zhao, H. Pan, Y. Lou, X. Qiu, J. Zhu, C. Burda, *Plasmonic $Cu_{2-x}S$ Nanocrystals: Optical and Structural Properties of Copper-Deficient Copper(I) Sulfides*, Journal of the American Chemical Society, 131 (2009) 4253-4261.

[16] H. Takeda, K. Adachi, *Near Infrared Absorption of Tungsten Oxide Nanoparticle Dispersions*, Journal of the American Ceramic Society, 90 (2007) 4059-4061.

[17] J. B. Goodenough, *Magnetism and the Chemical Bond*. Bull. Soc. Chim. Fr., 4 (1965)

1200.

[18] M. Okada, K. Ono, S. Yoshio, H. Fukuyama, K. Adachi, *Oxygen vacancies and pseudo Jahn-Teller destabilization in cesium-doped hexagonal tungsten bronzes*, Journal of the American Ceramic Society, 102 (2019) 5386-5400.

[19] A.F. Arif, R. Balgis, T. Ogi, T. Mori, K. Okuyama, *Experimental and theoretical approach to evaluation of nanostructured carbon particles derived from phenolic resin via spray pyrolysis*, Chemical Engineering Journal, 271 (2015) 79-86.

[20] A.F. Arif, Y. Chikuchi, R. Balgis, T. Ogi, K. Okuyama, *Synthesis of nitrogen-functionalized macroporous carbon particles via spray pyrolysis of melamine-resin*, RSC Advances, 6 (2016) 83421-83428.

[21] R. Balgis, A.F. Arif, T. Mori, T. Ogi, K. Okuyama, G.M. Anilkumar, *Morphology-dependent electrocatalytic activity of nanostructured Pt/C particles from hybrid aerosol–colloid process*, 62 (2016) 440-450.

[22] O. Arutanti, A.F. Arif, R. Balgis, T. Ogi, K. Okuyama, F. Iskandar, *Tailored synthesis of macroporous Pt/WO_3 photocatalyst with nanoaggregates via flame assisted spray pyrolysis*, 62 (2016) 3864-3873.

[23] Young, R.A. *Introduction to the Rietveld method. -The Rietveld method edited by R.A. Young*. *IUCr Book Series*, 1993, 1-39

[24] Bruker AXS, Topas, Version 6.0. 2016.

[25] K. Machida, M. Okada, K. Adachi, *Excitations of free and localized electrons at nearby energies in reduced cesium tungsten bronze nanocrystals,* 125 (2019) 103103.

[26] J. Oi, A. Kishimoto, T. Kudo, *Hexagonal and Pyrochlore-Type Cesium Tungstate Synthesized from Cesium Peroxo-Polytungstate and Their Redox Chemistry*, Journal of Solid State Chemistry, 103 (1993) 176-185.

[27] P. J. Wiseman, and P. G. Dickens. *J. Solid State Chem.*, **1976**, 17 (1), 91-100.

[28] Y. Ikeuchi, H. Takatsu, C. Tassel, Y. Goto, T. Murakami, H. Kageyama, *High-Pressure Synthesis of Fully Occupied Tetragonal and Cubic Tungsten Bronze Oxides*, 129 (2017) 5864-5867.

[29] A. Hussain, *Phase analysis of potassium, rubidium and cesium tungsten bronzes*. Acta Chem. Scand. A, 32 (1978).

[30] A. Hussain, R. Gruehn, C. H. Rüscher, *Crystal growth of alkali metal tungsten brozes M_xWO_3 (M = K, Rb, Cs), and their optical properties*. J. Alloys Compd. 246 (1997), 51-61.

* This chapter was written based on the paper published on *Inorganic Chemistry*:

S. Nakakura, A.F. Arif, K. Machida, K. Adachi, T. Ogi, Cationic Defect Engineering for Controlling the Infrared Absorption of Hexagonal Cesium Tungsten Bronze Nanoparticles, Inorganic Chemistry, 58 (2019) 9101-9107.

Chapter 4

Improved Photochromic Stability in Less Deficient Cesium Tungsten Bronze Nanoparticles*

4.1 Introduction

In recent years, solar heat shielding materials have been applied to reduce the energy consumption of air conditioning. They have been shown to suppress the increase in ambient temperature inside houses, commercial buildings, and automobiles. Nanoparticles of alkali-doped hexagonal tungsten bronzes, M_xWO_3 (M = K, Rb, Cs), possess a remarkable high capacity for solar shielding owing to their strong near-infrared (NIR) absorption coupled with a high transmission of visible light [1,2]. Specifically, Cs-doped hexagonal tungsten bronze ($Cs_{0.32}WO_3$) nanoparticles exhibit excellent NIR light absorption that allows for their applications to solar control films of smart windows, NIR cut filters for CCD cameras and heating centers for laser welding and cancer therapies [3,4]. However, $Cs_{0.32}WO_3$ nanoparticles are known to manifest a set of weathering-related instabilities: a blue coloration under strong ultraviolet (UV) irradiation (*i.e.* photochromic instability) and a decolorization under high temperature and high humidity. Both color changes pose critical problems for commercial applications [5].

Recently, the decolorization process in a high-moisture environment has been investigated by Yoshio *et al*. using first-principles molecular dynamics calculations, and

with a constructed potential-pH diagram was clarified as composed of a two-step reaction: an ion dissolution of Cs^+ and an oxidation of $(WO_3)^-$ [6]. This mechanism explains the essential role of H_2O and O in the decolorization process, to which a steric barrier such as hydrogen sulfide (SH) in place of hydroxide (OH) was proposed to suppress the deterioration.

On the other hand, the photochromic instability in $Cs_{0.32}WO_3$ nanoparticles was reported by Adachi *et al*. to be due to the formation of a H_xWO_3 phase on the surface [5]. In general, photochromic materials such as WO_3 [7-10], MoO_3 [10,11], TiO_2 [12], and V_2O_5 [13], have been applied in the development of smart windows [7,10,12,14], colorimetric sensors [11,15], etc. owing to their spontaneous reversible change in color by external light. The color change observed in general photochromism is contrasted with that of $Cs_{0.32}WO_3$, in that the former is quite marked whereas the latter [5] is considerably weak in magnitude. The color change of WO_3 and MoO_3 has been attributed to the formation of a bronze structure (A_xWO_3, A= H, Li, Na, etc.) [10,11,16]. In particular, the photochromic mechanism of WO_3 is well understood as due to the injection of electrons in the conduction band by intercalation of hydrogen to form a H_xWO_3 phase [16-19]. In the case of $Cs_{0.32}WO_3$ nanoparticles, which already form the bronze structure with a slight bluish color with ample electrons in the conduction band, they undergo a further bluish color change upon UV irradiation. This is brought by the diffusion of H^+ ions from the resin matrix to amorphous or crystalline Cs-deficient sites [20] present in the particle skin over a depth of a few nm from the surface [5]. Because the H_xWO_3 phase on the surface of $Cs_{0.32}WO_3$ nanoparticles strongly absorbs red light (*i.e.,* the longer wavelengths of visible light), the relative intensity of transmitted shorter-wavelength visible light increases and the color of the particles turns to deep blue.

To resolve the photochromic instability of $Cs_{0.32}WO_3$ nanoparticles, Zeng *et al.*

coated $Cs_{0.32}WO_3$ nanoparticles with an amorphous SiO_2 including the UV-absorbing agent (UVA) [21]. Their study indicated an effectiveness of UVA in decreasing the color change, as UVA naturally reduces the applied UV strength. Zhou *et al.* fabricated an inert polyethylene terephthalate (PET) composite film with $Cs_{0.32}WO_3$ nanoparticles by the melt blending process [22]. They argued that the inert polymer is sufficiently effective in preventing the generation of H^+. Although these methods are impressive approaches to solving the photochromic instability of $Cs_{0.32}WO_3$ nanoparticles, they need additional improved materials for coating or special polymers that suppress the H^+ diffusion.

Herein, we focus the effect of the less defective surface of $Cs_{0.32}WO_3$ nanoparticles to prevent the injection of H^+ ions. Recently, the authors succeeded in producing $Cs_{0.32}WO_3$ nanoparticles by using spray pyrolysis and mild reduction treatment [23,24]. This process is proven to be effective in the direct synthesis of homogeneous nanometer-sized particles having a sharp particle size distribution and high crystallinity with very short reaction time [25-29]. Because of less damaged on the surface of $Cs_{0.32}WO_3$ nanoparticles, we can expect few Cs-deficient sites on $Cs_{0.32}WO_3$ nanoparticles of spray pyrolysis.

Base on the above background, we evaluated in detail the optical properties, *e.g.*, transmittance profile, haze value, and photochromic stability under UV irradiation for the $Cs_{0.32}WO_3$ nanoparticles synthesized through spray pyrolysis method. The evaluated optical performance was also compared with that of $Cs_{0.32}WO_3$ nanoparticles synthesized by a conventional solid-state reaction method. Furthermore, the Cs-deficient sites on the surface of $Cs_{0.32}WO_3$ nanoparticles were observed directly using a spherical aberration-corrected scanning TEM. The $Cs_{0.32}WO_3$ nanoparticles through spray pyrolysis exhibited the high photochromic stability compared with that of solid-state reaction method due to less Cs-deficient sites on the surface of nanoparticles.

4.2 Experimental

4.2.1 Synthesis of $Cs_{0.32}WO_3$ Nanoparticles

To produce $Cs_{0.32}WO_3$ nanoparticles via spray pyrolysis, ammonium para-tungstate pentahydrate (ATP; $(NH_4)_{10}(W_{12}O_{41})\cdot 5H_2O$; purity 88%–90%; Kanto Chemical Co., Inc., Tokyo, Japan) and cesium carbonate (Cs_2CO_3; purity 99.9% Sigma-Aldrich Co., St Louis, Mo, USA) with concentrations of 1.25 and 0.40 mmol/L, respectively, were dissolved in ultra-pure water. The diluted ATP and Cs_2CO_3 were placed into an ultrasonic nebulizer (NE-U17; Omron Healthcare Co., Ltd., Tokyo, Japan, operated at 1.7 MHz) to generate droplets. To introduce the droplets into a tubular ceramic reactor (1.3 m long with inner diameter of 28.5 mm), carrier air gas was used at a flow rate of 4 L/min. The reactor was divided into five zones, with each zone kept at a different temperature, *i.e*., 200, 500, 700, 1200, and 1200°C from the entrance to the exit sides. A paper filter (No.3, Advantec Toyo Kaisha, Ltd., Tokyo, Japan) heated at a temperature of 120°C was used to collect the particles (called "As-produced samples"). The obtained particles were heated in a quartz tubular furnace at a temperature of 600°C for 1 hr under a 5% H_2/Ar gas flow. Then the samples were blended with methyl isobutyl ketone (MIBK) and a trace dispersant agent at a powder-to-MIBK weight ratio of 1 : 50, and were properly stirred by a paint shaker for 10 min using ZrO_2 beads of 50 μmϕ to obtain a dispersed $Cs_{0.32}WO_3$ suspension. The milled samples derived from spray pyrolysis route are called as SP-$Cs_{0.32}WO_3$. A reference standard $Cs_{0.32}WO_3$ powder was prepared by a solid-state reaction route (called "SS-$Cs_{0.32}WO_3$"). The precursor of SS-$Cs_{0.32}WO_3$ prepared by mixing with solution of tungstic acid and cesium carbonate at Cs/W = 0.33, kneaded, and dried at 100°C for 12 hr in air [30]. This precursor was heated under a reducing gas flow (H_2/N_2 = 3/97 by

volume) at 800°C for 1 hr. The obtained powder was blended with MIBK (at 1 : 10 in weight) and a trace dispersant agent, and was strongly stirred by a paint shaker for 6 hr using ZrO_2 beads of 0.3 mmϕ.

4.2.2 Characterization

The crystalline phases of the samples were identified using X-ray diffraction (XRD; Bruker D2 Phaser, Bruker AXS GmbH, Karlsruhe, Germany) using Cu-Kα radiation (λ= 1.54 Å) and operated at 30 kV and 10 mA. The morphology of the particles was characterized using transmission electron microscopy (TEM; JEM-3000F, 297 kV, JEOL Ltd., Tokyo, Japan). The average particle diameter was determined by direct measurement of more than 200 randomly-selected particles. Cs-deficient sites on the surface of $Cs_{0.32}WO_3$ nanoparticles were investigated by an atomic resolution in a spherical aberration-corrected scanning TEM (STEM; JEM-ARM-200F, 200 kV, JEOL Ltd., Tokyo, Japan) operated in the high-angle annular dark field (HAADF) mode. Optical measurements were performed in a UV-Vis-NIR spectrophotometer (Model V-670, JASCO Corporation, Tokyo, Japan) for $Cs_{0.32}WO_3$ suspensions (particles concentration: 0.02 wt%) using a quartz cell with a 10 mm optical path length. To evaluate the photochromic instability of the nanoparticles, a $Cs_{0.32}WO_3$ suspension was obtained by blending the nanoparticles with an acrylic UV-setting resin UV-3701 (Toagosei Co., Ltd., Tokyo, Japan) at a $Cs_{0.32}WO_3$ powder:UV-3701 weight ratio of 1 : 5. The dispersed $Cs_{0.32}WO_3$ suspension was coated with a wire bar (#49 and #6 for the SP-$Cs_{0.32}WO_3$ and SS-$Cs_{0.32}WO_3$ samples, respectively) onto a soda-lime glass plate (3 mm-t×10 mm×10 mm) that was fixed on a bar coater (TC-3, Mitsui Electric Co., Ltd, Chiba, Japan). The coated $Cs_{0.32}WO_3$ suspension was then dried at 100 °C for 10 min to remove the organic solvent in resin. The resin on glass plate was cured in a belt UV illuminator (ECS-401GX,

Eye Graphics Co., Ltd, Tokyo, Japan) for 1 min with a mercury lamp (H04-L41, Eye Graphics Co., Ltd, Tokyo, Japan) powered at 80 W/cm^2 to ensure polymerization. The primary wavelength of the mercury lamp was 365 nm. Through these steps a $Cs_{0.32}WO_3$ nanoparticles-polymer composite film was formed on glass plates. The composite film was irradiated by UV light from one side for 5, 10, and 20 min. The total transmittance (T.T.) and haze value (Haze) were measured using a haze meter (NDH 5000, Nippon Denshoku Industries Co., Ltd., Tokyo, Japan) complying to ISO 13468-1:1996 and ISO 14782:1999, respectively. Visible light transmittance (VLT) was measured in compliance with ISO 9050:2003. Absorbance (ABS) was calculated from the transmittance (T) measured by the UV-Vis-NIR spectrophotometer. The values of T at 550 nm and 1300 nm are represented as $T_{550\ nm}$ and $T_{1300\ nm}$, respectively. Furthermore, the ABS at 0.95 eV (converted from the wavelength of 1300 nm) and 2.26 eV (converted from the wavelength of 550 nm) are denoted as $ABS_{0.95\ eV}$ and $ABS_{2.26\ eV}$, respectively. The ratio of $ABS_{0.95\ eV}$ to $ABS_{2.26\ eV}$ is denoted as $R = ABS_{0.95\ eV}/ABS_{2.26\ eV}$, where a greater R value corresponds to a stronger NIR absorption with respect to visible transmission. Variation in ABS due to UV irradiation for 20 min is defined as $V_{UV} = (ABS_{after\ UV\ irradiation} - ABS_{initial})/ABS_{initial}$.

4.3 Results and Discussion

4.3.1 Synthesis and Characterization of SP-$Cs_{0.32}WO_3$ Nanoparticles

Figure 4.1(a) shows XRD spectra of as-produced and heat-treated samples using spray pyrolysis. Although a mixed pattern of $Cs_{0.32}WO_3$ (ICDD No.04-009-6455) and $CsW_{1.6}O_6$ (ICDD No. 00-81-0012) was obtained for the as-produced samples, a heat treatment at 600 °C for 1 hr under 5% H_2/Ar gas flow dissolved the $CsW_{1.6}O_6$ phase, which then merged into the $Cs_{0.32}WO_3$ phase. In this treatment, the color of the particles was changed from light green (**Figure 4.1(b)**) to deep blue (**Figure 4.1(c)**).

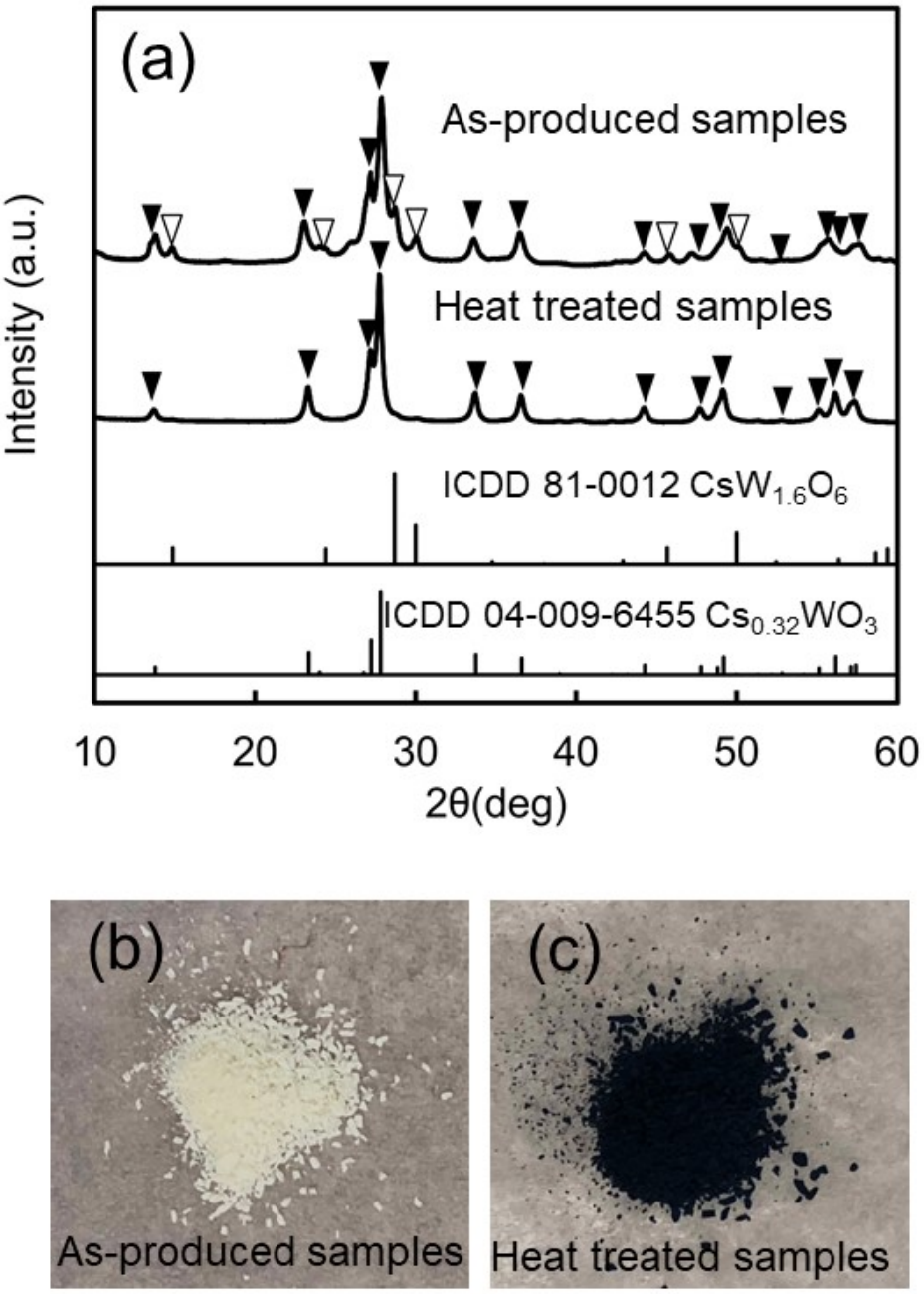

Figure 4.1 (a) XRD spectra and (b,c) optical micrographs of as-produced and heat-treated samples.

Figure 4.2(a) and (b) show TEM images at low and high magnification of the SP-$Cs_{0.32}WO_3$ particles, and **Figure 4.2(c)** shows their particle size distribution. It is seen that the SP-$Cs_{0.32}WO_3$ particles are nanometer-sized and well dispersed, like the as-produced samples (**Figure 4.2(d), (e)** and **(f)**). The geometric mean diameter, d_p, and geometric standard deviation, σ, of the particles were determined as 28.6 nm and 0.62 nm, respectively, *i.e.*, they were slightly larger in size and narrower in size distribution compared with the SS-$Cs_{0.32}WO_3$ nanoparticles, whose d_p and σ were 16.05 nm and 5.4 nm, respectively (**Figure 4.3(a) and (b)**). The shape of the SP-$Cs_{0.32}WO_3$ nanoparticles is approximated as a rounded hexagonal cylinder in contrast to the irregular and angular shape of SS-$Cs_{0.32}WO_3$ nanoparticles that were subjected to strong milling [30].

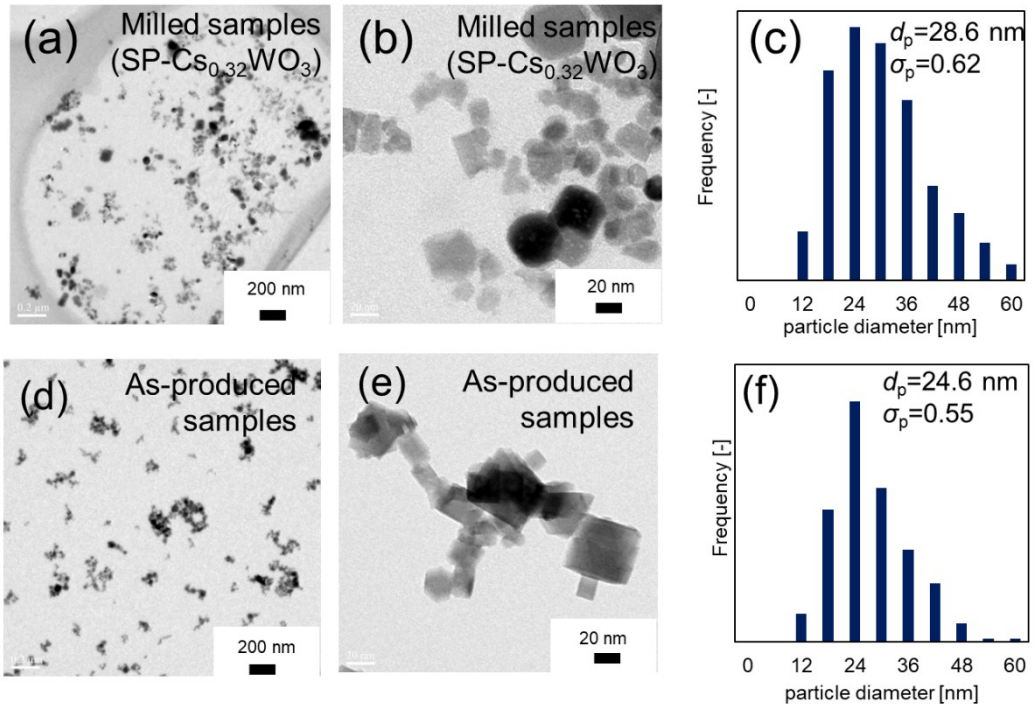

Figure 4.2 TEM images at (a,d) low and (b,d) high magnification, and (c,f) particle size distribution of lightly-milled samples and as-produced samples (SP-$Cs_{0.32}WO_3$).

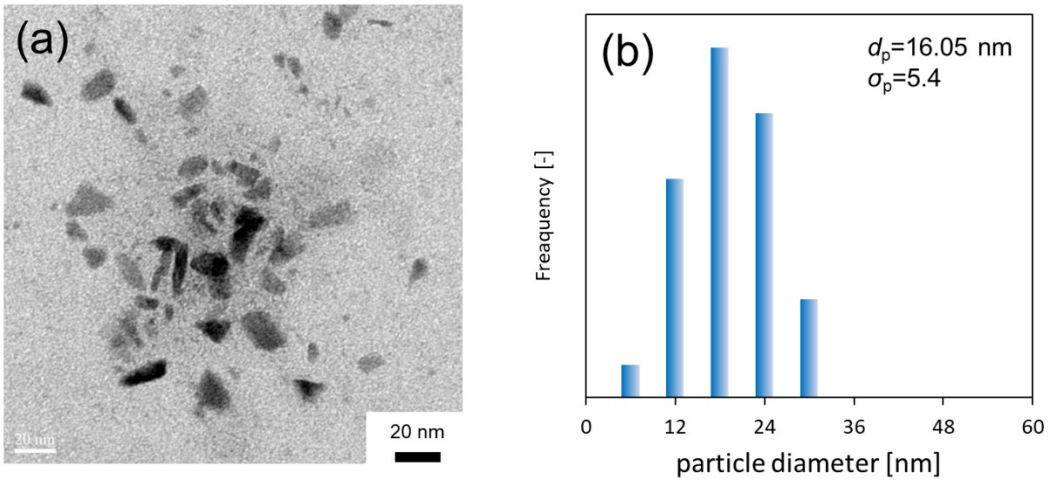

Figure 4.3 (a) TEM images and (b) particle size distribution of SS-$Cs_{0.32}WO_3$.

Figure 4.4 shows the transmittance spectra of the products. The as-produced sample exhibits low transmittance in the visible region and high transmittance in the NIR region. According to previous research [23], the absence of NIR absorption is due to the generation of planar W defects that suspend excess electrons to be provided to the conduction band. On the other hand, the transmittance spectrum of the heat-treated samples indicates a broad absorption in the NIR range between 800 and 2100 nm. Furthermore, the milled sample (SP-$Cs_{0.32}WO_3$) presents a further improved NIR absorption property with an increased transmission in the visible range. Thus, these results indicate a successful fabrication of $Cs_{0.32}WO_3$ nanoparticles with an intense NIR absorption capability using spray pyrolysis route that is comparable to those fabricated by the solid-state reaction route. Herein, the estimated R (= 5.8) of SP-$Cs_{0.32}WO_3$ was found to be lower than the R (= approximately 13) of the reference samples [1,30,31]. The NIR absorption property is strongly correlated with the electrons in the hybridized orbitals of W 5*d* and O 2*p* in the bottom of the conduction band, which are derived from

Cs dopant and oxygen vacancy (V_O) [30-34]. A possible reason for the low *R* of SP-$Cs_{0.32}WO_3$ is a lower number of electrons is provided from Cs and Vo than in the reference samples [23].

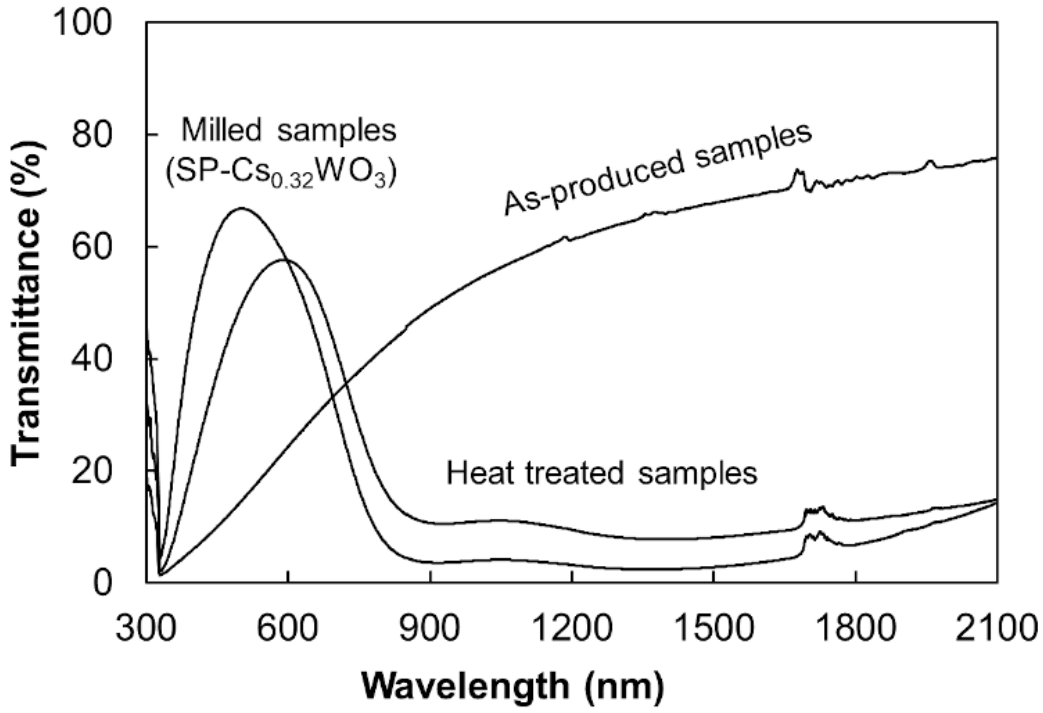

Figure 4.4 Transmittance spectra of as-produced, heat-treated, and milled (SP-$Cs_{0.32}WO_3$) samples.

4.3.2 Optical Stability of $Cs_{0.32}WO_3$ Nanoparticles

The optical properties of the samples before and after the UV irradiation for 20 min are shown in **Table 4.1**. Haze values of the milled SP-$Cs_{0.32}WO_3$ and SS-$Cs_{0.32}WO_3$ samples are 0.76% and 0.47%, respectively. Both haze values are below 1.0%, indicating a sufficiently low scattering in the visible region. The slightly larger haze value of SP-$Cs_{0.32}WO_3$ is attributed to the marginal presence of coarse particles exceeding 50 nm in size. The initial VLT values, 77.9% and 77.3% for SP-$Cs_{0.32}WO_3$ and SS-$Cs_{0.32}WO_3$,

respectively, decreased to 74.0% and 71.6%, respectively, after application of the UV irradiation for 20 min. This result indicates that the color change of $Cs_{0.32}WO_3$ samples occurred in both cases, showing a presence of the photochromic instability. A similar change was observed in the values of T.T. and $T_{550\ nm}$, as shown in **Table 4.1**.

Table. 4.1 Haze, VLT, Transmittance, and ABS of SP-$Cs_{0.32}WO_3$ and SS-$Cs_{0.32}WO_3$. The error range represents the standard deviation.

		Haze	*VLT*	*T.T.*	*Transmittance at 550 and 1300 nm*		*ABS at 0.95 and 2.26 eV*	
		%	%	%	$T_{550\ nm}$	$T_{1300\ nm}$	$ABS_{0.95\ eV}$	$ABS_{2.26\ eV}$
SP-$Cs_{0.32}WO_3$	Before UV	0.76	77.9	81.1	78.8	26.6	0.58	0.10
	(Error range)	(0.23)	(1.6)	(0.6)	(1.6)	(2.3)	(0.04)	(0.01)
	After UV	0.74	74.0	75.7	74.3	24.0	0.62	0.13
	(Error range)	(0.17)	(2.2)	(2.7)	(2.4)	(2.8)	(0.05)	(0.01)
SS-$Cs_{0.32}WO_3$	Before UV	0.47	77.3	79.9	78.3	9.5	1.03	0.11
	(Error range)	(0.02)	(1.2)	(0.9)	(1.1)	(2.3)	(0.11)	(0.01)
	After UV	0.43	71.6	73.6	72.7	6.4	1.21	0.14
	(Error range)	(0.05)	(2.1)	(1.4)	(1.9)	(2.2)	(0.17)	(0.01)

The corresponding change in transmittance profiles are shown in **Figures. 4.5(a) and (b)**. Dependence of T.T. on the UV irradiation time, *i.e.*, the photochromic stability, is shown in **Figure 4.6**. In the initial 5 min, both samples show a rapid decrease in T.T. by about 4 points, whereas after 20 min SS-$Cs_{0.32}WO_3$ continued to decrease rapidly while SP-$Cs_{0.32}WO_3$ slowed down and moderated. This difference suggests that SP-$Cs_{0.32}WO_3$ has a higher stability against UV irradiation than conventional SS-$Cs_{0.32}WO_3$. Similarly

in 20 min, $ABS_{0.95eV}$ increased by only 8% (= (0.62–0.58)/0.58) in SP-$Cs_{0.32}WO_3$ against 16% (= (1.21-1.03)/1.03) in SS-$Cs_{0.32}WO_3$, as shown in **Table. 4.1**. After the UV irradiation was stopped, bleaching occurred slowly when the specimen was placed in a dark place to recover more than 95 % transmission after several days, in agreement with the previous report [5].

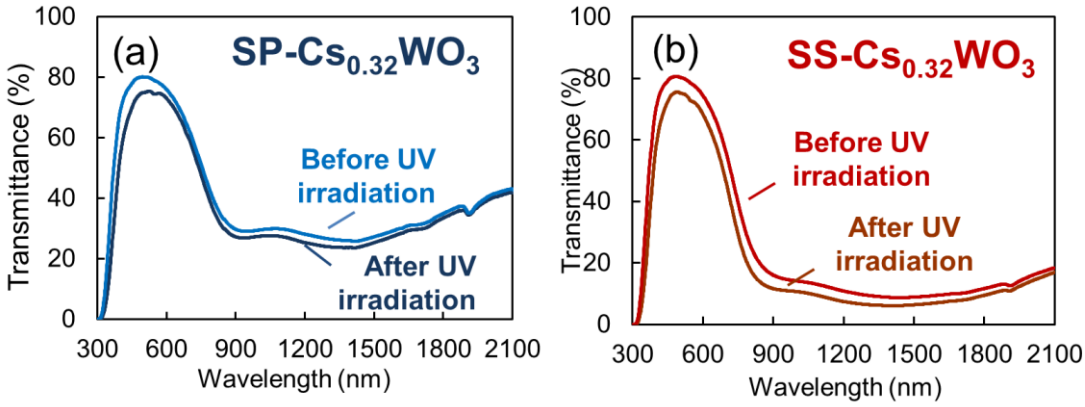

Figure 4.5 Transmittance profiles before and after the 20-min UV irradiation for (a) SP-$Cs_{0.32}WO_3$ and (b) SS-$Cs_{0.32}WO_3$.

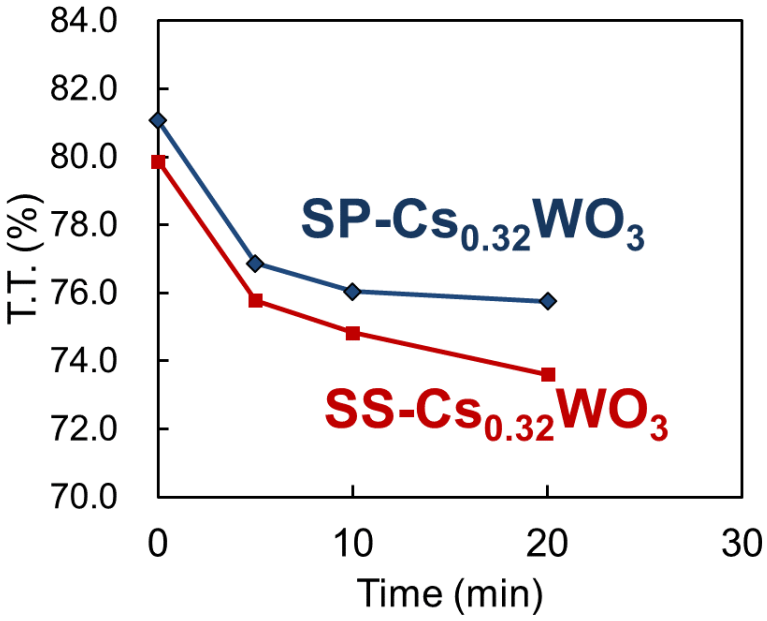

Figure 4.6 Dependence of T.T. on the UV irradiation time for (a) SP-$Cs_{0.32}WO_3$ and (b) SS-$Cs_{0.32}WO_3$.

The variation in ABS due to UV irradiation, V_{UV}, is known to produce double peaks [5] as indicated in **Figure 4.7**. The peaks are located at 0.98 eV and 1.51 eV, and are designated as the absorbance peaks by H_xWO_3 [5]. The magnitude of V_{UV} for SP-$Cs_{0.32}WO_3$ is about 1/5 that for SS-$Cs_{0.32}WO_3$ in the wide range between 0.5 and 2.3 eV. These observations indicate an improved optical stability against external UV irradiation for particles synthesized by spray pyrolysis route compared with those by the solid-state reaction route.

According to the previous analysis on $Cs_{0.32}WO_3$ [5], the origin of the color change upon UV irradiation is attributed to the formation of H_xWO_3 by the insertion of H^+ ions in the Cs-deficient sites of $Cs_{0.32}WO_3$ nanoparticles. The present result of the decreased effect of UV irradiation in SP-$Cs_{0.32}WO_3$ is consistent with the decreased Cs-deficient sites assumed in SP-$Cs_{0.32}WO_3$. No shift in the band gap was observed in **Figures 4.5(a)**

and (b) because the increased fraction of electron carrier in H_xWO_3 is quite small besides that the energy band itself should be modified.

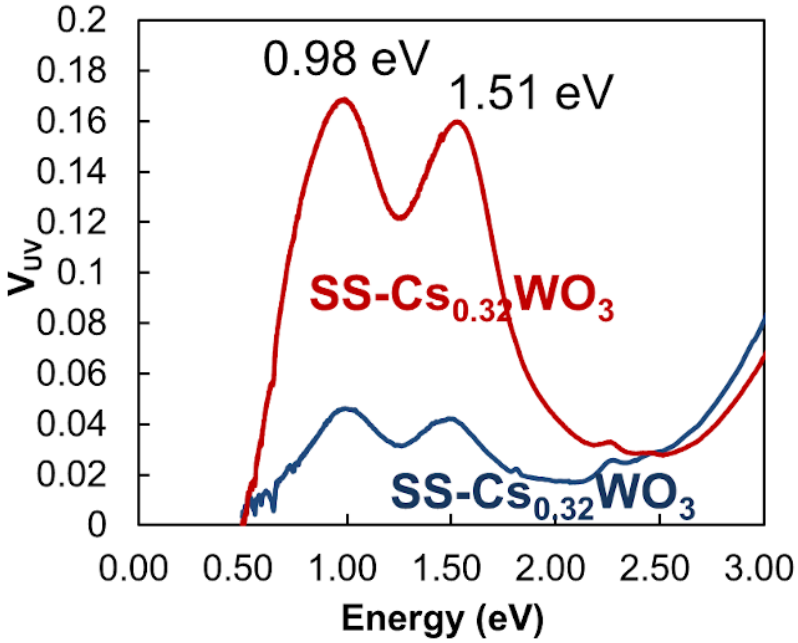

Figure 4.7 V_{UV} with respect to photon energy for (a) SP-$Cs_{0.32}WO_3$ and (b) SS-$Cs_{0.32}WO_3$.

Figure 4.8(a) shows a STEM-HAADF image of SP-$Cs_{0.32}WO_3$ projected on (010). In STEM-HAADF images, the brightness of the spot contrast is proportional to an atomic number and a projected density of atoms. The brightest and second brightest spots in **Figure 4.8(a)** are the projections of W atoms, while the weakest spots correspond to Cs atoms. **Figure 4.8(b)** shows a schematic atomic structure projected on (010) that is compared with the observed image in **Figure 4.8(a)**. A plane consisting of W and O atoms (W plane) and a plane consisting of Cs and O atoms (Cs plane) are alternately arranged. Cs atoms find a diffusion path along the c-axis through the hexagonal tunnels in $Cs_{0.32}WO_3$ [6], as shown in **Figure 4.8(c)**. To evaluate the removal of Cs atoms, spot

intensity was scanned along lines a–b, c–d, and e–f in **Figure 4.8(a)** and the resulting profiles are shown in **Figure 4.8(d)**. The Cs peaks are observed as regularly arranged along lines a–b and c–d, whereas they appear to be partially depleted along e–f in the outermost layer. Thus, Cs atoms are fully arranged in the interior up to the second layer from the surface and are partly deficient only in the outermost layer at less than 1 nm from the surface.

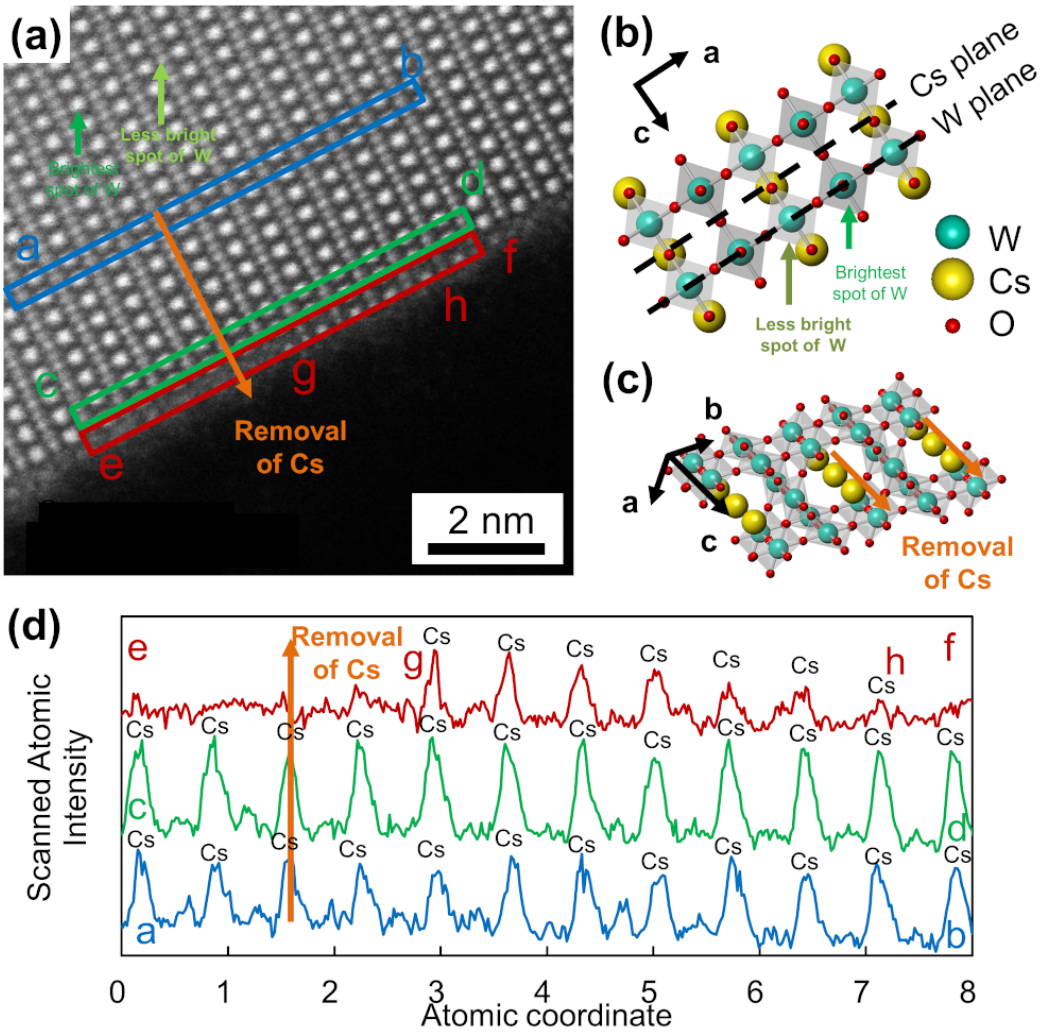

Figure 4.8 (a) Direct observation of Cs atoms on (010) in SP-$Cs_{0.32}WO_3$ in the STEM-HAADF image. (b, c) illustrate the schematic atomic arrangements of $Cs_{0.32}WO_3$, (d) shows scanned spot intensity profiles along lines a–b, c–d, and e–f in **Figure 4.8(a)**.

A similar analysis was conducted for STEM-HAADF images of (001) as shown in **Figure 4.9**. Cs deficient regions are confirmed on the outermost surface on $Cs_{0.32}WO_3$ particles as shown by the yellow arrows in **Figure 4.9**, whereas the second Cs/W plane from the surface (c–d) does not involve the Cs deficiency. Thus, the full occupancy of Cs atoms is preserved up to the second outermost surface; this is consistent with the results of the observation from (010). This analysis reveals that the SP-$Cs_{0.32}WO_3$ is fully doped with Cs atoms except for the outermost surface, which contributed to the few variations in the ABS change (*i.e.* V_{UV}). On the other hand, SS-$Cs_{0.32}WO_3$ has Cs-deficient sites to the depth of a few nm from the surface [5,20] that caused a large variation in V_{UV}. Thus, SP-$Cs_{0.32}WO_3$ suppressed the H^+ doping of Cs sites on the surface and retained its high photochromic stability compared with SS-$Cs_{0.32}WO_3$. These results are consistent with the mechanism reported in a previous study [5]; therefore, we conclude that spray pyrolysis can effectively improve the photochromic instability of $Cs_{0.32}WO_3$ nanoparticles.

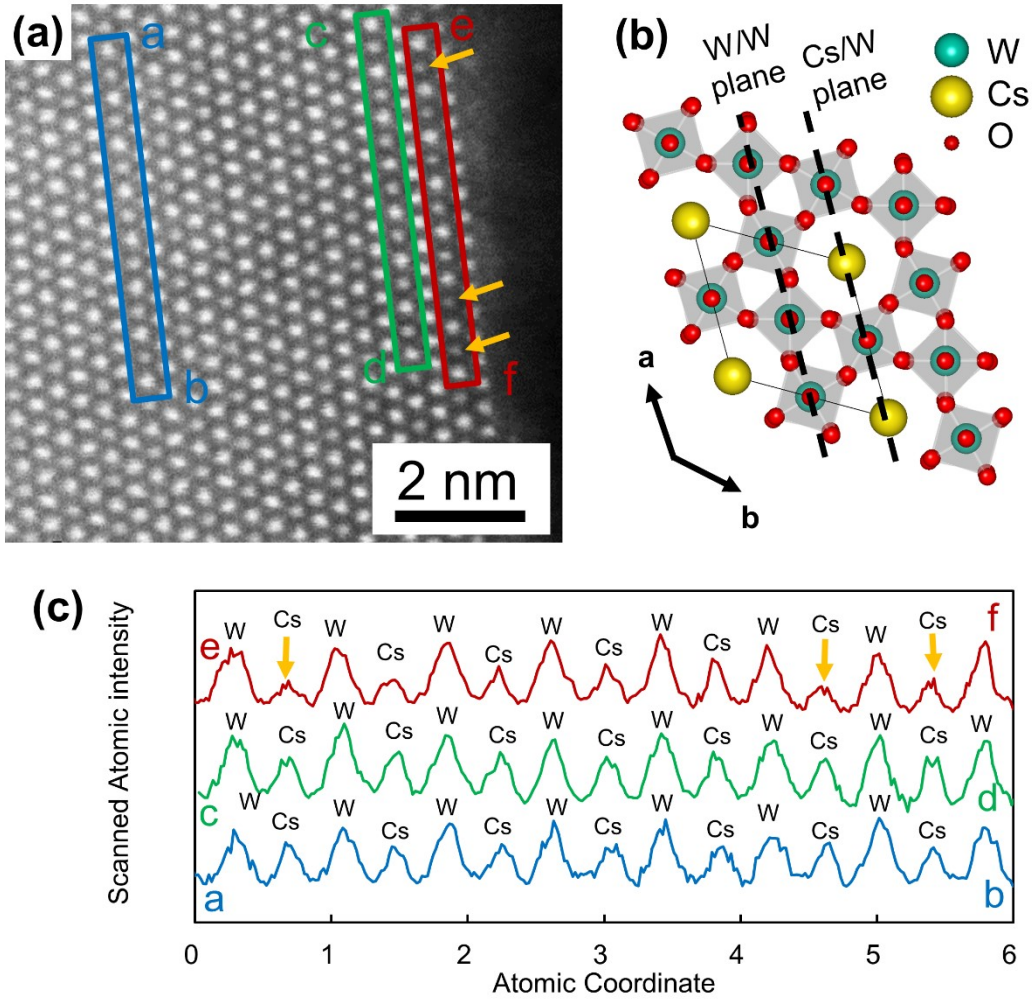

Figure 4.9 Direct observation of Cs atom rows in SP-$Cs_{0.32}WO_3$ observed along [001]. (a) STEM image in the HAADF mode, (b) schematic atomic arrangement, and (c) scanned spot intensity profiles along a–b, c–d, and e–f, respectively, in **Figure 4.9(a)**.

4.4 Summary

The present study revealed that the less Cs-deficient $Cs_{0.32}WO_3$ nanoparticles synthesized through spray pyrolysis route exhibit an improved photochromic stability, *i.e.*, they prevent color change due to UV irradiation. We demonstrated that less Cs-deficient $Cs_{0.32}WO_3$ nanoparticles could be successfully synthesized via spray pyrolysis route than via the solid-state reaction route. The variation in the ABS of SP-$Cs_{0.32}WO_3$ upon UV

irradiation was shown to be 1/5 that of SS-$Cs_{0.32}WO_3$ in the wide range between 0.5 and 2.3 eV. The STEM-HAADF analysis revealed that the Cs-deficient sites were limited to the outermost layer in SP-$Cs_{0.32}WO_3$, which contribute to the excellent photochromic stability of SP-$Cs_{0.32}WO_3$. These observations indicate that the color change upon UV irradiation originates from the Cs-deficient sites on the surface of $Cs_{0.32}WO_3$. The results obtained in this study are expected to contribute to further understanding of the photochromic behaviors in inorganic materials in general.

4.5 References

[1] H. Takeda, K. Adachi, *Near Infrared Absorption of Tungsten Oxide Nanoparticle Dispersions*, Journal of the American Ceramic Society, 90 (2007) 4059-4061.

[2] X.-J. Huang, J. Bao, Y. Han, C.-W. Cui, J.-X. Wang, X.-F. Zeng, J.-F. Chen, *Controllable synthesis and evolution mechanism of tungsten bronze nanocrystals with excellent optical performance for energy-saving glass*, Journal of Materials Chemistry C, 6 (2018) 7783-7789.

[3] C. Guo, S. Yin, H. Yu, S. Liu, Q. Dong, T. Goto, Z. Zhang, Y. Li, T. Sato, *Photothermal ablation cancer therapy using homogeneous Cs_xWO_3 nanorods with broad near-infra-red absorption*, Nanoscale, 5 (2013) 6469-6478.

[4] W. Guo, C. Guo, N. Zheng, T. Sun, S. Liu, *Cs_xWO_3 Nanorods Coated with Polyelectrolyte Multilayers as a Multifunctional Nanomaterial for Bimodal Imaging-Guided Photothermal/Photodynamic Cancer Treatment*, Advanced Materials, 29 (2017) 1604157.

[5] K. Adachi, Y. Ota, H. Tanaka, M. Okada, N. Oshimura, A. Tofuku, *Chromatic instabilities in cesium-doped tungsten bronze nanoparticles*, Journal of Applied Physics, 114 (2013) 194304.

[6] S. Yoshio, K. Adachi, M. Kubo, *Cesium desorption mechanism in $Cs_{0.33}WO_3$ by first-principles molecular dynamics calculations*, Journal of Applied Physics, 126 (2019) 073101.

[7] C.G. Granqvist, *Chromogenic materials for transmittance control of large-area windows*, Critical Reviews in Solid State and Materials Sciences, 16 (1990) 291-308.

[8] S. Li, M. Samy El-Shall, *Synthesis and characterization of photochromic molybdenum and tungsten oxide nanoparticles*, Nanostructured Materials, 12 (1999) 215-219.

[9] Q. Liu, C. Hu, X. Wang, *Hydrothermal synthesis of oxygen-deficiency tungsten oxide quantum dots with excellent photochromic reversibility*, Applied Surface Science, 480 (2019) 404-409.

[10] T.H. Fleisch, G.J. Mains, *An XPS study of the UV reduction and photochromism of MoO_3 and WO_3*, The Journal of chemical physics, 76 (1982) 780-786.

[11] A. Borgschulte, O. Sambalova, R. Delmelle, S. Jenatsch, R. Hany, F. Nüesch, *Hydrogen reduction of molybdenum oxide at room temperature*, Scientific Reports, 7 (2017) 40761.

[12] U. Joost, A. Šutka, M. Oja, K. Smits, N. Döbelin, A. Loot, M. Järvekülg, M. Hirsimäki, M. Valden, E. Nõmmiste, *Reversible Photodoping of TiO_2 Nanoparticles for Photochromic Applications*, Chemistry of Materials, 30 (2018) 8968-8974.

[13] S. Nishio, M. Kakihana, *Evidence for Visible Light Photochromism of V_2O_5*, Chemistry of Materials, 14 (2002) 3730-3733.

[14] M. Hočevar, U. Opara Krašovec, *A photochromic single glass pane*, Solar Energy Materials and Solar Cells, 186 (2018) 111-114.

[15] S. Tanaka, K. Adachi, S. Yamazaki, *Surface-enhanced photochromic phenomena of phenylalanine adsorbed on tungsten oxide nanoparticles: a novel approach for "label-free" colorimetric sensing*, Analyst, 138 (2013) 2536-2539.

[16] Y. Cui, F. Liang, C. Ji, S. Xu, H. Wang, Z. Lin, J. Liu, *Discoloration Effect and One-Step Synthesis of Hydrogen Tungsten and Molybdenum Bronze (H_xMO_3) using Liquid Metal at Room Temperature*, ACS Omega, 4 (2019) 7428-7435.

[17] C.G. Granqvist, *Electrochromic tungsten oxide films: Review of progress 1993–1998*, Solar Energy Materials and Solar Cells, 60 (2000) 201-262.

[18] R.J. Colton, A.M. Guzman, J.W. Rabalais, *Photochromism and electrochromism in amorphous transition metal oxide films*, Accounts of Chemical Research, 11 (1978)

170-176.

[19] G.A. Niklasson, C.G. Granqvist, *Electrochromics for smart windows: thin films of tungsten oxide and nickel oxide, and devices based on these*, Journal of Materials Chemistry, 17 (2007) 127-156.

[20] Y. Sato, M. Terauchi, K. Adachi, *High energy-resolution electron energy-loss spectroscopy study on the near-infrared scattering mechanism of $Cs_{0.33}WO_3$ crystals and nanoparticles*, Journal of Applied Physics, 112 (2012) 074308.

[21] X. Zeng, Y. Zhou, S. Ji, H. Luo, H. Yao, X. Huang, P. Jin, *The preparation of a high performance near-infrared shielding Cs_xWO_3/SiO_2 composite resin coating and research on its optical stability under ultraviolet illumination*, Journal of Materials Chemistry C, 3 (2015) 8050-8060.

[22] Y. Zhou, N. Li, Y. Xin, X. Cao, S. Ji, P. Jin, *Cs_xWO_3 nanoparticle-based organic polymer transparent foils: low haze, high near infrared-shielding ability and excellent photochromic stability*, Journal of Materials Chemistry C, 5 (2017) 6251-6258.

[23] S. Nakakura, A.F. Arif, K. Machida, K. Adachi, T. Ogi, *Cationic Defect Engineering for Controlling the Infrared Absorption of Hexagonal Cesium Tungsten Bronze Nanoparticles*, Inorganic Chemistry, 58 (2019) 9101-9107.

[24] T. Hirano, S. Nakakura, F.G. Rinaldi, E. Tanabe, W.-N. Wang, T. Ogi, *Synthesis of highly crystalline hexagonal cesium tungsten bronze nanoparticles by flame-assisted spray pyrolysis*, Advanced Powder Technology, 29 (2018) 2512-2520.

[25] M.T. Swihart, *Vapor-phase synthesis of nanoparticles*, Current Opinion in Colloid & Interface Science, 8 (2003) 127-133.

[26] K. Okuyama, I. Wuled Lenggoro, *Preparation of nanoparticles via spray route*, Chemical Engineering Science, 58 (2003) 537-547.

[27] T. Ogi, A.B.D. Nandiyanto, K. Okuyama, *Nanostructuring strategies in functional fine-particle synthesis towards resource and energy saving applications*, Advanced Powder Technology, 25 (2014) 3-17.

[28] S. Nakakura, A.F. Arif, F.G. Rinaldi, T. Hirano, E. Tanabe, R. Balgis, T. Ogi, *Direct synthesis of highly crystalline single-phase hexagonal tungsten oxide nanorods by spray pyrolysis*, Advanced Powder Technology, 30 (2019) 6-12.

[29] R. Mueller, L. Mädler, S.E. Pratsinis, *Nanoparticle synthesis at high production rates by flame spray pyrolysis*, Chemical Engineering Science, 58 (2003) 1969-1976.

[30] K. Machida, K. Adachi, *Ensemble Inhomogeneity of Dielectric Functions in Cs-Doped Tungsten Oxide Nanoparticles*, The Journal of Physical Chemistry C, 120 (2016) 16919-16930.

[31] K. Machida, M. Okada, K. Adachi, *Excitations of free and localized electrons at nearby energies in reduced cesium tungsten bronze nanocrystals*, Journal of Applied Physics, 125 (2019) 103103.

[32] S. Yoshio, K. Adachi, *Polarons in reduced cesium tungsten bronzes studied using the DFT + U method*, Materials Research Express, 6 (2018) 026548.

[33] S. Yoshio, M. Okada, K. Adachi, *Destabilization of pseudo-Jahn–Teller distortion in cesium-doped hexagonal tungsten bronzes*, Journal of Applied Physics, 124 (2018) 063109.

[34] M. Okada, K. Ono, S. Yoshio, H. Fukuyama, K. Adachi, *Oxygen vacancies and pseudo Jahn-Teller destabilization in cesium-doped hexagonal tungsten bronzes*, Journal of the American Ceramic Society, 102 (2019) 5386-5400.

[35] K. Adachi and T. Asahi, *Activation of plasmons and polarons in solar control cesium tungsten bronze and reduced tungsten oxide nanoparticles*, Journal of Material Research, 27 (2012) 965-970.

[*] This chapter was written based on the paper published on *Advanced Powder Technology*:

S. Nakakura, k. Machida, E. Tanabe, K. Adachi, and T. Ogi, “Improved Photochromic Stability in Less Deficient Cesium Tungsten Bronze Nanoparticles”, *Advanced Powder Technology* , in press

Chapter 5

Conclusion

Various kinds of tungsten oxide particles, such as hexagonal tungsten oxide nanorods and cesium doped tungsten oxide nanoparticles that include a tungsten deficiency, were successfully synthesized by the spray pyrolysis (SP) method.

The relationship between a tungsten deficiency and near infrared absorption properties were clarified, and the photochromic properties of cesium doped tungsten oxide nanoparticles were improved.

The major highlights of this dissertation are follows:

1. Single phase hexagonal tungsten oxide nanorods were synthesized by extending the residence time with the SP method. However, gas absorption analysis indicated that the performance based on the hexagonal channels was subpar, and this is thought to be because these nanorods were sintered and had stacking faults.
2. $Cs_{0.32}WO_3$ nanoparticles that include a tungsten deficiency were synthesized by the SP method. Detail analyses disclosed the presence of cationic defects; that is, a tungsten deficiency and insufficient Cs doping of the $Cs_{0.32}WO_3$ nanoparticles. We clarified that a tungsten deficiency is a key factor in obtaining near-infrared (NIR) absorption properties, and the combination of SP and heat treatment is effective in controlling the tungsten deficiency, lattice constants and NIR absorption properties.
3. The less Cs-deficient $Cs_{0.32}WO_3$ nanoparticles synthesized through the spray pyrolysis route exhibited improved photochromic stability, i.e., they were immune to color changes caused by UV irradiation. The STEM-HAADF analysis revealed

that the Cs-deficient sites were limited to the outermost layers in the SP-$Cs_{0.32}WO_3$, which contributed to its excellent photochromic stability. Thus, we conclude that spray pyrolysis is an effective method of improving the photochromic instability of $Cs_{0.32}WO_3$ nanoparticles.

Based on these highlights, $Cs_{0.32}WO_3$ nanoparticles synthesized by spray pyrolysis have many advantages, including the presence of a tungsten deficiency and fewer Cs-deficient sites on the surface. This method and its concepts are expected to contribute to further advances in inorganic materials.

List of figures

List of tables

List of publications

1. S. Nakakura, A.F. Arif, F.G. Rinaldi, T. Hirano, E. Tanabe, R. Balgis, T. Ogi, Direct synthesis of highly crystalline single-phase hexagonal tungsten oxide nanorods by spray pyrolysis, *Advanced Powder Technology*, **30** (2019) 6-12.

2. S. Nakakura, A.F. Arif, K. Machida, K. Adachi, T. Ogi, Cationic Defect Engineering for Controlling the Infrared Absorption of Hexagonal Cesium Tungsten Bronze Nanoparticles, *Inorganic Chemistry*, **58** (2019) 9101-9107.

3. S. Nakakura, K. Machida, E. Tanabe, K. Adachi, T. Ogi, Improved Photochromic Stability in Less Deficient Cesium Tungsten Bronze Nanoparticles, *Advanced Powder Technology*, in press.

Acknowledgements

First of all, I would like to express my deep gratitude my supervisor, Associate Professor Takashi Ogi for his continued guidance, helpful suggestion, and encouragement both with my research and my life. Without his guidance, it was impossible to finish my doctoral course. I am also grateful to Professor Kikuo Okuyama, Assistant Professor Ratna Balgis, and Dr. Aditya Farhan Arif for all their help and advices. I am grateful to my Ph.D. referees: Professor Toshinori Tsuru, Professor Akihiro Yabuki, and Professor Masahiro Sadakane for their constructive criticism, suggestions, and insights.

I would like to mention all members related my doctoral course in Sumitomo Metal Mining Co. Ltd., for valued support the social Ph. D program and for preparing the environment both in the company and the university. For my research, I am grateful thanks to Dr. Kenji Adachi, Research Director in Sumitomo Metal Mining Co. Ltd., for important discussion and suggestion. I also like to appreciate to Mr. Keisuke Machida for his kind advices.

I thank to Ms. Michiyo Tachibana, Mr. Cao Le Kiet Anh, Mr. Hikaru Osakada, Mr. Tomoyuki Hirano, Mr. Jun Kikkawa, and all other members of the Ogi laboratory for their kind help with experiments and with my life in Hiroshima University.

Finally, I would like to thank to my wife, Ayumi Nakakura; my son, Issei Nakakura; and my daughter, Seri Nakakura (born on 23 June 2019, *i.e.* the final year of this doctoral program) for their encouragement and care, and for the smiles.

Shuhei Nakakura

Higashi-Hiroshima, Japan

March, 2020